Master's Thesis

Dimension-reduction for reconstruction of dynamic particle configurations from MRI data

Tabea Naeven

Matr. 426723

Supervisor: Prof. Dr. Benedikt Wirth
Assisting Supervisor: Dr. Frank Wübbeling

Abstract

This thesis addresses the inverse problem of reconstructing dynamic particle configurations from finitely many observations, a task with applications for instance in the field of biomedical imaging. Reconstructions directly in the high-dimensional space of particle positions and velocities are often not computationally feasible, necessitating dimension-reduced methods. The present work considers an approach that employs projections onto lower-dimensional subspaces via Radon transforms, which allows reduced computational effort while maintaining exact reconstruction results of the full-dimensional problem.

Since MRI scans are not instantaneous, particle movement during data acquisition introduces additional challenges such as motion blur. To address this, this thesis builds on the aforementioned dimension-reduced reconstruction method, which assumes discrete snapshots in time, and introduces adaptations for continuous temporal progression in MRI with cartesian sampling. The MRI-adapted method is then evaluated on both simulated and real MRI data, showing accurate reconstructions of dynamic particles even in high-velocity configurations, and thus extending the applicability of the dimension-reduction technique to the MRI setting.

Acknowledgements

Contents

List of Figures

List of Tables

CHAPTER 1

Introduction

An *inverse problem* is the problem of determining an unknown cause based on observed effects. A highly prevalent area of application for inverse problems is medical image reconstruction, in which the objective is to reconstruct internal objects in a patient's body. Examples include retrieving an image of a patient's anatomy from X-ray measurements, or inferring the positions of iron-marked cells in a body from scan data obtained with Magnetic Resonance Imaging (MRI). The latter is the application we are concerned with in this thesis.

In order to construct an inverse problem for a particular imaging method, a *forward* or *observation operator* needs to be defined that suitably describes the considered measuring process. Let X, Y be general spaces of causes and effects. Then the inverse problem of computing cause x backward from effect y can be described as

$$\text{given } y \in Y, \text{ find } x \in X \text{ such that } Ax = y, \tag{1.1}$$

where $A : X \to Y$ is the forward operator. An inverse problem is called *well-posed* according to the definition by Jacques Hadamard [1], if all of the following properties are fulfilled:

1. It has a solution $x \in X$,

2. the solution is unique, and

3. the solution continuously depends on y.

Most inverse problems, however, violate at least one and often all of these conditions, meaning they are *ill-posed*. Thus, a well-posed regularised formulation approximating the problem is thus instead. The methods studied in this thesis replace the inverse problem (1.1) with an optimisation problem

$$\arg\min_{x \in X} F(Ax) + G(x) \tag{1.2}$$

where $F : Y \to (-\infty, \infty]$ is the fidelity term, which ensures closeness of Ax to the observed data, and $G : X \to (-\infty, \infty]$ is the regularisation term, which imposes certain constraints or properties on the solution.

Consider a configuration of linearly moving particles. An approach for the reconstruction of particle positions and trajectories was introduced by Alberti et al. in [2], in the form of a convex program. This program has the disadvantage of being very high-dimensional, leading to high computational costs. The dimension-reduced method proposed by Holler, Schlüter and Wirth in [3] addresses these computational challenges by employing Radon transforms to reduce the high-dimensional problem to a collection of problems on projections with

only one dimension in space respectively. While the dimension-reduced method is tested in [3] in experiments using a truncated Fourier transform as the observation operator, it has not yet been applied to the concrete case of MRI data. This is the contribution of this thesis. Specifically, our objective is to construct an observation operator for MRI and evaluate its performance and properties in experiments on both simulated and real MRI data of dynamic particle configurations. The core challenge in this lies in the fact that the acquisition of data with an MRI scan takes a certain amount of time during which dynamic particles continue moving, leading to motion blurring in the acquired images. Depending on the specific imaging scheme employed and the particle velocities, particles may become blurred and thus not unambiguously locatable, or they may even be entirely invisible. in the finalised image. Figure 1.1 illustrates the progression of motion blur with increasing particle velocities. We construct a novel truncated Fourier transform-based observation

a)   b)   c)
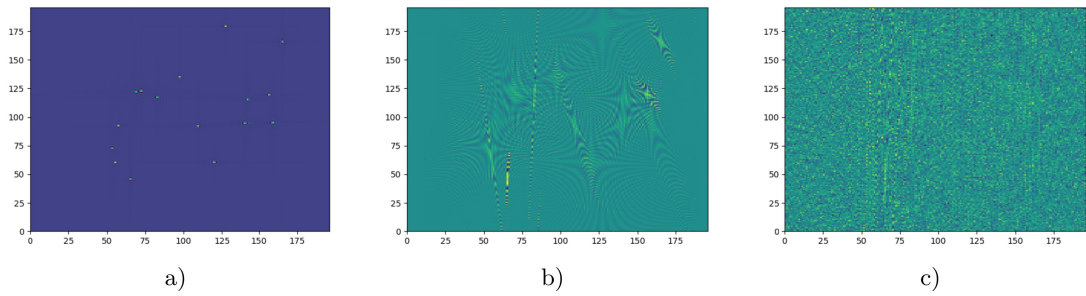
Figure 1.1.: Illustrative MRI images of the same simulated particle configuration at varying velocities: Static in a), at low-velocity in b) and in c) at twenty times the velocity of b).

operator that accounts for the passage of time and perform experiments in the setting of linearly moving iron particles in a homogeneous medium. We demonstrate that our MRI-adapted method performs well on configurations of high velocities on which using the dimension-reduced method with the unaltered truncated Fourier observation operator fails. Additionally, we show superior performance of the MRI-adapted version on a low-velocity scan with only minor motion blur.

1.1. Overview of this thesis

After stating some preliminary definitions and results in section 1.2, we introduce the dimension-reduced method by Holler et al. [3] in chapter 2. We start from static particle configurations and continue to the dynamic problem, define and establish central properties of Radon and move operators and derive the dimension reduction.

In chapter 3, we prove reconstruction properties of the dimension-reduced method. Specifically, we cover exact reconstruction in the absence of noise and error estimates for the case of noisy data.

After reproducing the method by Holler et al., we give an overview of the workings of MRI scanners in chapter 4 in order to deduce indicators for the definition of an observation operator that suitably approximates MRI.

Such an observation operator is then constructed in chapter 5. Based on the truncated Fourier transform, we design it to account for the passage of time during measurements and the non-zero radii of iron particles' areas of influence on the acquired scan images.

In chapter 6, we then test the MRI-adapted method in numerical experiments on both simulated data and images obtained from real MRI scans. We assess method performance and compare it to that of the dimension-reduced method using the unaltered truncated Fourier transform, gather indications on dynamic particle separation as a possible source condition for reconstruction, and evaluate error estimates in experiments with noise.

Lastly, we summarise our findings and give a brief outlook on possible further experiments and questions of interest in chapter 7.

1.2. Preliminaries

In this section, we present some definitions and results that are key to the topics of this thesis, covering Radon measures, product measures and pushforwards, primal and dual optimisation problems, and the Fourier transform. Proofs are omitted here for brevity but can be found in the referenced sources provided.

Definition 1 (Borel measure and total variation ([3], Def 7))**.** *Let X be a topological space. The* Borel σ-algebra $\mathcal{B}(X)$ *on X is the smallest σ-algebra containing all open sets. A* real Borel measure *is a countably-additive set function $\nu : \mathcal{B}(X) \to \mathbb{R}$. The* total variation *of a real Borel measure $\nu : \mathcal{B}(X) \to \mathbb{R}$ is the non-negative Borel measure defined as*

$$|\nu|(E) = \sup \left\{ \sum_i |\nu(E_i)| \mid E_1, E_2, ... \in \mathcal{B}(X) \text{ are pairwise disjoint}, E = \bigcup_i E_i \right\}.$$

Example 2 (Borel measures ([4], Ex 114))**.** *Let A be a measurable set.*

1. *The* Dirac measure *of A is $\delta_x(A) = \begin{cases} 1 & \text{if } x \in A, \\ 0 & \text{else.} \end{cases}$*

2. *The* counting measure *of A is $|A| = \begin{cases} \text{number of elements of } A & \text{if } A \text{ is finite,} \\ \infty & \text{else.} \end{cases}$*

3. *The m-dimensional* Hausdorff-measure *of A is*

$$\mathcal{H}^m(A) = \lim_{\epsilon \to 0} \inf \left\{ \sum_{i=1}^{\infty} \omega_m \left(\frac{\operatorname{diam} B_i}{2} \right)^m \mid A \subset \bigcup_{i=1}^{\infty} B_i, \operatorname{diam} B_i < \epsilon \right\},$$

where ω_m is the volume of the m-dimensional unit ball.

Definition 3 (Transformations of measures ([4], Def 116))**.** *Let (X, Σ_X) and (Y, Σ_Y) be measurable spaces, ν a measure $\nu : \Sigma_X \to \mathbb{R} \cup \{\infty\}$ and $B \in \Sigma_X$.*

1. *The restriction of ν to B is $\nu \llcorner B : \Sigma_X \to (-\infty, \infty]$ with $\nu \llcorner B(A) = \nu(A \cap B)$.*

2. *A function $f : X \to Y$ is called* measurable *if $f^{-1}(C) \in \Sigma_X$ for all $C \in \Sigma_Y$.*

3. *The* pushforward *of ν under a measurable function f is $f_{\#}\nu : \Sigma_Y \to (-\infty, \infty]$ with $f_{\#}\nu(C) = \nu(f^{-1}(C))$.*

Definition 4 (Radon measure ([3], Def 7)). *Let X be a topological space. A* finite Radon measure *on X is a real Borel measure ν whose total variation is a regular measure with $|\nu|(X) < \infty$. We denote the* space of finite Radon measures *on X by $\mathcal{M}(X)$. It is a normed vector space equipped with the norm $\|\nu\|_{\mathcal{M}} = |\nu|(X)$. Denote the set of non-negative finite Radon measures by $\mathcal{M}_+(X) \subset \mathcal{M}(X)$.*

Lemma 5 (Borel and Radon measure ([4], Thm 125)). *A real Borel measure on a σ-compact metric space is regular.*

Theorem 6 (Duality ([5], Thm 6.19, as adapted in [3])). *Let X be a locally compact Hausdorff space. Then the space $\mathcal{M}(X)$ can be identified with the dual space of $C_0(X)$, the latter being the completion of the space of compactly supported continuous functions with respect to the supremum norm $\| \cdot \|_\infty$. The duality pairing is given as*

$$\langle \nu, \phi \rangle = \int_X \phi(x) \, \mathrm{d}\nu(x),$$

and we have

$$\|\nu\|_{\mathcal{M}} = \sup_{\phi \in C_0(X), \|\phi\|_\infty \leq 1} \int_X \phi(x) \, \mathrm{d}\nu(x).$$

In particular, $\mathcal{M}(X)$ is a Banach space.

Definition 7 (Support of a measure ([3], Def 9)). *The* support *of a real Borel measure $\nu : \mathcal{B}(X) \to \mathbb{R}$ on a topological space X is defined as*

$$\mathrm{supp}(\nu) = \{x \in X \mid |\nu|(B) > 0 \text{ for each neighbourhood } B \text{ of } x\}.$$

Proposition 8 (Support properties ([3], Prop 10)). *Let X be a locally compact Hausdorff space and $\nu \in \mathcal{M}(X)$. Then the following holds.*

1. $\mathrm{supp}(\nu)$ *is closed and ν is concentrated on $\mathrm{supp}(\nu)$, i.e., $\nu(E) = \nu(E \cap \mathrm{supp}(\nu))$ for all $E \in \mathcal{B}(X)$.*

2. *If $\nu_n \overset{*}{\rightharpoonup} \nu$ in $\mathcal{M}(X)$ as $n \to \infty$ and if $\mathrm{supp}(\nu_n) \subset S$ for all n with $S \subset X$ closed, then $\mathrm{supp}(\nu) \subset S$.*

Lemma 9 (Equivalence of weak-$*$ and narrow convergence ([3], Lem 11)). *Let X be a complete separable metric space and $\nu_1, \nu_2, \ldots$ a sequence in $\mathcal{M}(X)$ weakly-$*$ converging to $\nu \in \mathcal{M}(X)$ such that $\mathrm{supp}(\nu_n) \subset S$ with $S \subset X$ compact. Then $\mathrm{supp}(\nu) \subset S$ and ν_n converges to ν also narrowly.*

Theorem 10 (Basic properties of pushforward measures ([3], Thm 14)). *Let (X, Σ_X) and (Y, Σ_Y) be measurable spaces, ν a measure $\nu : \Sigma_X \to \mathbb{R} \cup \{\infty\}$ and $f : X \to Y$ a measurable function. Then $f_{\#}\nu$ is a measure on (Y, Σ_Y) and a measurable function $g : Y \to \mathbb{R}$ in integrable with respect to $f_{\#}\nu$ if $g \circ f$ is integrable with respect to ν. If ν is non-negative, the converse also holds true. If both are integrable it holds that*

$$\int_Y g(y) \, \mathrm{d}f_{\#}\nu(y) = \int_X g(f(x)) \, \mathrm{d}\nu(x).$$

Further, if Y is a σ-compact metric space, then $f_\#\nu$ is a finite Radon measure on Σ_Y if ν is a finite Radon measure on Σ_X.

Proposition 11 (The pushforward as operator ([3], Prop 15)). *Let X, Y be locally compact Hausdorff spaces, X be a further complete, separable, σ-compact metric space and $f : X \to Y$ be continuous. Then*

$$f_\# : \mathcal{M}(X) \to \mathcal{M}(Y), \nu \mapsto f_\#\nu$$

is a well-defined linear operator with $\|f_\#\| \leq 1$. Further, the following holds.

1. *If $\nu \geq 0$, then $f_\#\nu \geq 0$ and $\|f_\#\nu\|_{\mathcal{M}(Y)} = \|\nu\|_{\mathcal{M}(X)}$.*

2. *$f_\#$ is continuous with respect to narrow convergence of measures.*

3. *$\operatorname{supp}(f_\#\nu) \subset \overline{f(\operatorname{supp}(\nu))}$.*

4. *If $\nu_1, \nu_2, \ldots \in \mathcal{M}(X)$ are such that $\nu_n \xrightarrow{\mathbf{n}} \nu \in \mathcal{M}(X)$ and $\operatorname{supp}(\nu_n) \subset S$ with S compact, then $\operatorname{supp}(f_\#\nu) \subset f(S)$ and $(f_\#\nu)_n \xrightarrow{\mathbf{n}} f_\#\nu$.*

Definition 12 (Product measure ([3], Def 16)). *Let X, Y be topological spaces, $\omega : \mathcal{B}(Z) \to \mathbb{R}$ a real Borel measure and $(\nu_z)_{z \in Z}$ a family of real Borel measures $\nu_z : \mathcal{B}(Z) \to \mathbb{R}$ such that for any $A \in \mathcal{B}(Z), Z \ni z \mapsto \nu_z(A)$ is ω-measurable. Then we define the* product measure

$$\nu_z \otimes_z \omega : \mathcal{B}(Y \times Z) \to \mathbb{R}$$

on the generator $\{A \times B \mid A \in \mathcal{B}(Y), B \in \mathcal{B}(Z)\}$ of $\mathcal{B}(Y \times Z)$ via

$$(\nu_z \otimes_z \omega)(A \times B) = \int_B \nu_z(A) \, \mathrm{d}\omega(z).$$

Similarly, we use the notation $\omega \otimes_z \nu_z$ for a corresponding product measure on $\mathcal{B}(Z \times Y)$.

Proposition 13 (Properties of the product measure ([3], Prop 17)). *Let X, Y, Z be σ- and locally compact metric spaces with Y, Z being complete and separable. Let $\omega \in \mathcal{M}_+(Z)$ and $\nu \in \mathcal{M}(X)$ be finite Radon measures with $\omega(Z) = 1$, and let $(f_z)_{z \in Z}$ be a family of functions $f_z : X \to Y$ such that $(x, z) \mapsto f_z(x)$ is continuous.*

Then the product measure $[f_z]_\#\nu \otimes_z \omega : \mathcal{B}(Y \times Z) \to \mathbb{R}$ is well-defined, a finite Radon-measre on $Y \times Z$, and the following holds.

1. *If $\nu \geq 0$, then $[f_z]_\#\nu \otimes_z \omega \geq 0$ and $\|[f_z]_\#\nu \otimes_z \omega\|_{\mathcal{M}(Y \times Z)} = \|\nu\|_{\mathcal{M}(X)}$.*

2. *$\nu \mapsto [f_z]_\#\nu \otimes_z \omega$ is continuous with respect to narrow convergence of measures.*

3. *$\operatorname{supp}([f_z]_\#\nu \otimes_z \omega) \subset \overline{F(\operatorname{supp}(\nu) \times \operatorname{supp}(\omega))}$.*

4. *Assume that Z is compact. Then, if $\nu_1, \nu_2, \ldots \in \mathcal{M}(X)$ are such that $\nu_n \xrightarrow{*} \nu \in \mathcal{M}(X)$ and $\operatorname{supp}(\nu_n) \subset S$ with S compact, it follows that $\operatorname{supp}([f_z]_\#\nu \otimes_z \omega) \subset F(S \times Z)$ and $[f_z]_\#\nu_n \otimes_z \omega(z) \xrightarrow{\mathbf{n}} [f_z]_\#\nu \otimes_z \omega$.*

The same holds true for product measure $\omega \otimes_z [f_z]_\#\nu : \mathcal{B}(Z \times Y) \to \mathbb{R}$.

Definition 14 (Subdifferential ([4], Def 98)). *The* subdifferential *of a convex functional $f : X \to (-\infty, \infty]$ in $x \in X$ is*

$$\partial f(x) = \{s \in X^* \mid f(y) \geq f(x) + \langle s, y - x \rangle\}.$$

Its elements are called subgradients.

Definition 15 (Legendre-Fenchel transform ([4], Def 101)). *The* Legendre-Fenchel conjugate *of a convex functional f on a Banach space X is*

$$f^* : X^* \to (-\infty, \infty], \quad f^*(y) = \sup_{x \in X} \langle y, x \rangle - f(x).$$

The pre-dual Legendre-Fenchel conjugate *of a convex functional f on a dual space X^* is*

$$^*f : X \to (-\infty, \infty], \quad {}^*f(y) = \sup_{y \in X^*} \langle y, x \rangle - f(y).$$

Theorem 16 (Fenchel-Rockafellar ([4], Thm 105)). *Let X, Y be Banach spaces, $F : Y \to (-\infty, \infty], G : X \to (-\infty, \infty]$ be proper and convex and let $A : X \to Y$ be bounded linear.*

1. *The* primal optimisation problem

$$p^* = \inf_{x \in X} F(Ax) + G(x)$$

   and its dual problem

$$d^* = \sup_{y \in Y^*} -F^*(y) - G^*(-A^*y^*)$$

   satisfy weak duality, *i.e., $d^* \leq p^*$.*

2. *Let* relint S *denote the* relative interior *of a set S (i.e., the interior relativ to $x + \{S - x\}$). If*

   a) *relint dom $F \cap A$ relint dom $G \neq \emptyset$ or*

   b) *$(-A^*)$ relint dom $F^* \cap$ relint dom $G^* \neq \emptyset$ and F, G are lower semi-continuous,*

   then strong duality $p^* = d^*$ holds. Under (2a) the supremum, under (2b) the infimum is attained.

Definition 17 (Fourier transform ([4], Def 157 & Rem 158)). *The* Fourier transform *of $f \in L^1(\mathbb{R}^n)$ with respect to $\xi \in \mathbb{R}^n$ is*

$$\mathcal{F}(\xi) = \int_{\mathbb{R}^n} f(x) e^{-ix \cdot \xi} \, \mathrm{d}x.$$

We write $\hat{f} = \mathcal{F}(f)$. If f is vector-valued, $\mathcal{F}$ is applied to each component. The inverse Fourier transform *is then defined as*

$$\mathcal{F}^{-1}(f)(x) = (2\pi)^{-n} \int_{\mathbb{R}^n} f(\xi) e^{ix \cdot \xi} \, \mathrm{d}\xi$$

and we write $\check{f} = \mathcal{F}^{-1}(f)$. The definition of $\mathcal{F}$ (and $\mathcal{F}^{-1}$) can be extended to Radon measures $\nu \in \mathcal{M}(\mathbb{R}^n)$ by

$$\mathcal{F}(\nu)(\xi) = \int_{R^n} e^{-ix \cdot \xi} \, \mathrm{d}\nu(x)$$

and, analogously,

$$\mathcal{F}^{-1}(\nu)(\xi) = (2\pi)^{-n} \int_{\mathbb{R}^n} e^{ix \cdot \xi} \, \mathrm{d}\nu(\xi).$$

Definition 18 (Truncated Fourier series). *The* truncated Fourier series *of a measure $\nu \in \mathcal{M}(\mathbb{R}^n)$ with respect to* truncation *or* cutoff frequency *$\Phi \geq 0$ is*

$$\mathcal{F}_\Phi(\nu) = \left(\int_{\mathbb{R}^n} e^{-i2\pi x \cdot \xi} \, \mathrm{d}\nu(x) \right)_{\xi \in \mathbb{Z}^n, \|\xi\|_\infty \leq \Phi}.$$

CHAPTER 2

Dimension-reduced reconstruction method

In this chapter, we define the dimension-reduced reconstruction method that was introduced by Holler et al. in [3]. In order to avoid unwieldy technicalities regarding Radon transforms on unbounded or open domains, we will define the problem in a compact setting. While some results would also hold for more general choices of domains, this setting is both simple and realistic. Thus, consider particles in a compact domain $\Omega \subset \mathbb{R}^d$, times in a compact temporal domain $\Sigma \subset \mathbb{R}$, and let $\Theta \subset S^{d-1}$ be a compact set of directions. Equip

- Ω with the Euclidian metric on $\mathbb{R}^d$ and

- Σ and Θ with the standard metrics on $\mathbb{R}$ and S^{d-1} respectively.

With this choice of metrics, these sets are compact and separable metric spaces, and we additionally equip

- Ω with Borel measure $\mathcal{L}^d$, the standard Lebesgue measure in $\mathbb{R}^d$ restricted to the underlying set, and

- Σ and Θ with general Borel probability measures $\mathcal{H}_\Sigma$ and $\mathcal{H}_\Theta$ with $\Theta = \operatorname{supp} \mathcal{H}_\Theta$.

Let $\mathcal{M}(\Omega)$ and $\mathcal{M}_+(\Omega)$ be the signed and the nonnegative Radon measures on Ω respectively, and let $\| \cdot \|_\mathcal{M}$ be the total variation norm. Furthermore, define the notation

$$\mathcal{M}(X)^I = \{ (\nu_i)_{i \in I} \mid \nu_i \in \mathcal{M}(X) \text{ for all } i \in I \}$$

for the product space with respect to set X and index set I.

2.1. Statement of the reconstruction problem

Beginning with the static problem in Ω, we can describe a set of N stationary particles x_i of masses m_i at locations $x_i \in \Omega$ via the linear combination

$$u = \sum_{i=1}^N m_i \delta_{x_i} \in \mathcal{M}(\Omega),$$

where δ_i is the Dirac delta. Let $f = \mathrm{Ob}u$ be an observation of u, obtained via an observation operator $\mathrm{Ob} : \mathcal{M}(\Omega) \to H$ for a Hilbert space H. In order to formally state reconstruction problems for both static particle configurations and dynamic configurations with measurements acquired at multiple measurement times, we define observation operators as follows.

Definition 19 (Observation operators ([3], Def 35)). *With H a Hilbert space and $\mathcal{T} \subset \Sigma$ a set of measurement times, for each $t \in \mathcal{T}$ define an* observation operator

$$\mathrm{Ob}_t : \mathcal{M}(\Omega) \to H$$

that is continuous with respect to the weak-∗ topology in $\mathcal{M}(\Omega)$ and H (or equivalently, that is the dual to a bounded linear operator $\mathrm{Ob}_t^* : H \to C(\Omega)$). The observation of a configuration $u \in \mathcal{M}(\Omega)^\Sigma$ is then given as

$$u \mapsto (\mathrm{Ob}_t u_t)_{t \in \mathcal{T}}.$$

In the case of a static configuration $u \in \mathcal{M}(\Omega)$, we simply drop the subscript t and denote the observation by

$$u \mapsto \mathrm{Ob}u.$$

We can then define a static optimisation problem

$$\min_{u \in \mathcal{M}_+(\mathbb{R}^d)} \|u\|_{\mathcal{M}} \quad \text{such that } \mathrm{Ob}u = f \tag{2.1}$$

for the reconstruction of particle configuration u from measurement f. Weak-∗-continuity of Ob is enforced to ensure that solutions of the reconstruction remain well-behaved under variations in configurations.

Consider now a dynamic configuration

$$\lambda = \sum_{i=1}^{N} m_i \delta_{(x_i, v_i)}.$$

in *phase space*, i.e., the space of positions and velocites, with linearly moving particles with initial locations $x_i \in \mathbb{R}^d$ and move vectors $v_i \in \mathbb{R}^d$. For our setting, we demand that all particles stay within domain Ω and no new particles enter for all times in Σ. Thus, we restrict choices of (x_i, v_i) to

$$\Lambda := \left\{ (x, v) \in \mathbb{R}^d \times \mathbb{R}^d \mid x + tv \in \Omega \text{ for all } t \in \Sigma \right\}. \tag{2.2}$$

To describe the current configuration at any point in time t, define a move operator that
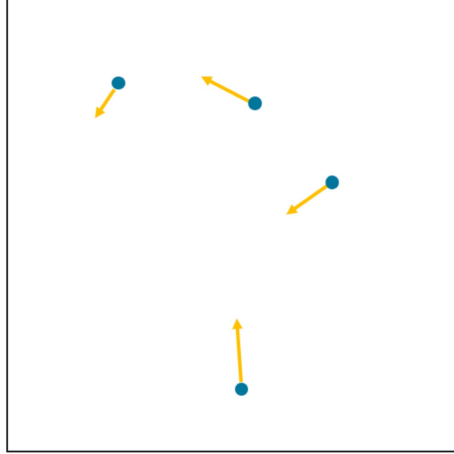
Figure 2.1.: Dynamic configuration of three particles with initial locations x_i (blue circles) and move vectors v_i (yellow arrows).

captures particle motion by mapping phase-space tuples of positions and velocities to time-dependent spatial positions.

Definition 20 (Move operator). *Let $t \in \Sigma$.*

- *Define the d-dimensional move operator for time t as*

$$\mathrm{Mv}_t^d : \mathcal{M}(\mathbb{R}^d \times \mathbb{R}^d) \to \mathcal{M}(\mathbb{R}^d);$$
$$\mathrm{Mv}_t^d \nu = [(x,v) \mapsto x + tv]_{\#} \lambda,$$

where $g_{\#}\nu$ is the pushforward of ν under g.

The move operator $\mathrm{Mv}^d : \mathcal{M}(\mathbb{R}^d \times \mathbb{R}^d) \to \mathcal{M}(\mathbb{R}^d \times \Sigma)$ *is then defined as*

$$\mathrm{Mv}^d \nu = \mathrm{Mv}_t^d \nu \otimes_t \mathcal{H}_\Sigma$$

and we set notation $\mathrm{Mv} := \mathrm{Mv}^1$.

- *Define the d-dimensional anglewise move operator for time t as*

$$\overline{\mathrm{Mv}_t^d} : \mathcal{M}(\Theta \times \mathbb{R}^d \times \mathbb{R}^d) \to \mathcal{M}(\Theta \times \mathbb{R}^d \times \Sigma);$$
$$\overline{\mathrm{Mv}_t^d} \nu = [(\theta, x, v) \mapsto (\theta, x + tv)]_{\#} \nu.$$

The anglewise move operator $\overline{\mathrm{Mv}^d} : \mathcal{M}(\Theta \times \mathbb{R}^d \times \mathbb{R}^d) \to \mathcal{M}(\Theta \times \mathbb{R}^d \times \Sigma)$ *is then defined as*

$$\overline{\mathrm{Mv}^d} \nu = \overline{\mathrm{Mv}_t^d} \nu \otimes_t \mathcal{H}_\Sigma$$

and we set notation $\overline{\mathrm{Mv}} := \overline{\mathrm{Mv}^1}$.

For a set of times $t \in \mathcal{T} \subset \mathbb{R}$, observations f_t and forward operators Ob_t, we now receive the dynamic reconstruction problem

$$\min_{\lambda \in \mathcal{M}_+(\mathbb{R}^d \times \mathbb{R}^d)} \|\lambda\|_{\mathcal{M}} \quad \text{such that } \mathrm{Ob}_t \mathrm{Mv}_t^d \lambda = f_t \text{ for all } t \in \mathcal{T}, \tag{2.3}$$

as first stated by Alberti et al. in [2]. Note that we simply have $\mathrm{Mv}_t^d \lambda = \sum_{i=1}^N m_i \delta_{x_i + tv_i}$. Besides gaining information on the particle movements additionally to their positions at the measurement times, the dynamic problem has the further advantage that the multiple observations f_t may contribute to better reconstruction results of current positions at each of the measurement times t as well. However, this is a high-dimensional problem and as such not very computationally feasible. In [3], Holler et al. propose a dimension-reduced method which employs Radon transforms to replace λ in the $2d$-dimensional space with snapshots $u_t = \mathrm{Mv}_t^d \lambda$ of the configuration at certain measurement times t and 2-dimensional projections onto directions θ in S^{d-1}, resulting in a reduction of the problem to $d + 1$ dimensions.

Definition 21 (Radon operators ([3], Def 19)). *Let $\theta \in \Theta$.*

- *Define the Radon transform with respect to θ as*

$$\mathrm{Rd}_\theta : \mathcal{M}(\mathbb{R}^d) \to \mathcal{M}(\mathbb{R});$$
$$\mathrm{Rd}_\theta \nu = [x \mapsto \theta \cdot x]_{\#} \nu.$$

The Radon transform $\mathrm{Rd} : \mathcal{M}(\mathbb{R}^d) \to \mathcal{M}(\Theta \times \mathbb{R})$ *is then defined as*

$$\mathrm{Rd}\nu = \mathcal{H}_\Theta \otimes_\theta \mathrm{Rd}_\theta \nu.$$

- *Define the timewise Radon transform with respect to θ as*

$$\overline{\mathrm{Rd}}_\theta : \mathcal{M}(\mathbb{R}^d \times \Sigma) \to \mathcal{M}(\mathbb{R} \times \Sigma);$$

$$\overline{\mathrm{Rd}}_\theta \nu = [(x,t) \mapsto (\theta \cdot x, t)]_\# \nu.$$

The timewise Radon transform $\overline{\mathrm{Rd}} : \mathcal{M}(\mathbb{R}^d \times \Sigma) \to \mathcal{M}(\Theta \times \mathbb{R} \times \Sigma)$ *is then defined as*

$$\overline{\mathrm{Rd}}\nu = \mathcal{H}_\Theta \otimes_\theta \overline{\mathrm{Rd}}_\theta \nu.$$

- *Define the joint Radon transform with respect to θ as*

$$\mathrm{Rj}_\theta : \mathcal{M}(\mathbb{R}^d \times \mathbb{R}^d) \to \mathcal{M}(\mathbb{R} \times \mathbb{R});$$

$$\mathrm{Rj}_\theta \nu = [(x,v) \mapsto (\theta \cdot x, \theta \cdot v)]_\# \nu.$$

The joint Radon transform $\mathrm{Rj} : \mathcal{M}(\mathbb{R}^d \times \mathbb{R}^d) \to \mathcal{M}(\Theta \times \mathbb{R} \times \mathbb{R})$ *is then defined as*

$$\mathrm{Rj}\nu = \mathcal{H}_\Theta \otimes_\theta \mathrm{Rj}_\theta \nu.$$

Let

$$\Gamma := \{(\theta \cdot x, \theta \cdot v) \mid (x,v) \in \Lambda, \theta \in \Theta\} \tag{2.4}$$

be the set of *position-velocity projections*, i.e., projections of measures in Λ with regard to directions Θ, and denote by

$$\Xi := \{\theta \cdot x \mid x \in \Omega, \theta \in \Theta\} \tag{2.5}$$

the set of projections of measures in Ω. We equip Λ, Γ and Ξ with the standard metrics of their underlying spaces, i.e., the Euclidian metric on $\mathbb{R}^d \times \mathbb{R}^d, \mathbb{R} \times \mathbb{R}$ and $\mathbb{R}$ respectively, making them compact and separable metric spaces. Indeed, all three are compact by their definition as the images of compact domains under continuous functions. Additionally equip Λ, Γ and Ξ with Borel measures $\mathcal{L}^d \times \mathcal{L}^d, \mathcal{L}^2$ and $\mathcal{L}^1$ for $\mathcal{L}^n$ the standard Lebesgue measure in $\mathbb{R}^n$ restricted to the respective underlying set.

Before defining the dimension-reduced problem, we first state some basic properties of Radon and move operators that will be relevant for the construction of the method and its quality as an approximation of the high-dimensional problem (2.3). Proofs of these properties are left out here for brevity but can be found in [3].

Remark 22 (Properties of Radon and move operators ([3], Rem 20 & 28)). *All of the defined Radon and move operators fulfill all three of the following properties. They*

(i) *define bounded linear operators with norm bounded by 1,*

(ii) *map non-negative measures to non-negative measures of the same norm, and*

(iii) *map L^1-functions to L^1 functions.*

The following explicit representations of the Radon operators hold true almost everywhere:

$$\nu \in L^1(\mathbb{R}^d): \quad \mathrm{Rd}_\theta \nu(s) = \int_{\{x \in \mathbb{R}^d \mid x \cdot \theta = s\}} \nu(x) \, \mathrm{d}\mathcal{H}^{d-1}(x),$$

$$\nu \in L^1(\mathbb{R}^d \times \Sigma): \quad \overline{\mathrm{Rd}}_\theta \nu(s,t) = \int_{\{x \in \mathbb{R}^d \mid x \cdot \theta = s\}} \nu(x,t) \, \mathrm{d}\mathcal{H}^{d-1}(x),$$

$$\nu \in L^1(\mathbb{R}^d \times \mathbb{R}^d): \quad \mathrm{Rj}_\theta \nu(s,r) = \int_{\{(x,y) \in \mathbb{R}^d \times \mathbb{R}^d \mid x \cdot \theta = s, y \cdot \theta = r\}} \nu(x,y) \, \mathrm{d}\mathcal{H}^{2d-2}(x,y).$$

Analogously, the following explicit representations of the move operators hold true almost everywhere:

$$\nu \in L^1(\mathbb{R}^n \times \mathbb{R}^n): \quad \mathrm{Mv}_t\nu(z) = \int_{\{(x,v)\in\mathbb{R}^n\times\mathbb{R}^n\,|\,x+tv=z\}} \nu(x,v)\,\mathrm{d}\mathcal{H}^n(x,v),$$

$$\nu \in L^1(\Theta \times \mathbb{R}^n \times \mathbb{R}^n): \quad \overline{\mathrm{Mv}}_t\nu(\theta,z) = \int_{\{(x,v)\in\mathbb{R}^n\times\mathbb{R}^n\,|\,x+tv=z\}} \nu(\theta,x,v)\,\mathrm{d}\mathcal{H}^n(x,v).$$

Proof. The result follows immediately from theorem 10 and propositions 11 and 13. $\qquad\square$

Proposition 23 (Radon and move operators for compactly supported measures ([3], Prop 22 & 30)). *With $\theta \in \Theta$ and $t \in \Sigma$ arbitrary, we have the following.*

Let

- *For $\nu \in \mathcal{M}(\mathbb{R}^d)$ with $\mathrm{supp}(\nu) \in \Omega$, it holds that*

$$\mathrm{supp}(\mathrm{Rd}_\theta\nu) \subset \Xi \text{ and } \mathrm{supp}(\mathrm{Rd}\nu) \subset \Theta \times \Xi.$$

- *For $\nu \in \mathcal{M}(\mathbb{R}^d \times \Sigma)$ with $\mathrm{supp}(\nu) \in \Omega \times \Sigma$, it holds that*

$$\mathrm{supp}(\overline{\mathrm{Rd}}_\theta\nu) \subset \Xi \times \Sigma \text{ and } \mathrm{supp}(\overline{\mathrm{Rd}}\nu) \subset \Theta \times \Xi \times \Sigma.$$

- *For $\nu \in \mathcal{M}(\mathbb{R}^d \times \mathbb{R}^d)$ with $\mathrm{supp}(\nu) \subset \Lambda$, it holds that*

$$\mathrm{supp}(\mathrm{Rj}_\theta\nu) \subset \Gamma \text{ and } \mathrm{supp}(\mathrm{Rj}\nu) \subset \theta \times \Gamma,$$

and additionally

$$\mathrm{supp}(\mathrm{Mv}_t^d\nu) \subset \Omega \text{ and } \mathrm{supp}(\mathrm{Mv}_t^d\nu) \subset \Omega \times \Sigma.$$

- *For $\nu \in \mathcal{M}(\Theta \times \mathbb{R}^2)$ with $\mathrm{supp}(\nu) \subset \Theta \times \Gamma$, it holds that*

$$\mathrm{supp}(\overline{\mathrm{Mv}}_t\nu) \subset \Theta \times \Xi \text{ and } \mathrm{supp}(\overline{\mathrm{Mv}}\nu) \subset \Theta \times \Xi \times \Sigma.$$

Using zero extension, the operator restrictions

$$\mathrm{Rd}_\theta : \mathcal{M}(\Omega) \to \mathcal{M}(\Xi) \text{ and } \mathrm{Rd} : \mathcal{M}(\Omega) \to \mathcal{M}(\Theta \times \Xi),$$

$$\overline{\mathrm{Rd}}_\theta : \mathcal{M}(\Omega \times \Sigma) \to \mathcal{M}(\Xi \times \Sigma) \text{ and } \overline{\mathrm{Rd}} : \mathcal{M}(\Omega \times \Sigma) \to \mathcal{M}(\Theta \times \Xi \times \Sigma),$$

$$\mathrm{Rj}_\theta : \mathcal{M}(\Lambda) \to \mathcal{M}(\Gamma) \text{ and } \mathrm{Rj} : \mathcal{M}(\Lambda) \to \mathcal{M}(\Theta \times \Gamma),$$

$$\mathrm{Mv}_t^d : \mathcal{M}(\Lambda) \to \mathcal{M}(\Omega) \text{ and } \mathrm{Mv}^d : \mathcal{M}(\Lambda) \to \mathcal{M}(\Omega \times \Sigma), \text{ as well as}$$

$$\overline{\mathrm{Mv}}_t : \mathcal{M}(\Theta \times \Gamma) \to \mathcal{M}(\Theta \times \Xi) \text{ and } \overline{\mathrm{Mv}} : \mathcal{M}(\Theta \times \Gamma) \to \mathcal{M}(\Theta \times \Xi \times \Sigma)$$

are all weakly-$*$ continuous.

Theorem 24 (Fourier slice theorem). *For $\nu \in \mathcal{M}(\mathbb{R}^d)$, we have*

$$\widehat{\mathrm{Rd}_\theta\nu}(\sigma) = \int_\mathbb{R} e^{-is\sigma}\,\mathrm{d}\mathrm{Rd}_\theta\nu(s) = \int_{\mathbb{R}^d} e^{-ix\cdot\theta\sigma}\,\mathrm{d}\nu(x) = \hat{\nu}(\theta\sigma) \quad \text{for all } \sigma \in \mathbb{R}, \theta \in S^{d-1}.$$

Proposition 25 (Injectivity of Radon and move operators ([3], Prop 26 & 34))**.** *If $\mathcal{H}_\Theta$ has a (non-zero) lower semi-continuous density with respect to the $(d-1)$-dimensional Hausdorff measure on S^{d-1}, then the Radon transform $\mathrm{Rd} : \mathcal{M}(\mathbb{R}^d) \to \mathcal{M}(\Theta \times \mathbb{R})$ is injective.*

Analogously, if $\mathcal{H}_\Sigma$ has a (non-zero) lower semi-continuous density with respect to the Lebesgue measure on $\mathbb{R}$, then the move operator $\mathrm{Mv} : \mathcal{M}(\mathbb{R} \times \mathbb{R}) \to \mathcal{M}(\mathbb{R} \times \Sigma)$ is injective.

Lemma 26 (Measure decomposition with projected lifting ([3], Lem 33))**.** *Let $u \in \mathcal{M}_+(\mathbb{R}^d)^\Sigma$ and $\gamma \in \mathcal{M}_+(\Theta \times \mathbb{R}^2)$ be such that*

$$\mathrm{Rd}u_t = \overline{\mathrm{Mv}}_t \gamma \ \text{for all } t \in \Sigma.$$

Then γ can be decomposed as

$$\gamma = \mathcal{H}_\Theta \otimes_\theta \gamma_\theta$$

with $(\gamma_\theta)_{\theta \in \Theta}$ a family of measures in $\mathcal{M}_+(\mathbb{R}^2)$ such that $\|\gamma_\theta\|_\mathcal{M} = \|\gamma\|_\mathcal{M}$. Further, we have $\|u_t\|_\mathcal{M} = \|\gamma\|_\mathcal{M}$ for all $t \in \Sigma$ and

$$\mathrm{Rd}_\theta u_t = \mathrm{Mv}_t \gamma$$

for every t and $\mathcal{H}_\Theta$-almost every θ.

With weak-$*$ continuity of Mv_t^d and Ob_t, a solution of (2.3) exists by standard arguments. By design of Λ and since the Mv_t^d map to non-negative measures by remark 22, we have that $\mathrm{Mv}_t^d \lambda \in \mathcal{M}_+(\Omega)$ for all $\lambda \in \mathcal{M}_+(\Lambda)$ and $t \in \Sigma$. Thus, we can formulate an equivalent problem to (2.3) using the snapshots u_t as

$$\min_{\substack{\lambda \in \mathcal{M}_+(\Lambda) \\ u \in \mathcal{M}_+(\Omega)^\Sigma}} \|\lambda\|_\mathcal{M} \quad \text{such that } \begin{cases} \mathrm{Mv}_t^d \lambda = u_t & \text{for all } t \in \Sigma, \\ \mathrm{Ob}_t u_t = f_t & \text{for all } t \in \mathcal{T}. \end{cases} \tag{2.6}$$

One can now perform dimension reduction by considering a projected version of the first constraint under the Radon transform on both sides, namely $\mathrm{Rd}\mathrm{Mv}_t^d = \mathrm{Rd}u_t$ for all $t \in \Sigma$, and using the following commutation property of Radon and move operators.

Lemma 27 (Commutation of Radon and move operators ([3], Lem 32))**.** *It holds that*

$$\overline{\mathrm{Rd}\mathrm{Mv}^d} = \overline{\mathrm{Mv}}\mathrm{Rj} \ \text{as well as} \ \mathrm{Rd}_\theta \mathrm{Mv}_t^d = \mathrm{Mv}_t \mathrm{Rj}_\theta \ \text{for all } t \in \mathbb{R}, \theta \in S^{d-1}.$$

Proof. Take $\nu \in \mathcal{M}_+(\mathbb{R}^d \times \mathbb{R}^d)$ and $\phi \in C_0(\Theta \times \mathbb{R} \times \Sigma)$. Then

$$\left\langle \overline{\mathrm{Rd}\mathrm{Mv}^d} \nu, \varphi \right\rangle = \int_{\mathbb{R}^d \times \mathbb{R}^d} \int_\Sigma \int_\Theta \varphi(\theta, \theta \cdot (x+ty), t) \, \mathrm{d}\mathcal{H}_\Theta(\theta) \, \mathrm{d}\mathcal{H}_\Sigma(t) \, \mathrm{d}\nu(x,y)$$

$$= \int_{\mathbb{R}^d \times \mathbb{R}^d} \int_\Theta \int_\Sigma \varphi(\theta, (\theta \cdot x) + t(\theta \cdot y), t) \, \mathrm{d}\mathcal{H}_\Sigma(t) \, \mathrm{d}\mathcal{H}_\Theta(\theta) \, \mathrm{d}\nu(x,y)$$

$$= \int_{\mathbb{R}^d \times \mathbb{R}^d} \int_\Theta (\overline{\mathrm{Mv}}^* \varphi)(\theta, \theta \cdot x, \theta \cdot y) \, \mathrm{d}\mathcal{H}_\Theta(\theta) \, \mathrm{d}\nu(x,y)$$

$$= \int_{\mathbb{R}^d \times \mathbb{R}^d} (\mathrm{Rj}^* \overline{\mathrm{Mv}}^* \varphi)(x,y) \, \mathrm{d}\nu(x,y) = \left\langle \overline{\mathrm{Mv}}\mathrm{Rj}\nu, \varphi \right\rangle,$$

where we applied Fubini's theorem since both $(\Sigma, \mathcal{H}_\Sigma)$ and $(\Theta, \mathcal{H}_\Theta)$ are finite measure spaces by assumption. The equality $\mathrm{Rd}_\theta \mathrm{Mv}_t^d = \mathrm{Mv}_t \mathrm{Rj}_\theta$ for all $t \in \mathbb{R}, \theta \in S^{d-1}$ follows similarly. $\quad\square$

Define the position-velocity projection $\gamma = \mathrm{Rj}\lambda$, then we get with lemma 27 that $\mathrm{RdMv}_t^d = \overline{\mathrm{Mv}}_t\gamma$. Note additionally that by remark 22 it holds that $\|\lambda\|_{\mathcal{M}} = \|\mathrm{Rj}\lambda\|_{\mathcal{M}}$ for all $\lambda \in \mathcal{M}_+(\Lambda)$. If Rd is injective, i.e., for appropriate choice of Θ as in proposition 25, we then have equivalence of (2.3) to

$$\min_{\substack{\lambda \in \mathcal{M}_+(\Lambda) \\ \gamma \in \mathcal{M}_+(\Theta \times \Gamma) \\ u \in \mathcal{M}_+(\Omega)^\Sigma}} \|\gamma\|_{\mathcal{M}} \quad \text{such that} \quad \begin{cases} \overline{\mathrm{Mv}}_t\gamma = \mathrm{Rd}u_t & \text{for all } t \in \Sigma, \\ \mathrm{Ob}_t u_t = f_t & \text{for all } t \in \mathcal{T}, \\ \mathrm{Rj}\lambda = \gamma. \end{cases} \tag{2.7}$$

The high-dimensional λ still remains present in the third constraint. By dropping it, we obtain a problem with variables of dimension at most $d+1$, the specific dimensionality depending on the particular choices of Θ and Σ. To include cases of noisy measurement data, introduce a softened contraint on the data in the form of the fidelity term

$$\frac{1}{2\alpha}\sum_{t \in \mathcal{T}} \|\mathrm{Ob}_t u_t - f_t\|^2,$$

where noise parameter $\alpha \in [0, \infty)$ and for $\alpha = 0$ we set $\frac{1}{2\alpha} = \infty$, thereby recovering the strict contraint in the noise-free case. The dimension-reduced reconstruction problem by Holler et al. is now stated as

$$\min_{\substack{\gamma \in \mathcal{M}_+(\Theta \times \Gamma) \\ u \in \mathcal{M}_+(\Omega)^\Sigma}} \|\gamma\|_{\mathcal{M}} + \frac{1}{2\alpha}\sum_{t \in \mathcal{T}} \|\mathrm{Ob}_t u_t - f_t\|_H^2 \text{ such that } \overline{\mathrm{Mv}}_t\gamma = \mathrm{Rd}u_t \text{ for all } t \in \Sigma. \quad (\mathrm{P}_\alpha(f))$$

In chapter 3, we will examine to what extent reconstruction properties transfer from the high-dimensional problem (2.3) to $\mathrm{P}_\alpha(f)$.

2.2. Well-posedness and equivalent formulations

Alternatively to $\mathrm{P}_\alpha(f)$, we can also formulate the problem for snapshots and position-velocity projections both defined in the respective product spaces $\mathcal{M}_+(\Omega)^\Sigma$ and $\mathcal{M}_+(\Gamma)^\Theta$. The product-topology formulation reads

$$\min_{\substack{\gamma \in \mathcal{M}_+(\Gamma)^\Theta \\ u \in \mathcal{M}_+(\Omega)^\Sigma}} \|\gamma_{\hat\theta}\|_{\mathcal{M}} + \frac{1}{2\alpha}\sum_{t \in \mathcal{T}} \|\mathrm{Ob}_t u_t - f_t\|_H^2 \text{ s.t. } \mathrm{Mv}_t^1\gamma_\theta = \mathrm{Rd}_\theta u_t \text{ for all } t \in \Sigma, \theta \in \Theta$$

$$(\Pi\text{-}P_{\sqrt{\delta}}(f^\delta))$$

with fixed arbitrary $\hat\theta \in \Theta$.

Remark 28 (Alternative problem formulations ([3], Prop 86, 87 & 88))**.** *If $(\Sigma, \mathcal{H}_\Sigma)$ is such that* $\mathrm{Mv} : \mathcal{M}(\Gamma) \to \mathcal{M}(\Xi \times \Sigma)$ *is injective, then $\Pi\text{-}P_{\sqrt{\delta}}(f^\delta)$ is equivalent to $\mathrm{P}_\alpha(f)$ in the sense that any solution (u, γ) of $\mathrm{P}_\alpha(f)$ admits a solution $(u, (\gamma_\theta)_{\theta \in \Theta})$ of $\Pi\text{-}P_{\sqrt{\delta}}(f^\delta)$, where $\gamma = \mathcal{H}_\Theta \otimes_\Theta \gamma_\theta$ is the unique decomposition of γ and vice versa.*

Variant $\Pi\text{-}P_{\sqrt{\delta}}(f^\delta)$ will be used in section 3.2 for the discussion of reconstruction properties of the method in the presence of noise, whereas formulation $\mathrm{P}_\alpha(f)$ is more convenient

for well-posedness and examining exact reconstruction in the noise-free setting, since the operation operator Ob_t can be applied at every $t \in \Sigma$ individually for the choice $\mathrm{Ob} \in \mathcal{M}_+(\Omega)^\Sigma$ and $\mathcal{M}_+(\Theta \times \Gamma)$ has the advantage of granting some regularity of γ with respect to $\theta \in \Theta$. A proof of remark 28 as well as a further formulation using the respective measure spaces $\mathcal{M}_+(\Omega \times \Sigma)$ and $\mathcal{M}_+(\Theta \times \Gamma)$ is also shown to exist and be equivalent to $\mathrm{P}_\alpha(f)$ under injectivity of Rd in Appendix A of [3] but is left out here for brevity.

Before analysing the reconstruction properties of the method in chapter 3, we state its well-posedness, the proof of which is also found in [3]. Stability of solutions is stated using $\mathcal{T}$-clustering points which we define first.

Definition 29 ($\mathcal{T}$-cluster point ([3])). *A sequence $((u^n, \gamma^n))_{n \in \mathbb{N}} \in \mathcal{M}_+(\Omega)^\Sigma \times \mathcal{M}_+(\Theta \times \Gamma)$ has a $\mathcal{T}$-cluster point at $(u, \gamma) \in \mathcal{M}_+(\Omega)^\Sigma \times \mathcal{M}_+(\Theta \times \Gamma)$ if there exists a subsequence $((u_t^{n_k}, \gamma^{n_k}))_{n_k}$ such that*

1. $u_t^{n_k} \overset{*}{\rightharpoonup} u_t$ for all $t \in \mathcal{T}$ and $\gamma^{n_k} \overset{*}{\rightharpoonup} \gamma$ as $k \to \infty$, and

2. for all $t \in \Sigma \setminus \mathcal{T}$, the measure u is a (standard) cluster point of the subsequence $u_t^{n_k}$ with respect to weak-$*$-convergence.

We then have the following result for the well-posedness of the dimension-reduced method.

Proposition 30 (Well-posedness ([3], Prop 38)). *Let $(f_t)_{t \in \mathcal{T}} \in H^{|\mathcal{T}|}$ and $\alpha \in [0, \infty)$. If $\alpha = 0$, assume f to be such that there exists $\lambda \in \mathcal{M}_+(\Lambda)$ with $\mathrm{Ob}_t \mathrm{Mv}_t^d \lambda = f_t$ for all $t \in \mathcal{T}$. Then problem $\mathrm{P}_\alpha(f)$ has a solution. Moreover, for $\alpha > 0$ the solutions are stable in the following sense:*

Let $(f^n)_{n \in \mathbb{N}}$ be a sequence of $f^n \in H^{|\mathcal{T}|}$ with $f_t^n \to f_t \in H$ for all $t \in \mathcal{T}$ as $n \to \infty$, and let $((u^n, \gamma^n))_{n \in \mathbb{N}}$ be a corresponding sequence of solutions to $\mathrm{P}_\alpha(f^n)$. Then the following holds:

1. The sequence $((u^n, \gamma^n))_{n \in \mathbb{N}}$ has a $\mathcal{T}$-cluster point.

2. Any $\mathcal{T}$-cluster point (u, γ) of the sequence $((u^n, \gamma^n))_{n \in \mathbb{N}}$ is a solution of $\mathrm{P}_\alpha(f)$.

3. If the solution (u, γ) to $\mathrm{P}_\alpha(f)$ is unique, the entire sequences u_t^n and γ^n weakly-$*$ converge to u_t and γ respectively, for all $t \in \Sigma$.

CHAPTER 3

Properties of the method

We will now establish reconstruction properties of the dimension reduced method. In particular, we will derive conditions for exact reconstruction in the case of noise-free measurements $f^\dagger$ in section 3.1, and error estimates in the case of measurements f^δ with noise level δ in section 3.2. As before, this chapter closely follows [3].

3.1. Reconstruction properties in the absence of noise

First consider the noise-free setting. In the following, we denote by $\lambda^\dagger \in \mathcal{M}_+(\Lambda)$ a ground truth configuration with noise-free measurements $f_t^\dagger = \mathrm{Ob}_t \mathrm{Mv}_t^d \lambda^\dagger$, ground truth snapshots $u_t^\dagger = \mathrm{Mv}_t^d \lambda^\dagger$ for times $t \in \mathcal{T}$, and ground truth position-velocity projections $\gamma_\theta^\dagger = \mathrm{Rj}_\theta \lambda^\dagger$ for directions $\theta \in \Theta$.

Configurations can be reconstructed exactly via $\mathrm{P}_0(f^\dagger)$ under certain geometric conditions, namely the absence of so-called ghost particles, as first defined in [2], and coincidences.

Definition 31 (Coincidence and ghost particle ([3], Def 40))**.** *Let $S = \{(x_i, v_i) \mid i = 1, \ldots, N\} \subset \mathbb{R}^n \times \mathbb{R}^n$ be a particle configuration and $\mathcal{T}' \subset \mathbb{R}$ a set of times. Define*

$$L_{i,t} = \{(x, v) \in \mathbb{R}^n \times \mathbb{R}^n \mid x + tv = x_i + tv_i\}.$$

Then configuration S admits

1. *a* coincidence *with respect to $\mathcal{T}'$ if two distinct particles coincide in their location at a time in $\mathcal{T}'$, i.e., if $L_{i,t} \cap L_{j,t} \neq \emptyset$ for any two distinct particles $i \neq j$ and time $t \in \mathcal{T}'$.*

2. *a* ghost particle *with respect to $\mathcal{T}'$ if there exist a point $(x, v) \in \mathbb{R}^n \times \mathbb{R}^n \setminus S$ and distinct indices $(i_t)_{t \in \mathcal{T}'} \subset \{1, \ldots, N\}$ such that*

$$\bigcap_{t \in \mathcal{T}'} L_{i_t, t} = \{(x, v)\}.$$

The set of ghost particles of S w.r.t. $\mathcal{T}'$ is denoted $G(S, \mathcal{T}')$.

Note. *We further denote*

$$\mathrm{Rj}_\theta(S) := \{(\theta \cdot x, \theta \cdot v) \mid (x, v) \in S\}$$

for any $S \subset \mathbb{R}^n \times \mathbb{R}^n$ and $\theta \in \Theta$, and

$$L_{i,t}(\theta) := \mathrm{Rj}_\theta(L_{i,t}) = \{(x, v) \in \mathbb{R} \times \mathbb{R} \mid x + tv = \theta \cdot x_i + t\theta \cdot v_i\}.$$

a) Coincidence at time $t = 2$.   b) Ghost particle w.r.t. $\mathcal{T} = \{2, 5\}$.
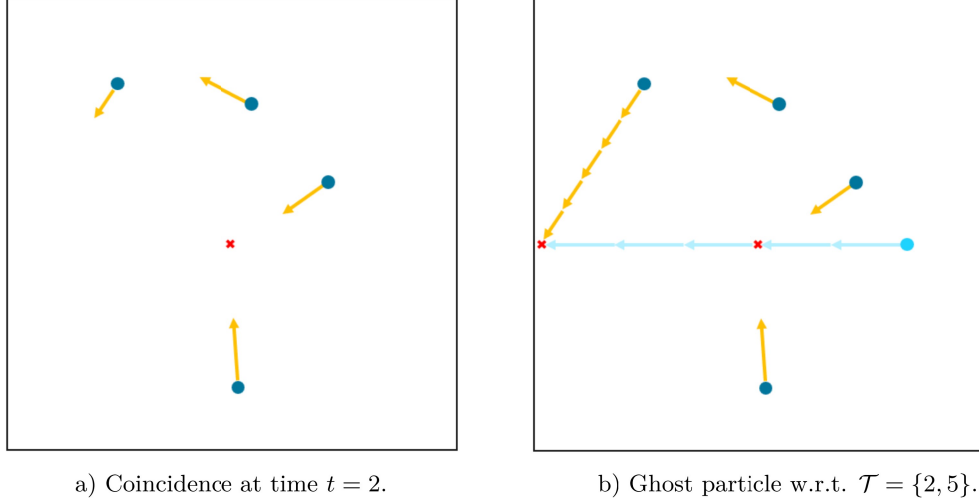
Figure 3.1.: Illustration of coincidence and ghost particle, where initial particle locations x_i and velocites v_i are depicted as blue circles and yellow arrows respectively, with red crosses marking the points in space at which current locations coincide at certain times. Note: The light blue particle in b) is a ghost particle with respect to $\mathcal{T} = \{2, 5\}$ but would not be considered one with respect to set of times $\mathcal{T} = \{2, 3, 4, 5\}$, as it does not create any coincidences with configuration particles at times $t = 3, 4$.

Note without proof that freedom from coincidences and ghost particles is almost always preserved under projection via Rj_θ.

Lemma 32 (Coincidences and ghost particles in projections ([3], Lem 45 & 47))**.** *Let S be a particle configuration and $\mathcal{T}'$ a finite set of times.*

1. *If S is free of coincidences at all times in $\mathcal{T}'$, then $\mathrm{Rj}_\theta(S)$ is also free of coincidences in $\mathcal{T}'$ for $\mathcal{H}^{d-1}$-almost all $\theta \in S^{d-1}$.*

2. *If S is free of ghost particles w.r.t. $\mathcal{T}'$, then for $\mathcal{H}^{d-1}$-almost all $\theta \in S^{d-1}$ the projected configuration $\mathrm{Rj}_\theta(S)$ is free of ghost particles w.r.t. $\mathcal{T}'$ as well.*

In order to show exact reconstruction as a property extending from the static to the dynamic problem, we first define exact reconstructibility for the static problem.

Definition 33 (Exact reconstruction of the static problem ([3], Def 41))**.** *The static reconstruction problem for a time $t \in \mathcal{T}$ and a noise-free measurement $f^\dagger$ is*

$$\min_{u \in \mathcal{M}_+(\Omega)} \|u\|_{\mathcal{M}} \ such \ that \ \mathrm{Ob}_t u_t = f_t^\dagger. \qquad (\mathrm{P}_{\mathrm{stat}}^t(f_t^\dagger))$$

The static problem reconstructs exactly if $u_t^\dagger$ is the unique solution.

3.1.1. General results for exact reconstruction

We will obtain reconstruction results in the noise-free setting in three steps:

1. Show that 'good' snapshots, i.e., snapshots u_t at times t at which the static problem reconstructs exactly, also reconstruct exactly for the dynamic problem as well (theorem 34).

2. From the exact reconstruction of these snapshots, infer exact reconstruction of position-velocity projections γ_θ under appropriate conditions on the direction θ (theorem 35).

3. Lastly, obtain conditions for exact reconstruction of arbitrary snapshots from the first two steps (theorem 36).

First, consider good snapshots.

Theorem 34 (Exact reconstruction of good snapshots ([3], Thm 42)). *Let (u, γ) be a solution of $\mathrm{P}_0(f^\dagger)$ and let $\mathcal{T}' \subset \mathcal{T}$ be a subset of times at which the static problem $\mathrm{P}_{stat}^t(f_t^\dagger)$ reconstructs exactly. Then $u_t = u_t^\dagger$ for all $t \in \mathcal{T}'$.*

Proof. Let (u, γ) be a solution of $\mathrm{P}_0(f^\dagger)$ and consider any time $t \in \mathcal{T}'$. Since $(u^\dagger, \gamma^\dagger)$ is admissible for $\mathrm{P}_0(f^\dagger)$ but (u, γ) is the solution, it must hold that

$$\|\gamma\|_{\mathcal{M}} \leq \|\gamma^\dagger\|_{\mathcal{M}}.$$

Since both solutions must satisfy the constraint $\overline{\mathrm{M}}\mathrm{v}_t \gamma = \mathrm{R}\mathrm{d}u_t$ and both Radon and move operators map non-negative measures to non-negative measures of the same norm by remark 22, we have

$$\|u_t\|_{\mathcal{M}} = \|\gamma_t\|_{\mathcal{M}} \leq \|\gamma_t^\dagger\|_{\mathcal{M}} = \|u_t^\dagger\|_{\mathcal{M}},$$

and since u is by definition admissible, it is a solution of $\mathrm{P}_{\mathrm{stat}}^t(f_t^\dagger)$. But by choice of $t \in \mathcal{T}'$, the static problem reconstructs exactly and thus $u_t = u_t^\dagger$ must hold. $\square$

Theorem 35 (Exact reconstruction of position-velocity projections ([3], Thm 43)). *Let $\mathcal{T}'$ and (u, γ) as in theorem 34, with disintegration $\gamma = \mathcal{H}_\Theta \otimes_\theta \gamma_\theta$. Let $\lambda^\dagger$ be a ground truth configuration and define*

$$\Theta' := \left\{ \theta \in \Theta \mid \mathrm{Rj}_\theta(\mathrm{supp}\,\lambda^\dagger) \text{ is free of coincidences and ghost particles w.r.t. } \mathcal{T}' \right\}.$$

Then we have $\gamma_\theta = \gamma_\theta^\dagger$ for $\mathcal{H}_\Theta$-almost all $\theta \in \Theta'$.

Proof. We have for $\mathcal{H}_\Theta$-almost all $\theta \in \Theta'$ that

$$\|\gamma_\theta\|_{\mathcal{M}} = \|\gamma\|_{\mathcal{M}} \text{ and } \mathrm{Rd}_\theta u_t = \mathrm{Mv}_i \gamma_\theta \text{ for all } t \in \Sigma \tag{3.1}$$

by lemma 26. For $\theta \in \Theta'$ chosen such that this holds, define the reconstruction error

$$\xi = \gamma_\theta - \gamma_\theta^\dagger \in \mathcal{M}(\mathbb{R}^d)$$

and let $\mathrm{supp}\,\lambda^\dagger = \{(x_i, v_i) \mid i = 1, \ldots, N\}$. Consider the Lebesgue decomposition $\xi = \xi_a + \xi_s$ with respect to $\gamma_\theta^\dagger$ with $\xi_s \perp \gamma_\theta^\dagger$ and $\xi_a = \sum_{i=1}^N \beta_i \delta_{(\theta \cdot x_i, \theta \cdot v_i)}$ for weights $\beta_i \in \mathbb{R}$. For $t \in \mathcal{T}'$ define

$$\tilde{q}_t : \mathbb{R} \to \mathbb{R}, \quad \tilde{q}_t(s) = \begin{cases} \mathrm{sgn}\,\beta_i & \text{if } s = \theta \cdot (x_i + t v_i) \\ 0 & \text{else,} \end{cases}$$

and let

$$q : \mathbb{R}^2 \to \mathbb{R}, \quad q(y, w) = \frac{1}{|\mathcal{T}'|} \sum_{t \in \mathcal{T}'} \tilde{q}_t(y + tw).$$

It can easily be seen that $|\tilde{q}_t(s)| \leq 1$ for all $s \in \mathbb{R}$ and, since $\mathrm{Rj}_\theta(\mathrm{supp}\, \lambda^\dagger)$ does not admit any coincidences or ghost particles by choice of θ, we have

$$|q(y, w)| < 1 \text{ for all } (y, w) \in \mathbb{R}^2 \setminus \mathrm{supp}\, \lambda^\dagger. \tag{3.2}$$

Furthermore, as $\mathrm{P}^t_{\mathrm{stat}}(f_t^\dagger)$ reconstructs exactly at all $t \in \mathcal{T}'$, we have

$$\mathrm{Mv}_t \gamma_\theta = \mathrm{Rd}_\theta u_t \overset{(\mathrm{thm.34})}{=} \mathrm{Rd}_t u_t^\dagger = \mathrm{Mv}_t \gamma_\theta^\dagger$$

and thus $\mathrm{Mv}_t \xi = \mathrm{Mv}_t \gamma_\theta - \mathrm{Mv}_t \gamma_\theta^\dagger = 0$ for all $t \in \mathcal{T}'$. From this and result (3.2) for q, it follows that

$$\begin{aligned}
0 &= \frac{1}{|\mathcal{T}'|} \sum_{t \in \mathcal{T}'} \int_{\mathbb{R}} \tilde{q}_t \, \mathrm{dMv}_t \xi \\
&= \int_{\mathbb{R}^2} q \, \mathrm{d}\xi \\
&= \int_{\mathbb{R}^2} q \, \mathrm{d}\xi_a + \int_{\mathbb{R}^2} q \, \mathrm{d}\xi_s = \sum_{i=1}^{N} |\beta_i| + \int_{\mathbb{R}} q \, \mathrm{d}\xi_s.
\end{aligned} \tag{3.3}$$

For $\xi_s = 0$, the rest is trivial, as then $\|\xi_a\|_{\mathcal{M}} = \sum_{i=1}^{N} |\beta_i| \overset{(3.3)}{=} 0$ and thus $\xi = \xi_a + \xi_s = 0$. So assume that $\xi_s \neq 0$. Then

$$\|\xi_a\|_{\mathcal{M}} = \sum_{i=1}^{N} |\beta_i| \overset{(3.3)}{=} - \int_{\mathbb{R}^2} q \, \mathrm{d}\xi_s \overset{(3.2)}{<} \|\xi_s\|_{\mathcal{M}}. \tag{3.4}$$

Consider that $\gamma_\theta^\dagger + \xi_a \perp \xi_s$ by definition of ξ_a and ξ_s. With optimality of γ, lemma 26 and choice of θ, we then receive the contradiction

$$\begin{aligned}
\|\gamma_\theta^\dagger\|_{\mathcal{M}} &\overset{(3.4)}{<} \|\gamma_\theta^\dagger\|_{\mathcal{M}} - \|\xi_a\|_{\mathcal{M}} + \|\xi_s\|_{\mathcal{M}} \\
&\leq \|\gamma_\Theta^\dagger + \xi_a\|_{\mathcal{M}} + \|\xi_s\|_{\mathcal{M}} \\
&= \|\gamma_\theta^\dagger + \xi\|_{\mathcal{M}} \\
&= \|\gamma_\theta\|_{\mathcal{M}} \\
&= \|\gamma\|_{\mathcal{M}} \\
&\leq \|\gamma^\dagger\|_{\mathcal{M}} = \|\gamma_\theta^\dagger\|_{\mathcal{M}}.
\end{aligned}$$

Thus, $\xi_s = 0$ must hold and $\gamma_\theta = \gamma_\theta^\dagger$ follows as above. $\qquad \square$

We now have that

$$\mathrm{Rd}_\theta u_t = \mathrm{Mv}_t \gamma_\Theta = \mathrm{Mv}_t \gamma_\theta^\dagger = \mathrm{Rd}_\theta u_t^\dagger \text{ for all } t \in \Sigma, \text{ for } \mathcal{H}_\Theta\text{-almost all } \theta \in \Theta', \tag{3.5}$$

from which the result for arbitrary snapshots follows immediately.

Theorem 36 (Exact reconstruction of arbitrary snapshots ([3], Thm 44)). *Let $\mathcal{T}'$ and (u, γ) as in theorem 34 and consider an arbitrary time $t \in \Sigma$. Let Θ' be as defined in theorem 35. If $u_t^\dagger$ is uniquely determined by the restriction $(\mathcal{H}_\Theta \llcorner \Theta') \otimes_\Theta \mathrm{Rd}_\theta u_t^\dagger$ of the Radon transform to Θ', then $u_t = u_t^\dagger$.*

We know by lemma 32 that Θ' differs from Θ only by a $\mathcal{H}^{d-1}$-nullset. Thus, if $\Theta = S^{d-1}$ and $\mathcal{H}_\Theta$ is the $(d-1)$-dimensional Hausdorff measure, we receive that $(u^\dagger, \gamma^\dagger)$ reconstructs exactly. This is formally stated in theorem 42.

3.1.2. Exact reconstruction for a finite set of directions

In this section, we examine the case of finitely many directions Θ and derive the minimum numbers of directions and times of exact reconstructibility from the static problem that are needed for exact reconstruction of all snapshots of a configuration. Since difficulty of reconstruction increases with the amount of particles considered, fix some $N \in \mathbb{N}$ and consider configurations of at most N Dirac masses.

We first introduce a useful property of the two-dimensional Radon transform.

Proposition 37 (Equivalence of move and radon operators). *For a measure $\nu \in \mathcal{M}_+(\mathbb{R}^2)$, the move operator is equivalent to the Radon transform via*

$$\mathrm{Mv}_t \nu = \left[s \mapsto \sqrt{1+t^2} s \right]_\# \left(\mathrm{Rd}_{\frac{(1,t)}{\sqrt{1+t^2}}} \nu \right).$$

To obtain the desired results, Holler et al. in [3] generalise a theorem on the X-ray transform by Hajós and Rényi [6] to the Radon transform.

Proposition 38 (Determination of a discrete measure from Radon transforms ([3], Prop 48 & Cor 49)). *Let $\Theta \subset S^{d-1}$ be a set of $(d-1)N+1$ directions, any d of them being linearly independent. Then a measure $\nu \in \mathcal{M}_+(\mathbb{R}^d)$ with support in at most N distinct points is uniquely determined by the Radon transforms $\mathrm{Rd}_\theta \nu$ for $\theta \in \Theta$.*

A simple proof of prop 38 following the idea of a proof of Hajós and Rényi's theorem from [7] is given in [3]. The sought-after reconstruction property now follows easily.

Proposition 39 (Exact reconstruction from a finite set of directions ([3], Cor 50)). *Let $\lambda^\dagger$ be a configuration of at most N particles and let $\Theta \subset S^{d-1}$ be a subset of $(d-1)N+1$ directions, any d of which are linearly independent, with $\mathcal{H}_\Theta$ the counting measure on Θ. Let $\mathcal{T}'$ be a set of $N+1$ times at which $\mathrm{P}_{stat}^t(f_t^\dagger)$ reconstructs exactly. For (u, γ) a solution of $\mathrm{P}_0(f^\dagger)$ we then have that $(u, \gamma) = (u^\dagger, \gamma^\dagger)$.*

Proof. By theorem 34, we have that $u_t = u_l^\dagger$ for all $t \in \mathcal{T}'$, and thus

$$\mathrm{Mv}_t \gamma_\theta = \mathrm{Rd}_\theta u_t = \mathrm{Rd}_\theta u_t^\dagger = \mathrm{Mv}_t \gamma_\theta^\dagger \text{ for all } t \in \mathcal{T}', \theta \in \Theta. \tag{3.6}$$

By proposition 37, it follows that

$$\mathrm{Rd}_{\frac{(1,t)}{\sqrt{1+t^2}}} \gamma_\theta = \mathrm{Rd}_{\frac{(1,t)}{\sqrt{1+t^2}}} \gamma_\theta^\dagger \text{ for all } \theta \in \Theta, \tag{3.7}$$

and thus, since $|\mathcal{T}'| = N + 1$, we obtain $\gamma_\theta = \gamma_\theta^\dagger$ for all $\theta \in \Theta$ by lemma 38. Then we have

$$\mathrm{Rd}_\vartheta u_t = \mathrm{Mv}_t \gamma_\theta = \mathrm{Mv}_t \gamma_\theta^\dagger = \mathrm{Rd}_\theta u_t^\dagger \text{ for all } t \in \Sigma, \theta \in \Theta, \tag{3.8}$$

and since $|\Theta| = (d-1)N + 1$, applying lemma 38 again gives the result that $u_t = u_t^\dagger$ is uniquely determined for all $t \in \Sigma$. $\qquad\square$

Exact reconstruction of most configurations

Beyond the results obtained for all configurations of N points so far, it is very practically relevant to consider less strict conditions under which exact reconstruction follows for 'most' configurations. Here, we take 'most' to mean all but a Lebesgue-nullset. Indeed, we can show that for most configurations only three times for which snapshots are exactly reconstructible from the static problem already suffice to show exact reconstruction of the entire configuration from $\mathrm{P}_0(f^\dagger)$. This will be formally stated and proven in section 3.1.3 using the following results.

Proposition 40 (Determination of measure from Radon transforms ([3], Prop 51)). *Let $\Theta \subset S^{d-1}$ be a set of $d+1$ directions, any d of which are linearly independent, and consider any probability distribution of N points in $\mathbb{R}^d$ that is absolutely continuous with respect to the Nd-dimensional Lebesgue measure. Then almost surely a set S of N points is uniquely determined among all subsets of $\mathbb{R}^d$ by its Radon transforms $\mathrm{Rd}_\theta S$ for $\theta \in \Theta$.*

Proof. For $S = \{x_1, \ldots, x_N\} \subset \mathbb{R}^d$, denote by

$$H_\theta^i = \{x \in \mathbb{R}^d \mid (x - x_i) \cdot \theta = 0\}$$

the hyperplane through x_i that is orthogonal to $\theta \in \Theta$. Then S can be uniquely determined if

$$\bigcap_{\theta \in \Theta} H_\theta^{\iota(\theta)} = \begin{cases} \{x_i\} & \text{for } \iota \equiv i \text{ constant}, \\ \emptyset & \text{else}, \end{cases} \tag{3.9}$$

where ι is a mapping $\iota : \Theta \to \{1, \ldots, N\}$. Now, for any non-constant ι, the intersection of the hyperplanes is non-empty iff there exists a solution $x \in \mathbb{R}^d$ to

$$\begin{pmatrix} \theta_1 \\ \vdots \\ \theta_{d+1} \end{pmatrix} x = \begin{pmatrix} \theta_1 \cdot x_{\iota(\theta_i)} \\ \vdots \\ \theta_{d+1} \cdot x_{\iota(\theta_{d+1})} \end{pmatrix}$$

and the set of solutions to this overdetermined equation system is at most $(Nd - 1)$-dimensional, i.e., a Lebesgue-nullset. $\qquad\square$

Corollary 41 (Determination of measure from Radon transforms ([3], Cor 52)). *Let $\Theta \subset S^{d-1}$ be a set of $d+1$ directions, any d of which are linearly independent, and consider any probability distribution of discrete non-negative measures $\sum_{i=1}^N a_i \delta_{x_i}$ such that the induced distribution of their N support points is absolutely continuous with respect to the Nd-dimensional Lebesgue measure. Then almost surely such a measure ν is uniquely determined among all non-negative Radon measures by its Radon transforms $\mathrm{Rd}_\theta \nu$ for $\theta \in \Theta$.*

Proof. By proposition 40, the support of ν is almost surely uniquely determined. If it is then so are the weights a_i. Indeed: Let $\nu' = \sum_{i=1}^{N} b_i \delta_{x_i}$ be a measure with the same support and Radon transforms $\mathrm{Rd}_\theta \nu' = \mathrm{Rd}_\theta \nu$ as ν for all $\theta \in \Theta$ and define

$$\xi_+ = \sum_{\substack{i=1, \\ a_i > b_i}} (a_i - b_i)\delta_{x_i}, \qquad \xi_- = -\sum_{\substack{i=1, \\ a_i < b_i}} (a_i - b_i)\delta_{x_i},$$

then $0 = \mathrm{Rd}_\theta(\nu' - \nu) = \mathrm{Rd}_\theta(\xi_+ - \xi_-)$ for all $\theta \in \Theta$. Since the supports of ξ_+ and ξ_- are subsets of $\mathrm{supp}\, \nu$ and as such contain at most N points, proposition 40 gives that they are almost surely uniquely determined by their Radon transforms $\mathrm{Rd}_\theta \xi_+ = \mathrm{Rd}_\theta \xi_-$, and thus $\mathrm{supp}\, \xi_+ = \mathrm{supp}\, \xi_-$. Since $\mathrm{supp}\, \xi_+ \cap \mathrm{supp}\, \xi_- = \emptyset$ must hold by definition, it follows that $\xi_+ = \xi_- = 0$ and we have $\nu' = \nu$. $\qquad\square$

3.1.3. Exact reconstruction in the noise-free setting

The exact reconstruction properties in the noise-free setting, for $\mathcal{H}_\Theta$ a Hausdorff or counting measure, are summarised in the following theorems.

Theorem 42 (Exact reconstruction for noise-free data - Hausdorff measure ([3], Thm 3)). *Take $\mathcal{H}_\Theta$ to have a nonzero lower semi-continuous density with respect to the $(d-1)$-dimensional Hausdorff measure on S^{d-1}. Let $\mathcal{T}' \subset \mathcal{T}$ be a non-empty set of times t at which $\mathrm{P}_{stat}^t(f_t^\dagger)$ reconstructs exactly, and let ground truth configuration $\lambda^\dagger$ be free of coincidences and ghost particles with respect to $\mathcal{T}'$. Then we have for solution (u, γ) of $\mathrm{P}_0(f^\dagger)$ that*

1. $u_t = u_t^\dagger$ for all $t \in \Sigma$, and

2. $\gamma_\theta = \gamma_\theta^\dagger$ for $\mathcal{H}_\Theta$-almost all $\theta \in \Theta$.

Proof. Consider the subset

$$\Theta' = \left\{ \theta \in \Theta \mid \mathrm{Rj}_\theta(\mathrm{supp}\, \lambda^\dagger) \text{ is free of coincidences and ghost particles w.r.t. } \mathcal{T}' \right\}$$

of directions. By lemma 32, it contains $\mathcal{H}^{d-1}$-almost all $\theta \in \Theta$. Since $\mathcal{H}_\Theta$ is absolutely continuous with respect to $\mathcal{H}^{d-1}$, this gives that Θ' contains $\mathcal{H}_\Theta$-almost all $\theta \in \Theta$. For (u, γ) the solution of $\mathrm{P}_0(f_t^\dagger)$, we have by theorem 34 that

$$u_t = u_t^\dagger \text{ for all } t \in \mathcal{T}'.$$

Let $\gamma = \mathcal{H}_\Theta \otimes_\theta \gamma_\theta$ be a disintegration of γ as in lemma 26, then it follows from theorem 35 that

$$\gamma_\theta = \gamma_\theta^\dagger \text{ for } \mathcal{H}_\Theta\text{-almost all } \theta \in \Theta.$$

Lastly, with injectivity of the Radon transform we have that $u_t^\dagger$ is uniquely determined by $\left(\mathcal{H}_\Theta \llcorner \Theta' \otimes_\theta \mathrm{Rd}_\theta u_t^\dagger \right)$. With this the conditions of theorem 36 are fulfilled and it follows that $u_t = u_t^\dagger$ holds for all $t \in \Sigma$. $\qquad\square$

Theorem 43 (Exact reconstruction for noise-free data - Counting measure ([3], Thm 4)). *Take $\mathcal{H}_\Theta$ to be the counting measure on the set Θ of $d+1$ directions, any d of which are*

linearly independent. Let ground truth configuration $\lambda^\dagger$ be such that its location vector is distributed according to a probability distribution which is absolutey continuous with respect to the $2Nd$-dimensional Lebesgue measure. If there exists a set $\mathcal{T}'$ three times t at which $\mathrm{P}^t_{stat}(f^\dagger_t)$ reconstructs exactly, then almost surely the solution (u, γ) of $\mathrm{P}_0(f^\dagger)$ satisfies

1. *$u_t = u^\dagger_t$ for all $t \in \Sigma$, and*

2. *$\gamma_\theta = \gamma^\dagger_\theta$ for $\mathcal{H}_\Theta$-almost all $\theta \in \Theta$.*

Proof. We know by theorem 36 that

$$u_t = u^\dagger_t \text{ for all } t \in \mathcal{T}',$$

from which it follows via

$$\mathrm{Mv}_t \gamma_\theta = \mathrm{Rd}_\theta u_t = \mathrm{Rd}_\theta u^\dagger_t = \mathrm{Mv}_t \gamma^\dagger_\theta \text{ for all } \theta \in \Theta, t \in \mathcal{T}'$$

and proposition 37 that

$$\mathrm{Rd}_{\frac{(1,t)}{\sqrt{1+t^2}}} \gamma_\theta = \mathrm{Rd}_{\frac{(1,t)}{\sqrt{1+t^2}}} \gamma^\dagger_\theta \text{ for all } t \in \mathcal{T}'. \tag{3.10}$$

Then we have for the two-dimensional projections γ_θ by corollary 38 with $d = 2$ that the three Radon transforms (3.10) almost surely uniquely determine $u_t = u^\dagger_t$ for all $t \in \Sigma$. $\square$

3.2. Reconstruction properties in a noisy setting

In this section, we will derive error estimates for the model in the noisy setting, i.e., measurements f^δ with noise level δ. In order to do so, we must take into account two possible causes of error: mass change, i.e., particles being reconstructed with more or less mass to them than in the ground truth, and mass relocation, i.e., a reconstructed particle in a location where there are none in the ground truth configuration and vice versa. Note that these two sources of error cannot be clearly distinguished from one another and both are captured by the unbalanced Wasserstein-divergence, which we will use for quantification of the reconstruction error.

Definition 44 (Unbalanced Wasserstein-divergence ([3], Def 55))**.** *The Wasserstein-p distance between two non-negative Radon measures $\nu_1, \nu_2 \in \mathcal{M}_+(\mathbb{R}^d)$ for $p \geq 1$ is defined as*

$$W_p(\nu_1, \nu_2) = \inf \left\{ \left(\iint_{\mathbb{R}^d \times \mathbb{R}^d} \mathrm{dist}(x, y)^p \, \mathrm{d}\pi(x, y) \right)^{\frac{1}{p}} \mid \pi \in \mathcal{M}_+(\mathbb{R}^d \times \mathbb{R}^d), \right.$$

$$\left. [(x, y) \mapsto x]_\# \pi = \nu_1, [(x, y) \mapsto y]_\# \pi = \nu_2 \right\}.$$

For measures with unequal mass $\nu_1(\mathbb{R}^d) \neq \nu_2(\mathbb{R}^d)$, the above infimum is over the empty set and thus infinite. For a fixed $R > 0$, we define the unbalanced Wasserstein-p divergence between ν_1 and ν_2 as

$$W^p_{p,R}(\nu_1, \nu_2) = \inf \left\{ W^p_p(\nu, \nu_2) + \frac{1}{2} R^p \|\nu_1 - \nu\|_{\mathcal{M}} \mid \nu \in \mathcal{M}_+(\mathbb{R}^d) \right\}.$$

We will derive noise-dependent error estimates by constructing appropriate dual variables. This is a commonly used approach in inverse problems, an in-depth explanation of which can be found in [4]. In section 3.2.1, we will specifically construct dual variables for the product-topology formulation

$$\min_{\substack{\gamma \in \mathcal{M}_+(\Gamma)^\Theta \\ u \in \mathcal{M}_+(\Omega)^\Sigma}} \|\gamma_{\hat{\theta}}\|_{\mathcal{M}} + \frac{1}{2\alpha} \sum_{t \in \mathcal{T}} \|\mathrm{Ob}_t u_t - f_t\|_H^2 \text{ s.t. } \mathrm{Mv}_t^1 \gamma_\theta = \mathrm{Rd}_\theta u_t \text{ for all } t \in \Sigma, \theta \in \Theta$$

$$(\Pi\text{-}P_{\sqrt{\delta}}(f^\delta))$$

for $\hat{\theta} \in \Theta$ arbitrary but fixed, as this is more easily done than for $\mathrm{P}_\alpha(f)$, but the convergence rate results as stated in section 3.2.2 extend to both formulations. We first define in abstract terms:

- dual spaces X, Y to topological vector spaces,

- $K : X \to Y$ a continuous linear forward operator that is the dual to $K^* : Y^* \to X^*$,

- $G : X \to \mathbb{R}$ a convex regularisation term,

- $F_f : Y \to \mathbb{R}$ a non-negative convex fidelity term for measurement f, with $(F_f)^*$ the pre-dual Legendre-Fenchel conjugate, and

- $y^\dagger \in X$ a ground truth configuration.

Ground truths and noisy variables are denoted by $\dagger$ and δ respectively, where δ is the noise level in a measurement f^δ and we have $F_{f^\delta}(f^\dagger) \leq \delta$. The further derivation of error estimates is based upon the following result:

Theorem 45 (Unbalanced Wasserstein estimate for noisy reconstruction of non-negative measures on compact domains (adapted from [3], Cor 63 & Rem 64)). *Let $\Omega \subset \mathbb{R}^d$ be a compact domain. Consider the regulariser*

$$G(y^\delta) = G(y_1^\delta, y_2^\delta) = \|y_1^\delta\|_+ + G_2(y_2^\delta),$$

where

$$\|y_1^\delta\|_+ = \begin{cases} \|y_1^\delta\|_{\mathcal{M}} & \text{if } y_1^\delta \in \mathcal{M}_+(\Omega) \\ \infty & \text{else.} \end{cases}$$

Let $y_1^\dagger \in \mathcal{M}_+(\Omega)$ with $\mathrm{supp}\, y_1^\dagger = \{x_1, ..., x_N\} \subset \Omega$, and let y^δ with $y_1^\delta \in \mathcal{M}_+(\Omega)$ be obtained from the problem

$$\min_{y^\delta \in X} G(y^\delta) + \frac{1}{\alpha} F_{f^\delta}(Ky^\delta).$$

Let $w^\dagger, w \in Y^*$ such that, for some $\mu, \kappa, R > 0$ with $2R < \min_{i \neq j} \mathrm{dist}(x_i, x_j)$, all of the following conditions hold:

(i) $-K^* w^\dagger = -\left((K^* w^\dagger)_1, (K^* w^\dagger)_2\right) \in \partial G(y_2^\delta),$

(ii) $-(K^* w)_1 \in \partial \|\cdot\|_{\mathcal{M}} \left(\sum_{i=1}^N (y_1^\delta - y_1^\dagger)(B_R(\{x_i\})\delta_{x_i}\right),$

(iii) $-(K^* w^\dagger)_1(x) \leq 1 - \kappa \min\{R, \mathrm{dist}(x, \mathrm{supp}\, y_1^\dagger)\}^2,$

(iv) $(K^* w)_1(x_i)(K^* w)_1(x) \geq 1 - \mu \, \mathrm{dist}(x, x_i)^2 \text{ for all } x \in B_R(\{x_i\}), i = 1, ..., N.$

Then we have

$$W_{2,R}^2(y_1^\delta, y_1^\dagger) \le \frac{1}{2} R^2 \langle (K^* w)_2, y_2^\delta - y_2^\dagger \rangle$$
$$+ \frac{12 + 7 \max\{\kappa, \mu\} R^2}{4\kappa\alpha} \left(\delta + F_{f^\delta}^*(2\alpha w^\dagger) + F_{f^\delta}^*(-2\alpha w^\dagger) + F_{f^\delta}^*(2\alpha w) + F_{f^\delta}^*(-2\alpha w) \right).$$
$$(3.11)$$

A proof of theorem 45 is beyond the scope of this thesis but can be found in [3].

3.2.1. Construction of dual variables for $\Pi\text{-}P_{\sqrt{\delta}}(f^\delta)$

We now construct specific dual variables for $\Pi\text{-}P_{\sqrt{\delta}}(f^\delta)$ by following a similar three-step strategy as for the noise-free setting in section 3.1 before:

1. Show reconstruction properties for a few snapshots u_t which possess a handy property. Here, these are snapshots that are stably reconstructible by definition 46 (theorem 48).

2. On the basis of the first step, derive error estimates for the position-velocity projections γ (theorem 55).

3. Infer error estimates for all non-stably-reconstructible snapshots from the information attained in the first two steps (theorem 56).

First, consider stably-reconstructible measures.

Definition 46 (Stably reconstructible measure ([3], Def 5))**.** *We call a measure $\nu^\dagger = \sum_{i=1}^N m_i \delta_{x_i} \in \mathcal{M}_+(\Omega)$ stably reconstructible from measurements via K, if there exist $\kappa, \mu, R > 0$ such that for any N-tuple $s \in \{-1, 1\}^N$ and associated measure $\nu^s = \sum_{i=1}^N s_i \delta_{x_i} \in \mathcal{M}(\Omega)$, there exist dual variables $v^\dagger, v^s$, such that all following properties are fulfilled:*

(i) $-K^* v^\dagger \in \partial \| \cdot \|_{\mathcal{M}}(\nu^\dagger)$,

(ii) $-K^* v^s \in \partial \| \cdot \|_{\mathcal{M}}(\nu^s)$,

(iii) $-K^* v^\dagger(x) \le 1 - \kappa \min\{R, \text{dist}(x, \text{supp}\,\nu^\dagger)\}^2$ *for all $x \in \Omega$,*

(iv) $K^* v^s(x_i) K^* v^s(x) \ge 1 - \mu \,\text{dist}(x, x_i)^2$ *for all $x \in B_R(\{x_i\}), i = 1, ..., N$.*

For particular choices of forward operator K, straightforward criteria have been proven to be sufficient for stable reconstructibility of a measure. Relevant to our application, one such operator is the truncated Fourier series, for which Candès and Fernandez-Granda have identified the minimum distance between particles in a configuration as a sufficient condition in [8].

Remark 47 (Stable reconstructibility for truncated Fourier series ([8], Lem 2.4 & 2.5))**.** *Let the observation operator $K = \mathcal{F}_\Phi$ be the truncated Fourier series on S^1 with cutoff frequency $\Phi > 0$. Then there exist constants $c_0, c_1, c_2, c_3 > 0$ such that a measure $u^\dagger = \sum_{i=1}^N m_i \delta_{x_i} \in \mathcal{M}_+(S^1)$ with a minimum distance of $\Delta = \frac{c_0}{\Phi}$ between any two Dirac locations is $(c_1\Phi^2, c_2\Phi^2, \frac{c_3}{\Phi}) - $ stably reconstructible.*

Versions of this statement in more than one dimension are given but not proven in [8]. We investigate to what extent this source condition might translate to the MRI setting for the mri-adapted observation operator as introduced in chapter 5, by examining the relationship between the performance of the method and varying levels of separation between particles in the numerical experiments in chapter 6. The statement of a source condition for the mri-adapted method is outside the scope of this thesis but may be a point of interest for future exploration. For a stably reconstructible measure, we can consider a version of the error estimate (3.11) as a special case of theorem 45 as follows.

Theorem 48 (Unbalanced Wasserstein distance for a stably reconstructible measure ([3], Thm 66)). *Let measure $\nu^\dagger$ be (κ, μ, R)-stably reconstructible from measurements via K with dual variables $v^\dagger, v^s$. Let $f^\dagger = K\nu^\dagger$ and noisy measurement f^δ such that $F_{f^\delta}(f^\dagger) \leq \delta$. Then for ν^δ the minimiser of*

$$\min_{\nu^\delta} \|\nu^\delta\|_+ + \frac{1}{\alpha} F_{f^\delta}(K\nu^\delta),$$

we have

$$W_{2,R}^2(\nu^\delta, \nu^\dagger) \leq \frac{12 + 7\max\{\kappa, \mu\}R^2}{4\kappa\alpha}$$
$$\cdot \left(\delta + F_{f^\delta}^*(2\alpha v^\dagger) + F_{f^\delta}^*(-2\alpha v^\dagger) + \max_{s \in \{-1,1\}^N} F_{f^\delta}^*(2\alpha v^s) + F_{f^\delta}^*(-2\alpha v^s) \right).$$

In preparation for the construction of dual variables for the product topology-setting, we introduce some concise notation.

Definition 49 (Abbreviated operators (as used in [3])). *Define*

$$\underline{\mathrm{Rd}} : \mathcal{M}(\Omega)^\Sigma \to \mathcal{M}(\Xi)^{\Theta \times \Sigma}, \qquad \underline{\mathrm{Rd}}(u) = (\mathrm{Rd}_\theta u_t)_{\theta \in \Theta, t \in \Sigma},$$
$$\underline{\mathrm{Mv}}^1 : \mathcal{M}(\Gamma)^\Theta \to \mathcal{M}(\Xi)^{\Theta \times \Sigma}, \qquad \underline{\mathrm{Mv}}^1(\gamma) = (\mathrm{Mv}_t^1 \gamma_\theta)_{\theta \in \Theta, t \in \Sigma},$$
$$\underline{\mathrm{Ob}} : \mathcal{M}(\Gamma)^\Sigma \to H^{|\mathcal{T}|}, \qquad \underline{\mathrm{Ob}}(u) = (\mathrm{Ob}_t u_t)_{t \in \mathcal{T}},$$

and

$$\iota_+ : \prod_{i \in I} \mathcal{M}(A_i) \to \{0, \infty\}, \qquad \iota_+(\nu) = \begin{cases} 0 & \text{if } \nu_i \in \mathcal{M}_+(A_i) \text{ for all } i \in I, \\ \infty & \text{else,} \end{cases}$$

where I is an index set for Lipschitz domains A_i.

Proposition 50. *Note that*

$$w \in \partial\| \cdot \|_+(\nu) \iff w \leq 1 \text{ everywhere with } w = 1 \text{ on } \mathrm{supp}\,\nu, \qquad (3.12)$$
$$w \in \partial\iota_+(\nu) \iff w \leq 0 \text{ everywhere with } w = 0 \text{ on } \mathrm{supp}\,\nu. \qquad (3.13)$$

Remark 51. *The abbreviated operators from definition 49 are continuous with respect to the product topology.*

Proof. An operator K ist continuous w.r.t. the product topology if $p_j \circ K$ is continuous for all projections

$$p_j : \prod_{i \in J} Y_j \to Y_j.$$

Consider $\underline{\mathrm{Rd}}$, then

$$
\begin{aligned}
p_{\theta,t} \circ \underline{\mathrm{Rd}} u &= \mathrm{Rd}_\theta u_t \\
&= \mathrm{Rd}_\theta(\mathrm{pr}_t(u)) \quad \text{for all } \theta \in \Theta,
\end{aligned}
$$

where $\mathrm{pr}_t : \mathcal{M}(\Omega)^\Sigma \to \mathcal{M}(\Omega)$ is a continuous projection for all $t \in \Sigma$ and Rd_θ is a continuous linear operator between Banach spaces. Thus, their composition is continuous. Analogous arguments hold for the other operators. $\qquad\square$

We now define appropriate choices of regularisation energy, fidelity term and (pre-)dual spaces and variables for reconstruction error estimation for the model $\Pi\text{-}P_{\sqrt{\delta}}(f^\delta)$. To this end, let

- $X = \mathcal{M}(\Omega)^\Sigma \times \mathcal{M}(\Gamma)^\Theta$,
- $Y = H^{|\mathcal{T}|} \times \mathcal{M}(\Xi)^{\Theta \times \Gamma}$,
- $y^\dagger = (u^\dagger, \gamma^\dagger)$, $y^\delta = (u, \gamma) \in X$,
- $K = \begin{pmatrix} \underline{\mathrm{Ob}} & 0 \\ \underline{\mathrm{Rd}} & -\underline{\mathrm{Mv}}^1 \end{pmatrix} : X \to Y$,
- $F_f(a,b) = \frac{1}{2} \sum_{t \in \mathcal{T}} \|a_t - f_t\|_H^2 + \iota_0(b)$,
- $G(u, \gamma) = \iota_+(u, \gamma) + *$,

where $*$ is chosen as either $\|\gamma_\theta\|_{\mathcal{M}}$ or $\|u_t\|_{\mathcal{M}}$ for particular θ and t as is convenient for the respective argument. Since $\underline{\mathrm{Rd}} u = \underline{\mathrm{Mv}}^1 \gamma$ has to hold for any solution (u, γ) and since both Radon and move operators map non-negative measures to non-negative measures of the same norm by remark 22, these choices are equivalent. Then we have pre-dual spaces

$$X^* = \left\{ (\phi, \psi) \in C(\Omega)^\Sigma \times C(\Gamma)^\Theta \mid \phi_t = \psi_\theta = 0 \text{ for almost all } t \in \Sigma, \theta \in \Theta \right\}$$

and

$$Y^* = \left\{ (v, q) \in (H^*)^{|\mathcal{T}|} \times C(\Xi)^{\Theta \times \Sigma} \mid q_{\theta,t} = 0 \text{ for almost all } t \in \Sigma, \theta \in \Theta \right\},$$

equipped with the final topology with respect to inclusions

$$
\begin{aligned}
\phi_t &\mapsto (\phi, \psi) \in X^* & &\text{with } \phi_{\tilde{t}} = 0 \text{ for all } \tilde{t} \neq t \\
\psi_\theta &\mapsto (\phi, \psi) \in X^* & &\text{with } \psi_{\tilde{\theta}} = 0 \text{ for all } \tilde{\theta} \neq \theta \\
q_{\theta,t} &\mapsto (v, q) \in Y^* & &\text{with } q_{\tilde{\theta},\tilde{t}} = 0 \text{ for all } (\tilde{\theta}, \tilde{t}) \neq (\theta, t).
\end{aligned}
$$

Remark 52. *For F_f^* as chosen above and $w = (w_1, w_2) \in Y^*$, we have*

$$F_f^*(w_1, w_2) = \sum_{t \in \mathcal{T}} \frac{1}{2} \|(w_1)_t\|_{H^*}^2 + \langle (w_1)_t, f_t \rangle.$$

and thus

$$F_f^*(2\alpha w) + F_f^*(-2\alpha w) = \sum_{t \in \mathcal{T}} \|(2\alpha w_1)_t\|_{H^*}^2$$
$$= 4\alpha^2 |w_1|^2$$

for $|\cdot| : (H^*)^{|\mathcal{T}|} \to \mathbb{R}_{\geq 0}$ *defined accordingly.*

Note. *The notation $|w|$ for a dual variable w as defined here is not to be confused with the cardinality $|\mathcal{T}|$ of a set $\mathcal{T}$. Since it is always immediately clear from context whether a dual variable or a set is considered, this notation will hereinafter pertain to both.*

With these definitions in place, we demonstrate that the error estimate from theorem 48 can be transferred to stably reconstructible snapshots in the dynamic setting.

Theorem 53 (Error estimate for stably reconstructible snapshots ([3], Thm 68)). *Let a snapshot $u_t^\dagger$ be (κ, μ, R)-stably reconstrubtible from measurements with Ob_t via $v^\dagger, v^s$. Then for (u, γ) the minimiser of $\Pi\text{-}P_{\sqrt{\delta}}(f^\delta)$, we have*

$$W_{2,R}^2(u_t, u_t^\dagger) \leq \frac{12 + 7\max\{\kappa, \mu\}R^2}{4\kappa} \left(1 + 4|v^\dagger|^2 + \max_{s \in \{-1,1\}^N} 4|v^s|^2\right) \sqrt{\delta}. \tag{3.14}$$

Proof. Let $s_i = \left(\mathrm{sgn}\left((u_t - u_t^\dagger)(B_R(\{x_i + tv_i\}))\right)\right)_{i=1,\dots,N}$ and let $v^\dagger, v^s$ be the dual variables for $u_t^\dagger$ as set in definition 46. Furthermore, let $y^\delta = (u, \gamma)$ with $y_1^\delta = u_t$ and $y_2^\delta = \left((u_{\tilde{t}})_{\tilde{t} \neq t}, \gamma\right)$, define $y^\dagger$ analogously and consider the regulariser

$$G(y^\delta) = \|y_1^\delta\|_+ + \iota_+(y_2^\delta).$$

Then the dual variables

$$w^\dagger = \begin{pmatrix} \tilde{v}^\dagger \\ 0 \end{pmatrix} \quad \text{with } \tilde{v}_{\tilde{t}}^\dagger = \begin{cases} v^\dagger & \text{if } \tilde{t} = t \\ 0 & \text{else} \end{cases}$$

and

$$w = \begin{pmatrix} \tilde{v} \\ 0 \end{pmatrix} \quad \text{with } \tilde{v}_{\tilde{t}} = \begin{cases} v^s & \text{if } \tilde{t} = t \\ 0 & \text{else} \end{cases}$$

satisfy the conditions of theorem 45. Indeed, we have that

$$-\mathrm{Ob}_t^* \tilde{v}_t^\dagger = -\mathrm{Ob}_t^* v^\dagger$$
$$\leq 1 - \kappa \min\{R, \mathrm{dist}(x, \mathrm{supp}\, u_t^\dagger)\}^2 \leq 1 \tag{3.15}$$

with equality on the support of $y_1^\dagger = u_t^\dagger$ and by (3.12) this gives that $-(K^* w^\dagger)_1 \in \partial \|\cdot\|_+(y_1^\dagger)$. Additionally, $(K^* w^\dagger)_2 = 0$ everywhere and with (3.13), we have $-(K^* w^\dagger)_2 \in \partial \iota_+(y_2^\dagger)$. Thus, the conditions are fulfilled for $w^\dagger$. The conditions for w follow easily by the definitions of $v^\dagger$ and v^s. $\square$

We now proceed to the second step and construct corresponding dual variables for the position-velocity projections. The error estimates resulting from this are dependent upon the margins by which a particle configuration 'misses' admitting a coincidence or ghost particle.

Definition 54 (Δ-coincidence and Δ-ghost particle with respect to configurations and projections ([3], Def 69 & 72)). *Let $\nu = \sum_{i=1}^{N} m_i \delta_{(x_i, v_i)} \in \mathcal{M}_+(\mathbb{R}^n \times \mathbb{R}^n)$ be a particle configuration and $\mathcal{T}' \subset \mathbb{R}$ a set of times. Configuration ν admits...*

(i) a Δ-coincidence with respect to $\mathcal{T}'$ if there exist two particles i, j with $i \neq j$ and a time $t \in \mathcal{T}'$, such that $\mathrm{dist}(x_i + t v_i, x_j + t v_j) \leq \Delta$.

(ii) a Δ-ghost particle with respect to $\mathcal{T}'$ at $(x, v) \in \mathbb{R}^n \times \mathbb{R}^n$ if, for every $t \in \mathcal{T}'$, there exists some particle i such that $\mathrm{dist}(x + tv, x_i + t v_i) \leq \Delta$.

Analogously, for $\Theta' \subset S^{d-1}$ a set of directions, a static particle configuration $u = \sum_{i=1}^{N} m_i \delta_{x_i} \in \mathcal{M}_+(\mathbb{R}^d)$ admits...

(i) a Δ-coincidence with respect to Θ' if there exist two particles i, j with $i \neq j$ and a direction $\theta \in \Theta'$, such that $\mathrm{dist}(\theta \cdot x_i, \theta \cdot x_j) \leq \Delta$.

(ii) a Δ-ghost particle with respect to Θ' at $x \in \mathbb{R}^d$ if, for every $\theta \in \Theta'$, there exists some particle i such that $\mathrm{dist}(\theta \cdot x, \theta \cdot x_i) \leq \Delta$.

Theorem 55 (Error estimates for γ ([3], Thm 70)). *Let $\theta \in \Theta$ and let $\mathcal{T}' \subset \mathcal{T}$ be a subset of times for which $u_t^\dagger$ is $(\hat{\kappa}, \hat{\mu}, \hat{R})$-stably reconstructible from measurements with Ob_t via $\hat{v}_t^\dagger, \hat{v}_t^s$. Let σ be the smallest eigenvalue of $\frac{1}{|\mathcal{T}'|} \sum_{t \in \mathcal{T}'} \begin{pmatrix} 1 \\ -t \end{pmatrix} \otimes \begin{pmatrix} 1 \\ -t \end{pmatrix}$, let $\kappa = \sigma \hat{\kappa}$ and define*

$$R = \frac{\min\{\hat{R}, \frac{\Delta}{3}, \Delta'\}}{\sqrt{1 + \max_{t \in \mathcal{T}'} t^2}},$$

where $\Delta, \Delta' \geq 0$ are such that $\gamma_\theta^\dagger$ admits no Δ-coincidences or Δ'-ghost particles with respect to $\mathcal{T}'$. Then for (u, γ) the minimiser of Π-$P_{\sqrt{\delta}}(f^\delta)$, the unbalanced Wasserstein distance w.r.t. the position-velocity projections is bound via

$$W_{2,R}^2(\gamma_\theta, \gamma_\theta^\dagger) \leq \frac{12 + 7\kappa R^2}{4\kappa} \left(1 + 4 \max_{t \in \mathcal{T}'} |\hat{v}_t^\dagger|^2 \right) \sqrt{\delta} + \frac{1}{2R^2} \max_{t \in \mathcal{T}'} W_{2,R}^2(u_t, u_t^\dagger). \qquad (3.16)$$

Proof. Let $y^\delta = (u, \gamma)$ and split it into $y_1^\delta = \gamma_\theta$ and $y_2^\delta = (u, (\gamma_{\tilde{\theta}})_{\tilde{\theta} \neq \theta})$. Consider the regulariser

$$G(u, \gamma) = \|\gamma_\theta\|_+ + \iota_+(u, (\gamma_{\tilde{\theta}})_{\tilde{\theta} \neq \theta}).$$

Our goal is to construct dual variables $w^\dagger$ and w that fulfill the conditions of theorem 45. Define

- $v^\dagger \in (H^*)^{|\mathcal{T}|}$ with $v_t^\dagger = \begin{cases} \frac{\hat{v}_t^\dagger}{|\mathcal{T}'|} & \text{if } t \in \mathcal{T}', \\ 0 & \text{else,} \end{cases}$

- $\bar{R} = \min\{\hat{R}, \frac{\Delta}{3}, \Delta'\}$,

- $s_i = \mathrm{sgn}(\gamma_\theta - \gamma_{\tilde{\theta}}) \left(B_R(\{(\theta \cdot x_i, \theta \cdot v_i)\}) \right)$ for $i = 1, \ldots, N$.

Then let $q^\dagger \in C(\Xi)^{\Theta \times \Gamma}$ be

$$q^\dagger_{\tilde{\theta},t} = \begin{cases} \frac{1 - \tilde{\kappa} \min\{\bar{R}, \text{dist}(x, \text{supp } \text{Rd}_\theta u^\dagger_t)\}^2}{|\mathcal{T}'|} & \text{if } t \in \mathcal{T}', \tilde{\theta} = \theta, \\ 0 & \text{else }, \end{cases}$$

(3.17)

and let $q \in C(\Xi)^{\Theta \times \Gamma}$ be the continuous extension of

$$q_{\tilde{\theta},t}(x) = \begin{cases} \frac{s_i}{|\mathcal{T}'|} & \text{if } t \in \mathcal{T}', \tilde{\theta} = \theta, \text{ and } x \in B_{\bar{R}}(\{\theta \cdot (x_i + tv_i)\}), \\ 0 & \text{else }, \end{cases}$$ (3.18)

onto the entirety of Ξ such that $|q| \leq \frac{1}{|\mathcal{T}'|}$ holds everywhere. The latter is possible since, by choice of $\bar{R} \leq \frac{\Delta}{3}$, the intersections $B_{\bar{R}}(\{\theta \cdot (x_i + tv_i)\}) \cap B_{\bar{R}}(\{\theta \cdot (x_j + tv_j)\})$ are empty for $i \neq j$. Lastly, we define

$$w^\dagger = \begin{pmatrix} v^\dagger \\ q^\dagger \end{pmatrix} \text{ and } w = \begin{pmatrix} 0 \\ q \end{pmatrix}.$$

We now demonstrate that these choices indeed satisfy the conditions of theorem 45 for $\mu = 0$. Firstly, by $\bar{R} \leq \hat{R}$ and stable reconstrubtibility of $u^\dagger_t$ via $\hat{v}^\dagger_t, \hat{v}^s_t$, we have for all $t \in \mathcal{T}'$ that

$$\text{Ob}^*_t v^\dagger_t(x) = \left(\text{Ob}^*_t \frac{\hat{v}^\dagger_t}{|\mathcal{T}'|} \right)(x)$$

$$\geq \frac{\hat{\kappa}}{|\mathcal{T}'|} \min\{\hat{R}, \text{dist}(x, \text{supp } u^\dagger_t)\}^2 - 1$$

$$\geq \frac{\hat{\kappa}}{|\mathcal{T}'|} \min\{\bar{R}, \text{dist}(x, \text{supp } u^\dagger_t)\}^2 - 1 = -\text{Rd}^*_\theta q^\dagger_{\theta,t}(x)$$

and thus

$$\underline{\text{Ob}}^* v^\dagger + \underline{\text{Rd}}^* q^\dagger \geq 0$$

with equality on the support of $u^\dagger_t$ and, by (3.13), we have

$$- \left(\underline{\text{Ob}}^* v^\dagger + \underline{\text{Rd}}^* q^\dagger \right) \in \partial \iota_+(u^\dagger_t).$$ (3.19)

Secondly, we define neighbourhoods

$$\mathcal{N}_i = \bigcup_{t \in \mathcal{T}'} \left\{ \begin{pmatrix} x \\ v \end{pmatrix} \in \mathbb{R}^2 \mid -\bar{R} \leq \begin{pmatrix} 1 \\ t \end{pmatrix} \cdot \left[\begin{pmatrix} x \\ v \end{pmatrix} - \begin{pmatrix} \theta \cdot x_i \\ \theta \cdot v_i \end{pmatrix} \right] \leq \bar{R} \right\}$$ (3.20)

of $(\theta \cdot x_i, \theta \cdot v_i)$. Then for $(x, v) \in \mathcal{N}_i$, we have

$$\left((\underline{\text{Mv}}^1)^* q^\dagger \right)_\theta (x, v) = \sum_{t \in \mathcal{T}'} \text{Mv}^1_t q^\dagger_{\theta,t}(x, v)$$

$$= 1 - \hat{\kappa}(x - \theta \cdot x_i, v - \theta \cdot v_i) \cdot Q \cdot \begin{pmatrix} x - \theta \cdot x_i \\ v - \theta \cdot v_i \end{pmatrix}$$

where Q is the positive definite matrix

$$Q = \frac{1}{|\mathcal{T}'|} \sum_{t \in \mathcal{T}'} \begin{pmatrix} 1 \\ -t \end{pmatrix} \otimes \begin{pmatrix} 1 \\ -t \end{pmatrix}.$$

Thus, since $\kappa = \sigma \hat{\kappa}$ and σ is by definition the smallest eigenvalue of Q, we get

$$\left((\underline{Mv}^1)^* q^\dagger \right)_\theta (x, v) \leq 1 - \kappa \operatorname{dist}((x, v), \operatorname{supp} \gamma_\theta^\dagger)^2$$

for $(x, v) \in \bigcup_{i=1,\dots,N} \mathcal{N}_i$ with equality on the support of $\gamma_\theta^\dagger$ and, by (3.12),

$$\left((\underline{Mv}^1)^* q^\dagger \right)_\theta \in \partial \| \cdot \|_+(\gamma_\theta^\dagger). \tag{3.21}$$

Thirdly, note that $\left((\underline{Mv}^1)^* q^\dagger \right)_\theta \leq 1 - \hat{\kappa} \bar{R}^2$ for all $(x, v) \notin \mathcal{N}_i$, since $\bar{R} \leq \Delta'$ and γ_θ^t admits no Δ'-ghost particles. For R as defined in the statement, we have $R = \frac{\bar{R}}{\sqrt{1 + \max_{t \in \mathcal{T}'} t^2}}$. Then $B_R(\{(\theta \cdot x_i, \theta \cdot v_i)\}) \subset \mathcal{N}_i$ and thus we have

$$\left((\underline{Mv}^1)^* q^\dagger \right)_\theta (x, v) \leq 1 - \kappa \min\{R, \operatorname{dist}((x, v)), \operatorname{supp} \gamma_\theta^\dagger)\}^2. \tag{3.22}$$

Thus the conditions of theorem 45 for $w^\dagger$ are fulfilled. We can show analogously that

$$\left((\underline{Mv}^1)^* q \right)_\theta \in \partial \| \cdot \|_{\mathcal{M}} \left(\sum_{(x,v) \in \operatorname{supp} \gamma_\theta^\dagger} (\gamma_\theta - \gamma_\theta^\dagger)(B_R(\{(x, v)\})) \delta_{(x,v)} \right)$$

and

$$\left((\underline{Mv}^1)^* q \right)_\theta (x, v) \cdot \left((\underline{Mv}^1)^* q \right)_\theta (x_i, v_i) = s_i^2 = 1 \text{ for all } (x, v) \in B_R(\{(\theta \cdot x_i, \theta \cdot v_i)\}),$$

and thus the conditions for $w = \begin{pmatrix} 0 \\ q \end{pmatrix}$ are satisfied as well (with $\mu = 0$). Now lastly, with

$$|(\underline{Rd}^* q)_t(x)| = \left| \frac{s_i}{|\mathcal{T}'|} \right| = \frac{1}{|\mathcal{T}'|} \text{ for all } x \in B_{\bar{R}}(\operatorname{supp} u_t^\dagger), t \in \mathcal{T}',$$

we arrive at

$$\begin{aligned}
\langle (K^* w)_2, y_2^\delta - y_2^\dagger \rangle &= \sum_{t \in \mathcal{T}'} \langle (\underline{Rd}^* q)_t, u_t - u_t^\dagger \rangle \\
&\leq \frac{1}{|\mathcal{T}'|} \sum_{t \in \mathcal{T}'} \left(|(u_t - u_t^\dagger)(\Omega \setminus B_R(\operatorname{supp} u_t^\dagger))| + |(u_t - u_t^\dagger)(B_R(\operatorname{supp} u_t^\dagger))| \right) \\
&\leq \frac{1}{2R^2 |\mathcal{T}'|} \sum_{t \in \mathcal{T}'} W_{2,R}^2(u_t, u_t^\dagger)
\end{aligned}$$

and the claim follows with theorem 45. $\qquad \square$

To conclude, we undertake the third and last step and derive reconstruction properties for the non-stably-reconstructible snapshots as well.

Theorem 56 (Error estimate for non-stably-reconstructible snapshots ([3], Thm 73)). *Let $\Theta' \subset \Theta$ a finite subset of directions and $\mathcal{T}' \subset \mathcal{T}$ such that $u_t^\dagger$ is $(\hat{\kappa}, \hat{\mu}, \hat{R})$-stably reconstructible from measurements with Ob_t via $\hat{v}_t^\dagger, \hat{v}_t^s$ for all times $t \in \mathcal{T}'$. Let σ be the smallest eigenvalue of $\frac{1}{|\Theta'|} \sum_{\theta \in \Theta'} \theta \otimes \theta$, let $\bar{\kappa} = \frac{\sigma \kappa}{1+t^2}$ and define*

$$\bar{R} = \min\left\{(1+t^2)R, \frac{\Delta}{3\sqrt{1+t^2}}, \Delta'\right\},$$

where $\Delta, \Delta' \geq 0$ are such that $u_t^\dagger$ admits no Δ-coincidences or Δ'-ghost particles with respect to Θ', and κ and R are as in theorem 55, taking the minimum R over all $\theta \in \Theta'$. Then for (u, γ) the minimiser of $\Pi\text{-}P_{\sqrt{\delta}}(f^\delta)$, the error estimate for $t \in \Sigma \setminus \mathcal{T}'$ is bound via

$$W_{2,\bar{R}}^2(u_t, u_t^\dagger) \leq \frac{12 + 7\bar{\kappa}\bar{R}^2}{4\bar{\kappa}}\left(1 + 4\max_{t \in \mathcal{T}'}|\hat{v}_t^\dagger|^2\right)\sqrt{\delta} + \frac{1}{2\bar{R}^2}\max_{\theta \in \Theta'}W_{2,\bar{R}}^2(\gamma_\theta, \gamma_\theta^\dagger). \tag{3.23}$$

A proof of theorem 56 can be found in [3]. It is left out here for brevity but largely follows similar arguments to those seen in the proof of theorem 55 as the dual variables are constructed analogously except for u and $\mathcal{T}'$ being swapped with γ and Θ' respectively.

3.2.2. Error estimates in the noisy setting

Similar results regarding the reconstruction error hold for the formulation $P_\alpha(f)$. In fact, theorem 48 holds exactly as is for $\mathcal{M}_+(\Gamma)^\Theta$ instead of $\mathcal{M}_+(\Theta \times \Gamma)$ as well, whereas theorems 55 and 56 need slight alterations. These estimates are explored in detail in [3], but left out here for brevity. The reconstruction properties in the noisy setting can now be summarised as follows.

Theorem 57 (Reconstruction error estimates in the noisy setting ([3], Thm 65)). *Let (u, γ) be the solution of $P_{\sqrt{\delta}}(f^\delta)$ or $\Pi\text{-}P_{\sqrt{\delta}}(f^\delta)$. Let $\mathcal{T}' \subset \mathcal{T}$ be a non-empty set of times t for which $u_t^\dagger$ is stably reconstructible and let $\Theta' \subset \Theta$ be a subset of directions. Then there exist constants $R, C_1 > 0$, depending on $\lambda^\dagger$ and $\mathcal{T}'$, and $C_2 > 0$, depending on $\lambda^\dagger$ and Θ', such that*

1. $W_{2,R}^2(u_t, u_t^\dagger) \leq C_1\sqrt{\delta}$ *for all $t \in \mathcal{T}'$,*

2. $W_{2,R_\theta}^2(\gamma_\theta, \gamma_\theta^\dagger) \leq \frac{C_1}{R_\theta^\dagger}\sqrt{\delta}$ *for all $\theta \in \Theta$ in case of $\Pi\text{-}P_{\sqrt{\delta}}(f^\delta)$ (respectively for $\mathcal{H}_\Theta$-almost all $\theta \in \Theta$ in case of $P_\alpha(f)$), where*

$$R_\theta = \frac{\min\{R, \frac{\Delta_\theta}{3}\}}{\sqrt{1 + \max_{t \in \mathcal{T}'} t^2}}$$

   and $\Delta_\theta \geq 0$ is such that $\gamma_\theta^\dagger$ contains no Δ_θ-coincidences or Δ_θ-ghost particles with respect to $\mathcal{T}'$,

3. $W_{2,R_t}^2(u_t, u_t^\dagger) \leq C_1 C_2(t^2 + \frac{1}{R_t^4})\sqrt{\delta}$ *for all $t \in \Sigma$, where*

$$R_t = \frac{\min\{R, \frac{\Delta_t}{3}\}}{3\sqrt{1+t^2}}$$

and $\Delta_t \in [0, \inf_{\theta \in \Theta'} \Delta_\theta]$ *is such that* $u_t^\dagger$ *contains no* Δ_t*-coincidences or* Δ_t*-ghost particles with respect to* Θ'.

Proof. The result follows for $\Pi\text{-}P_{\sqrt{\delta}}(f^\delta)$ from theorems 48, 55 and 56. $\qquad\qquad\square$

The result of theorem 57 for $P_\alpha(f)$ follows with analogous construction of dual variables, see the corresponding theorems 74, 75, 76 and 77 in [3].

CHAPTER 4

Magnetic Resonance Imaging

In order to apply the dimension-reduced reconstruction method to data obtained from MRI scans, we must first understand how MRI works. It should be duly noted at this point that Magnetic Resonance Imaging is a complex technology and that the following explanation is by no means exhaustive, but intended to build a basic understanding of the process and its implications for the reconstruction method. This section is oriented mostly along [9] and [10], with additional input from [11] and [12].

4.1. Components of the scanner

We consider here scanners with a closed-bore cylindrical design, which make up the majority of MRI scanners world-wide [13]. Inside the body of the scanner, there are three types of coils. The first is the principal cylindrical superconducting magnet, which consists of
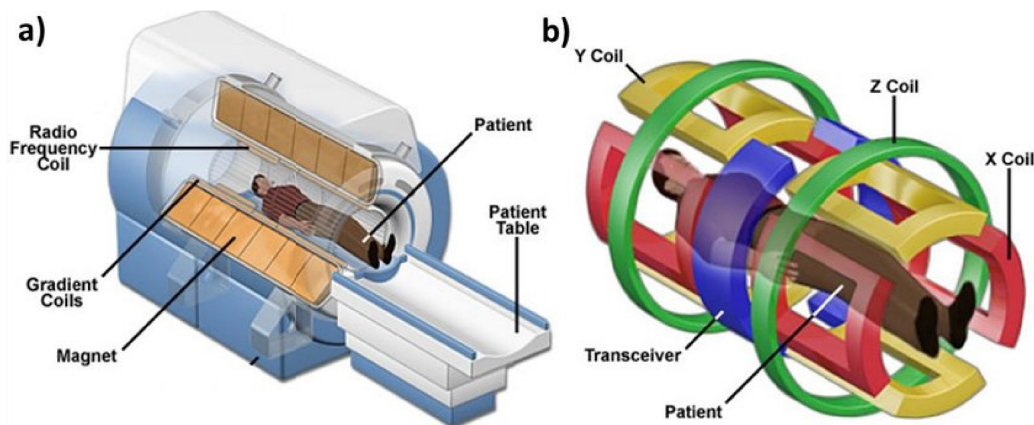
Figure 4.1.: The coils inside an MRI scanner. (from [14])

windings surrounding the imaging volume, enclosed in a vacuum tight vessel filled with liquid helium. Consider a three-dimensional coordinate system with axes x, y and z, with the z-axis pointing along the sample stage (or patient table in clinical scanners). Then this main magnet creates a static magnetic field $\vec{B}_0 = (0, 0, B_0)^\top$ with magnetic flux density B_0. As depicted in figure 4.2, $\vec{B}_0$ is not perfectly homogeneous, but the specific design of the main magnet, as well as additional shim coils, mitigate this issue such that an area towards the centre of the magnetic field is sufficiently homogeneous for use in MRI. Most scanners in clinical use have static fields ranging from 0.5 to 3 Tesla [15]. The particular scanner

used for gathering data for the experiments in section 6.3 generates a 9.4 T ultra-high field.
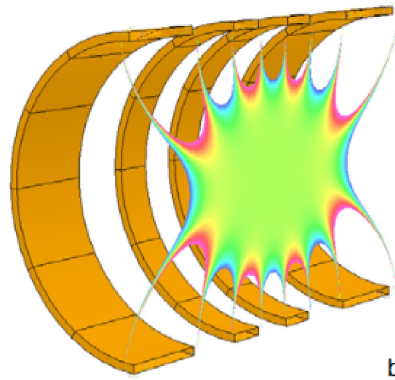
Figure 4.2.: The region of the static magnetic field $\vec{B}_0$ in which the field strength differs less than 1% from the field centre. (from [13])

Secondly, there are the X-, Y- and Z-gradient coils. They produce distortions in B_0 by adding time-varying secondary magnetic fields, the purpose of which is discussed in section 4.2.4.

Thirdly, the radiofrequency (RF) coils have two functions: to transmit radiofrequency pulses and to detect signals via electromagnetic induction (see section 4.2.2). Depending on scanner design, there can either be separate RF coils for transmission and reception or one single coil serving both functions.

4.2. Nuclear Magnetic Resonance

At the basis of MRI is the physical phenomenon of *Nuclear Magnetic Resonance (NMR)*, as first described for molecular beams by Isidor Rabi in 1938 [16], and for liquids and solids by Felix Bloch [11] and Edward Mills Purcell [17] respectively in 1946, winning all three of them Nobel Prizes in Physics [18]. It describes the capacity of many atomic nuclei, when placed in a magnetic field, to absorb and re-emit radiofrequency energy. Most MRI scanners make use of this property in hydrogen protons, specifically.

4.2.1. Spin and precession

Spin angular momentum, or simply *spin*, is a fundamental and intrinsic natural property of atomic and subatomic particles. We may think of spin angular momentum as a vector-like property, with directional components describing the way it is pointing. While not entirely quantum mechanically accurate[1], it is a helpful image to think of the spin vector as somewhat akin to the axis of rotation in classical physics. This vector can never be

---

[1]For more precise mathematical descriptions, consider the concept of spinors (see for example [19]). For a more detailed physical (and somewhat humourous) characterisation, see the 34th Feynman lecture [20].

measured directly, due to Heisenberg's uncertainty principle, but its existence can be shown experimentally for large collections of particles. This was first done in an experiment by Stern and Gerlach [21] in 1922, which demonstrated a quantised spatial orientation of spin angular momentum, meaning that upon measurement only a set of discrete *eigenstates* is ever observed. The nucleus of ^1H, the most common hydrogen isotope, possesses a spin of $S = \frac{1}{2}\hbar$, where $\hbar$ is the reduced Planck constant, and takes two ($= 2S/\hbar + 1$) spin eigenstates. Since the ^1H nucleus consists of a single proton, the terms nucleus and proton are henceforth used interchangeably.

Spin is closely related to magnetic properties: The intrinsic magnetic moment $\vec{mu}$ of a proton is proportional to its spin via $\vec{\mu} = \gamma S$, where γ is the *gyromagnetic ratio*, an empirical constant specific to the atomic species. The (rounded) gyromagnetic ratio of ^1H is $42.58\,\mathrm{MHz/T}$. In keeping with the imagery from classical physics, we may imagine a proton with spin angular momentum as a magnetic dipole, like a tiny bar magnet. Consider an ensemble of protons. In absence of an external magnetic field, no direction in space is 'preferred' over another. Thus, the *net magnetisation* of the ensemble is essentially zero. But when a magnetic dipole is placed in a static magnetic field $\vec{B_0}$, a torque $\vec{\mu} \times \vec{B_0}$ is created which acts as a force perpendicular to both the static field and the direction of the angular momentum. The consequence of this is that, instead of aligning perfectly and statically with $\vec{B_0}$, the protons fall into *precession*, a circular rotation about the field direction at a constant angle. Again, a quantum mechanically slightly inaccurate but helpful image is that of a spinning top. The *Larmor frequency* ω_0 of this precession depends on the magnetic flux

$$f_o = \gamma B_o$$
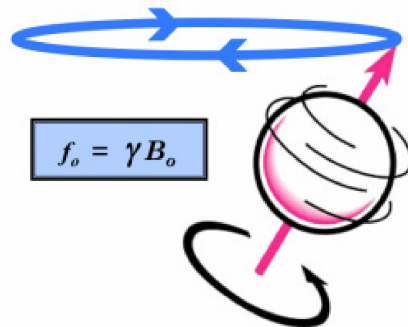
Figure 4.3.: Representation of a precessing nucleus. While a helpful visualisation, particles possessing spin are not actually physically spinning. (from [10])

density and the gyromagnetic ratio of the nucleus via the Larmor relationship $\omega_0 = \gamma B_0$. Upon application of the magnetic field, the parallel spin state in the direction of $\vec{B_0}$ now has slightly lower magnetic energy, causing more nuclei in the ensemble to align that way[2]. This leads to a distribution of spin polarisation that is stable but not microscopically static: The individual spins all still precess and even 'wander' between states, but the distribution overall remains the same, creating a small positive longitudinal net magnetisation $\vec{M}$ in the direction of the magnetic field $\vec{B_0}$.

Note. *When regarding the macroscopic net magnetisation vector $\vec{M}$, it suffices to use mostly*

---

[2]For a more detailed exploration of the individual 'wandering' of spins that eventually leads to this alignment, see reference [22].

descriptions from classical physics for subsequent explanations. The less intuitive explanatory approach using quantum mechanics arrives at the same results and is thus left out here.

Consider again the three-dimensional coordinate system with directions x, y, z, where $\vec{B_0}$ points in z-direction. While the individual protons are precessing about $\vec{B_0}$ at uniform Larmor frequency ω_0, their precession movements are out of phase with each other. Because of this, the net magnetisation vector $\vec{M}$ itself does not have an x-y-component. As its angular momentum is perfectly aligned with $\vec{B_0}$, it does not precess.

4.2.2. Creation of a signal: transverse magnetisation

Neglecting relaxation processes, which we will consider later, the behaviour of $\vec{M}$ in a general magnetic field $\vec{B}$ is described by the simplified Bloch equations[3]

$$\frac{dM_x(t)}{dt} = \gamma(\vec{M}(t) \times \vec{B}(t))_x$$

$$\frac{dM_y(t)}{dt} = \gamma(\vec{M}(t) \times \vec{B}(t))_y$$

$$\frac{dM_z(t)}{dt} = \gamma(\vec{M}(t) \times \vec{B}(t))_z.$$

In order to create a signal, $\vec{M}$ itself has to precess about $\vec{B_0}$. This is where the radiofrequency coils of the scanner come into play: they are used to emit a short duration RF pulse at Larmor frequency ω_0, creating an oscillating magnetic field $\vec{B_1}$ in the x-y-plane, perpendicular to $\vec{B_0}$. Due to the torque from this pulse, $\vec{M}$ is displaced from its equilibrium and starts precessing in the transverse plane, also at Larmor frequency (see figure 4.4).[4] The tipped $\vec{M}$ now produces a fluctuating magnetic field which, by Faraday's law of induction, induces an electromotive force in the RF receiver coil. This is the signal.

4.2.3. $T1$ and $T2$ relaxation

Let M_{xy} be the transverse magnetisation in the x-y-plane and M_z the longitudinal magnetisation along the z-axis. After excitation by the RF pulse, once $\vec{B_1}$ is shut off again, $\vec{M}$ starts realigning with $\vec{B_0}$ and M_z approaches its initial equilibrium value from before excitation, as increasing numbers of spins revert back to the lower energy parallel orientation. This process is called *T1 relaxation*. Assuming a tip angle of 90° after excitation, the

---

[3]Different formulations of the Bloch equations commonly use both the magnetic flux density B and the magnetic field strength H. Both qualities are closely related via $B = \mu_0 H$, where μ_0 is the permeability of the vacuum ([23]). In modern MRI literature, B is usually preferred due to its direct relation to the Larmor frequency via $\omega_0 = \gamma B$, the magnetic flux density is what effectively influences the behaviour of the magnetic moments.

[4]Although often depicted otherwise, the tipped net magnetisation vector $\vec{M}$ does not mean that the spins are now all in resonance (or in-phase) with each other. In fact, only a small fraction of them are. There is merely enough of a 'tendency' and closeness of phases such that, in net, there is precession in the x-y-plane. For more on this see reference [10], subpage on phase coherence.
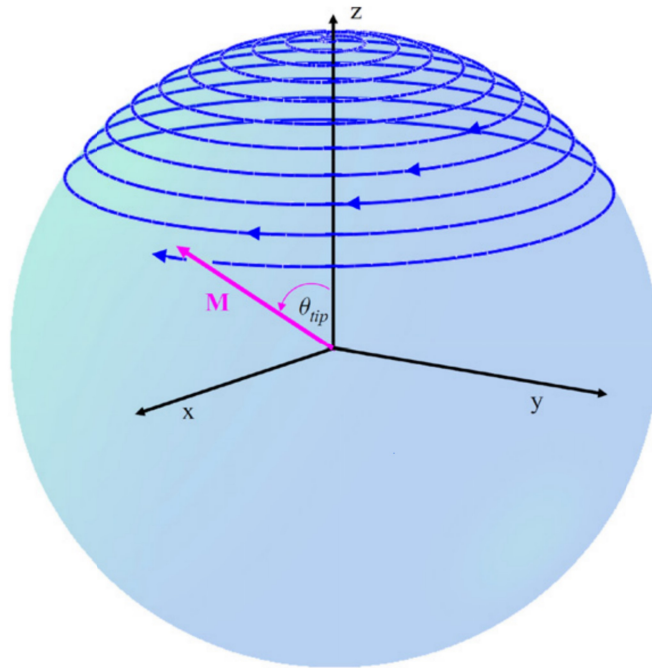
Figure 4.4.: Net magnetisation $\vec{M}$ being tipped into precession by oscillating field $\vec{B_1}$. (from [9])

longitudinal relaxation time $T1$ is the time after which M_z has returned to $(1 - \frac{1}{e})$ of its equilibrium value. It is strongly dependent on the magnetic flux density B_0.

Additionally, spins go out of phase with each other within the transverse plane due to spin-spin interactions, contributing to *T2 relaxation*, i.e., the decay of M_{xy}. Analogously to before, for a 90° tip angle, $T2$ is the time it takes for M_{xy} to decrease to $\frac{1}{e}$ of its initial post-excitation value. Since both spin-spin interactions and spin flips towards realignment with $\vec{B_0}$ contribute to the decay of the transverse magnetisation, $T2$ is significantly smaller than $T1$. In practice, M_{xy} often decreases at a faster rate than atomic interactions alone would suggest. This shorter effective relaxation time is denoted $T2^*$ and occurs mainly due to inhomogeneities in $\vec{B_0}$, as even small inconsistencies significantly speed up dephasing in the transverse plane. Taking relaxation into concern, the Bloch equations read

$$\frac{dM_x(t)}{dt} = \gamma(\vec{M}(t) \times \vec{B}(t))_x - \frac{M_x(t)}{T_2}$$
$$\frac{dM_y(t)}{dt} = \gamma(\vec{M}(t) \times \vec{B}(t))_y - \frac{M_y(t)}{T_2}$$
$$\frac{dM_z(t)}{dt} = \gamma(\vec{M}(t) \times \vec{B}(t))_z - \frac{M_z(t) - M_0}{T_1}.$$

Since relaxation times depend on the spins' local environments, they differ between materials, such as tissue types in the human body. These discrepancies allow for contrast in the produced image. The specific sought-after contrast is attained by choice of magnetisation scheme and the timing of the signal read-out. A deeper exploration of scan design choices

regarding $T1$- vs. $T2$-weighted imaging and their implications for image contrast is beyond the scope of this thesis.

4.2.4. Spatial encoding

In order to produce a useful image, the signal induced in the receiver coil(s) must be made locatable. This is done via spatial encoding using the remaining major component of the machine: gradient coils which produce additional magnetic fields in z-direction with linear variations in field strength along each axis.

The magnetic field during activity of the gradient coils is then

$$B^{total}(x, y, z) = B_0 + G_X x + G_Y y + G_Z z,$$

where G_I is the gradient in the respective direction (see figure 4.5). Since the precession

a) X-gradient	b) Y-gradient	c) Z-gradient
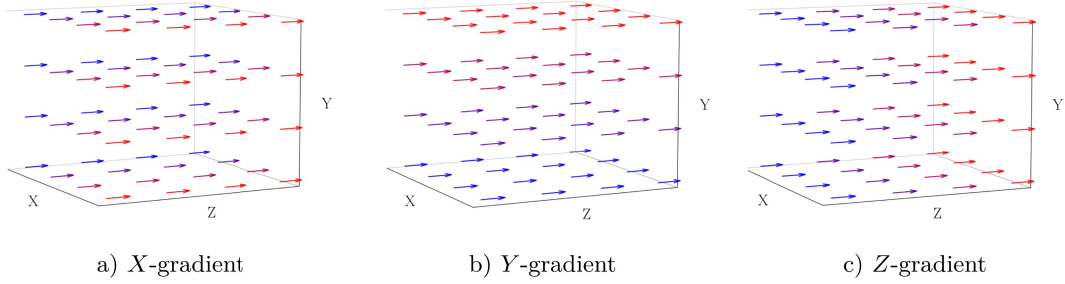
Figure 4.5.: B^{total} during activity of the respective gradient coil, blue denoting lower and red higher flux density.

frequency of a proton depends on the local magnetic flux density, this makes the frequency of a signal a function of position in space

$$f(x, y, z, t) = \gamma \cdot B^{total}(t) = \gamma \cdot (B_0 + G(t) \cdot (x, y, z)^\top),$$

where $G(t) = (G_X(t), G_Y(t), G_Z(t))$ at time t. Via choice of gradient application schemes, spatial patterns of spin phases can thus be encoded into the scanned subject.

4.2.5. The signal

Let $V \subset \mathbb{R}^3$ be the imaging volume of the scanner. Let $\rho(x, y, z)$ be the proton spin density in the transverse plane at location (x, y, z), i.e., the unknown we want to obtain. Then define by

$$\phi(x, y, z, t) = \gamma \cdot \left(\int_0^t G(s) ds \right) \cdot (x, y, z)^\top$$

the accumulated local phase offset of spins at location (x, y, z) by time t as encoded using the gradient coils, i.e., the known we control. Then the signal detected in the receiver coil at any time t is

$$S(t) = \int_V \rho(x, y, z) \cdot e^{-i\omega_0 - i\phi(x, y, z, t)} d(x, y, z),$$

the composite of all spin frequencies. Let

$$k_I(t) = \frac{\gamma}{2\pi} \left(\int_0^t G_I(s)ds \right) \text{ for } I = X, Y, Z,$$

and define the k-space vector $\mathbf{k} := (k_X, k_Y, k_Z)$. Using notation $\mathbf{r} := (x, y, z)^\top$, we can then rewrite ϕ as

$$\phi(x, y, z, t) = 2\pi \mathbf{k}(t) \cdot \mathbf{r}$$

and receive the signal expression

$$S(t) = e^{-i\omega_0 t} \int_V \rho(\mathbf{r}) \cdot e^{-i2\pi \mathbf{k}(t) \cdot \mathbf{r}} d\mathbf{r},$$

where we pulled the term $e^{-i\omega_0 t}$ out of the integral. Since time is an implicit function of $\mathbf{k}$ and the last integral is the Fourier transform of ρ with respect to $\mathbf{k}$, we obtain

$$S(\mathbf{k}(t)) = \mathcal{F}(\rho)(\mathbf{k}(t)),$$

and

$$S(t) = e^{-i\omega_0 t} S(\mathbf{k}(t)).$$

The factor $e^{-i\omega_0 t}$ does not contribute to the spatial information that is encoded in $\rho(\mathbf{r})$ and can be removed by demodulation of the signal, thus we can disregard it. Now, ρ is recovered by applying the inverse Fourier transform and we receive

$$\rho(\mathbf{r}) = \mathcal{F}^{-1}(S(\mathbf{k}))(\mathbf{r}).$$

In practice, the signal is acquired as a set of computer-readable digitised samples and not a continuous analogue signal. Thus, the (inverse) truncated discrete Fourier transform is needed instead.

4.3. The gradient echo pulse sequence

In order to gather a full image, excitation of spins, spatial encoding and signal read-out are done using specifically designed combinations of radiofrequency and gradient pulses. These are called *pulse sequences*. In the following, an exemplary *gradient echo* (GRE) pulse sequence is described in more detail.

4.3.1. Slice selection

Only two properties of any proton spin are measurable in the signal: phase and frequency. Thus, the information suffices for localisation in two dimensions but not in three [9]. To circumvent this issue, a 2D slice to be imaged is selected first by making use of the fact that a radiofrequency pulse only excites protons spinning at its own frequency. A slice-selection-gradient is applied during emission of the RF pulse. This gradient can be chosen to select a slice in any orientation and at any position of the scanned object. For simplicity, and because this is the case for the data used in the numerical experiments in section 6 of

$$B_0 + G_Z z$$

Transmitted radiofrequencies
$[\omega_s - \Delta\omega, \omega_s + \Delta\omega]$,
where
$\omega_s \pm \Delta\omega = \gamma(B_0 + G_Z(z_s \pm \Delta z))$

Chosen slice at $[z_s - \Delta z, z_s + \Delta z]$

Figure 4.6.: Slice selection.

this thesis, we assume a pure Z-gradient, selecting a slice perpendicular to the z-axis, as illustrated in figure 4.6. During application of the gradient, the spins experience slightly different magnetic flux densities along z and thus precess at varying frequencies, going increasingly out of phase with each other. In order to reverse this effect, once the slice is selected, the negative of the selection-gradient is emitted, getting the excited spins within the slice back in-phase. Since any signal originates only from excited spins, the acquired signal now pertains exclusively to the selected slice.

4.3.2. The k-space formalism and cartesian sampling

The acquired signal for any spatial frequency tuple (k_X, k_Y) is stored in so-called *k-space*. Despite naming conventions, this is not a mathematical space but better thought of as a $(2\Phi + 1) \times (2\Phi + 1)$ grid or matrix of data points, where Φ is the scan's cutoff frequency (see figure 4.7).

a) Each pixel in k-space represents a spatial frequency, with pixel intensity corresponding to the weight of the respective spatial frequency's contribution to the image. The further from the centre, the higher the frequency.

b) Representation of an image of Lincoln in k-space, illustrating higher and lower frequencies.

Figure 4.7.: The k-space formalism, depicted as a grey-scale magnitude image. (from [12])

There are various approaches to filling k-space, i.e., collecting the data for all frequency tuples. One of the most commonly used schemes is *cartesian sampling*. It gets its name

a) Cartesian sampling   b) Echo-planar or 'zig-zag' sampling

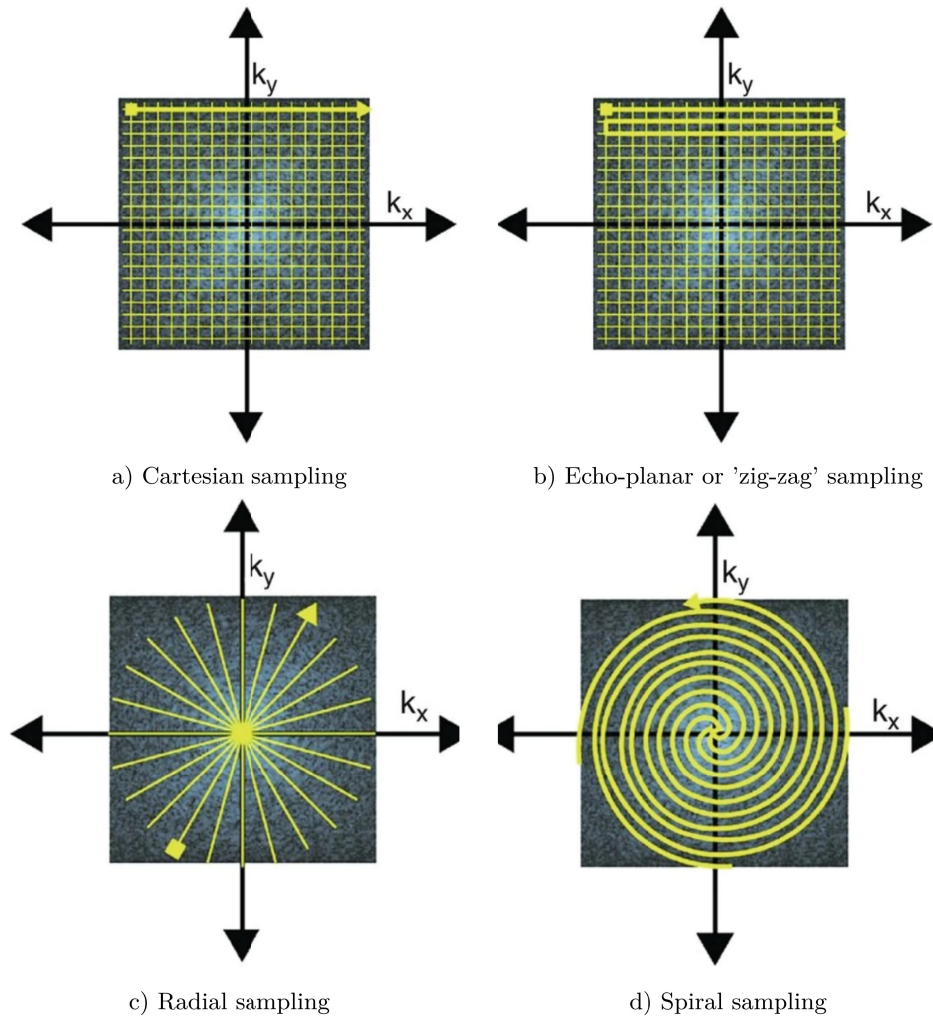c) Radial sampling   d) Spiral sampling

Figure 4.8.: Trajectories in k-space sampling. (from [24])

from the 'trail' along which the k-space data is sampled. After slice selection, a *phase encoding*-gradient is applied until the desired starting phase pattern is reached. In our case, this is represented by the upper-left corner of k-space in the first iteration, with the gradient consisting of a positive Y- and a negative X-gradient. Then, during the signal read-out, a *frequency encoding*-gradient is active. For cartesian sampling, this is a positive X-gradient, such that the entire first line in k-space is sampled, containing all required values of k_X for the fixed k_Y (see figure 4.8). This sequence of slice selection, phase encoding and frequency encoding during readout is then repeated for varying intensities of the Y-component in the phase encoding-gradient, such that in each iteration a different line of k-space is sampled (see figure 4.9). The time passing between the RF pulse exciting the spins and the midpoint of the read-out is called *time to echo*, referred to as TE. The delay time between repetitions of the full sequence is called *repetition time* or TR and is usually significantly longer, since
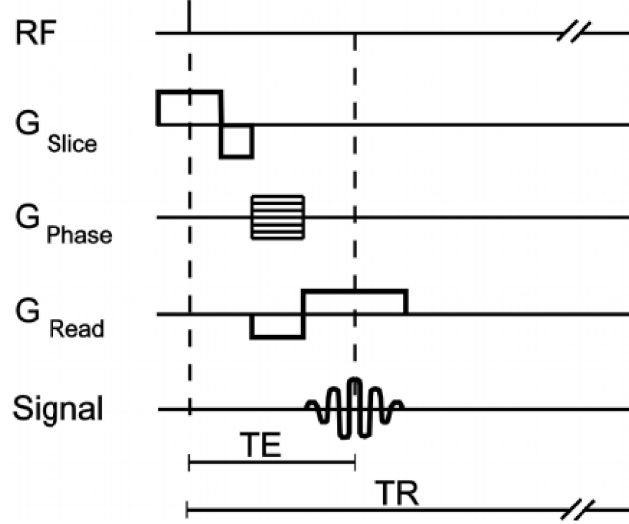
Figure 4.9.: GRE pulse sequence. (from [25])

the phases of the spins have to return to the chosen initial 'neutral' location in k-space $((k_X, k_Y) = (0,0)$ in our case) before the sequence can be started over. This may be done actively via additional application of gradients or passively by waiting for the transverse magnetisation to decay naturally due to $T1$ and $T2$ relaxation. The choice of TR has varying implications for the scan. It crucially affects the contrast between tissues in the retrieved image as well as the overall time needed for the full scan to be completed. There is a great variety of differing pulse sequences and sampling schemes. For example, besides gradient echo sequences as described here, spin echo sequences [26] are also very common, and in place of cartesian one might choose radial [27] or spiral [28] sampling schemes. In this thesis however, we adapt the reconstruction method to work specifically for MRI data gathered using a gradient echo sequence with cartesian sampling as described here.

CHAPTER 5

The MRI observation operator

We now construct an MRI-adapted observation operator. Based on our description of the MRI scanning process from chapter 4, an observation operator Ob appropriately describing the MRI setting with cartesian sampling should

1. be based on the truncated Fourier transform $\mathcal{F}_{(\Phi_0, \Phi_1)}$ for a tuple (Φ_0, Φ_1) of cutoff frequencies, sampling a $(2\Phi_0 + 1) \times (2\Phi_1 + 1)$ k-space, and

2. account for the passage of time between k-space lines.

For our experiments on real data, a third property has to be considered. The particle configurations in the real scan data we use in experiments in chapter 6 consist of small amounts ('particles') of iron placed in an agarose-gel. A detailed description of the data and acquisition process is found in section 6.3.1. In short, the iron particles cause signal voids that show up in the scan images as hypointense spots of non-zero radius. Thus, we additionally require the MRI observation operator to

3. take into consideration the non-zero radius of the area of influence of a particle on the image.

We reconstruct particles in a two-dimensional slice image and thus consider $\Omega \subset \mathbb{R}^2$.

Definition 58 (MRI observation operator without convolution). *Let* $\Phi = (\Phi_0, \Phi_1)$ *be a tuple of line and column cutoff frequencies. For a measurement time* $t \in \mathcal{T}$ *and snapshot* $u_t \in \mathcal{M}(\Omega)$, *define the MRI observation operator* Ob_p^q *for the q-th line and p-th column of k-space lines as*

$$
\begin{aligned}
\mathrm{Ob}_p^q(\Phi)u_t &= \mathcal{F}\left(u_{t+q\Delta t}\right)(-\Phi_0 + q, -\Phi_1 + p) \\
&= \left(\int_\Omega e^{-2\pi i \cdot x \cdot (-\Phi_0 + q, -\Phi_1 + p)} \cdot u_{t+q\Delta t}(x)\, dx\right),
\end{aligned}
\tag{5.1}
$$

where Δt *is the time passing between lines. Summarising the full q-th line in*

$$
\begin{aligned}
\mathrm{Ob}^q(\Phi)u_t &= \left(\mathrm{Ob}_p^q(\Phi)u_t\right)_{p \in \mathbb{N}_0,\, p \leq 2\Phi_1} \\
&= \left(\int_\Omega e^{-2\pi i \cdot x \cdot (-\Phi_0 + q, -\Phi_1 + p)} \cdot u_{t+q\Delta t}(x)\, dx\right)_{p \in \mathbb{N}_0,\, p \leq 2\Phi_1},
\end{aligned}
\tag{5.2}
$$

construct the full operator by collecting all values within the k-space window specified by the cutoff frequencies. Define the MRI observation operator for cartesian sampling *with respect to cutoff frequency tuple* $\Phi = (\Phi_0, \Phi_1)$ *as*

$$
\mathrm{Ob}(\Phi)u_t = \left(\mathrm{Ob}^q(\Phi)u_t\right)_{q \in \mathbb{N}_0,\, q \leq 2\Phi_0}.
\tag{5.3}
$$

The first two conditions are already fulfilled by this operator. In order to account for the non-zero radius of the effect of particles on the scan, we convolve the snapshot u_t with the characteristic function $\mathbb{1}_B$ of a ball $B := B_r\left((0,0)\right)$ of radius r, representing the region affected by a single particle. For simplicity, we assume here the same radius r for all particles. Then the convolution theorem (see [29]) gives that

$$\mathcal{F}(\mathbb{1}_B * u_t)(\xi) = \mathcal{F}(\mathbb{1}_B)(\xi) \cdot \mathcal{F}(u_t)(\xi) \quad \text{for all } \xi \in \mathbb{R}^2, \tag{5.4}$$

and thus we define the following adaptation of the observation operator to include convolution.

Definition 59 (MRI observation operator with convolution). *For Φ, t, u_t and Δt as in definition 58 and $B = B_r((0,0))$ with radius r, we define the MRI observation operator $\overline{\mathrm{Ob}}_p^q$ with convolution for the q-th line and p-th column of k-space as*

$$
\begin{aligned}
\overline{\mathrm{Ob}}_p^q(\Phi)u_t &= \mathcal{F}\left(\mathbb{1}_B * u_{t+q\Delta t}\right)\left(-\Phi_0 + q, -\Phi_1 + p\right) \\
&\overset{(5.4)}{=} \mathcal{F}\left(\mathbb{1}_B\right)\left(-\Phi_0 + q, -\Phi_1 + p\right) \cdot \mathrm{Ob}_p^q(\Phi)u_t,
\end{aligned}
\tag{5.5}
$$

where

$$\mathcal{F}\left(\mathbb{1}_B\right)(\xi) = \int_B e^{2\pi i \cdot x \cdot \xi}\, dx$$

for any frequency tuple ξ. Analogously to definition 58, collect the full q-th k-space line in

$$\overline{\mathrm{Ob}}^q(\Phi)u_t = \left(\overline{\mathrm{Ob}}_p^q(\Phi)u_t\right)_{p \in \mathbb{N}_0,\, p \leq 2\Phi_1}. \tag{5.6}$$

Then the MRI observation operator for cartesian sampling with convolution *with respect to cutoff frequency tuple $\Phi = (\Phi_0, \Phi_1)$ is*

$$\overline{\mathrm{Ob}}(\Phi)u_t = \left(\overline{\mathrm{Ob}}^q(\Phi)u_t\right)_{q \in \mathbb{N}_0,\, q \leq 2\Phi_0}. \tag{5.7}$$

This observation operator now satisfies all three of the desired properties.

CHAPTER 6

Numerical experiments

In this chapter, we assess the performance of the reconstruction method in numerical experiments on both simulated datasets and real data obtained from MRI scans. First, we formulate the discretised optimisation problem. In our discretisation we consider the domain

$$\Omega = [0, 1]^d.$$

For the set of measurement times $\mathcal{T} \subset \Sigma$, assume without loss of generality that the times are centred around 0 such that there is a $T > 0$ with

$$[\min \mathcal{T}, \max \mathcal{T}] = [-T, T]$$

and define the corresponding expanded set of *subtimes* as

$$\mathcal{T}_{\Phi_0} := \{t + q\Delta t \mid t \in \mathcal{T}, q \in \mathbb{N}_0 \text{ with } q \leq 2\Phi_0\},$$

where Δt is the time passing between lines and Φ_0 the line-cut-off frequency. Note that, in contrast to $\mathcal{T}$, the subtimes $\mathcal{T}_{\Phi_0}$ are neither centred around 0 nor in general a subset of Σ. We will consider configurations of particles that stay within Ω for all subtimes, i.e., for the full duration of a scan and denote the set of such particles as

$$\tilde{\Lambda} := \left\{ (x, v) \in \mathbb{R}^d \times \mathbb{R}^d \mid x + \tilde{t}v \in [0, 1]^d \text{ for all } \tilde{t} \in \mathcal{T}_{\Phi_0} \right\}. \tag{6.1}$$

Note that $\tilde{\Lambda}$ differs from Λ as defined in (2.2) in that particles are required to stay within Ω for additional subtimes in $\mathcal{T}_{\Phi_0}$ but not for times in $\Sigma \setminus \mathcal{T}_{\Phi_0}$.

6.1. Discretisation

6.1.1. Discretised snapshots and position-velocity projections

For consistent discretisation we first have to define grids for the Radon measures γ_θ and u_t. Instead of setting fixed grids on Γ and Ω, we define ones that vary with θ and t respectively. This is advantageous because it avoids a loss in degrees of freedom, since a fixed grid would also cover regions of Γ (resp. Ω) which $\mathrm{R}j_\theta$ (resp. $\mathrm{M}v_t$) may not map to for all choices of θ (resp. t). Thus, in order to set appropriate grids, we must first examine the domains of all snapshots and position-velocity projections.

Proposition 60 (Domain of γ_θ (adapted from [3])). *For a given $\theta \in S^{d-1}$, define*

$$s_+ := \sum_{j:\theta_j > 0} \theta_j \text{ and } s_- := \sum_{j:\theta_j < 0} \theta_j.$$

The set $\mathrm{Rj}_\theta(\tilde{\Lambda}) \subset \Gamma$ *is a parallelogram in* $\mathbb{R}^2$ *with vertices*

$$\begin{pmatrix} s_- \\ 0 \end{pmatrix}, \begin{pmatrix} s_+ \\ 0 \end{pmatrix}, \begin{pmatrix} \frac{s_+ + s_-}{2} \\ \frac{s_+ - s_-}{2(T + 2\Phi_0 \Delta t)} \end{pmatrix} \begin{pmatrix} \frac{s_+ + s_-}{2} \\ \frac{s_- - s_+}{2(T + 2\Phi_0 \Delta t)} \end{pmatrix}.$$

Proposition 61 (Domain of u_t (adapted from [3])). *Let* $t \in \mathbb{R}$ *be given.*

1. *If* $|t| \leq T + 2\Phi_0 \Delta t$, *we have* $\mathrm{Mv}_t^d(\tilde{\Lambda}) = [0, 1]^d$.

2. *If* $|t| > T + 2\Phi_0 \Delta t$, *we have* $\mathrm{Mv}_t^d(\tilde{\Lambda}) = \left[\frac{1}{2} - \frac{|t|}{2(T + 2\Phi_0 \Delta t)}, \frac{1}{2} + \frac{|t|}{2(T + 2\Phi_0 \Delta t)} \right]^d$.

Proof. Both domains follow via the proofs of the corresponding propositions 78 and 79 in [3] by simply replacing T with $T + 2\Phi_0 \Delta t$. $\qquad \square$

We then define grids $G_u(t)$ and $G_\gamma(\theta)$ by linearly mapping a regular rectangular $M \times M$ grid to the domains as described in propositions 60 and 61. The snapshots u_t are now discretised as vectors $\vec{u}_t \in \mathbb{R}^{M^d}$, where each vector entry is the value of the piecewise constant u_t on the respective grid cell, multiplied by the cell volume. The $\vec{\gamma}_\theta \in \mathbb{R}^{M^2}$ are defined analogously.

6.1.2. Discretised Radon and move operators

In the numerical experiments we will only regard the setting for $d = 2$. For simplicity, we restrict the discretisation of Mv_t^d and Rd_θ to this case as well. Note that $\mathrm{Rd}_\theta u_t$ is a measure on the one-dimensional Ξ and consider its domain.

Proposition 62 (Domain of $\mathrm{Rd}_\theta u_t$). *Let* $\theta \in \Theta$ *and* $t \in \Sigma$, *with* s_+ *and* s_- *as in proposition 60.*

1. *If* $|t| \leq T + 2\Phi_0 \Delta t$, *we have* $\mathrm{Rd}_\theta \left(\mathrm{Mv}_t^2(\tilde{\Lambda}) \right) = [s_-, s_+]$

2. *If* $|t| > T + 2\Phi_0 \Delta t$, *we have*

$$\mathrm{Rd}_\theta \left(\mathrm{Mv}_t^2(\tilde{\Lambda}) \right) = \left[\frac{s_+ + s_-}{2} - \frac{t(s_+ - s_-)}{2(T + 2\Phi_0 \Delta t)}, \frac{s_+ + s_-}{2} + \frac{t(s_+ - s_-)}{2(T + 2\Phi_0 \Delta t)} \right].$$

Proof.

$$\mathrm{Rd}_\theta \left(\mathrm{Mv}_t^2(\tilde{\Lambda}) \right) = \mathrm{Mv}_t^1 \left(\mathrm{Rj}_\theta(\tilde{\Lambda}) \right)$$

$$\overset{(\text{prop.60})}{=} \mathrm{Mv}_t^1 \left(\mathrm{conv} \left\{ \begin{pmatrix} s_- \\ 0 \end{pmatrix}, \begin{pmatrix} s_+ \\ 0 \end{pmatrix}, \begin{pmatrix} \frac{s_+ + s_-}{2} \\ \frac{s_+ - s_-}{2(T + 2\Phi_0 \Delta t)} \end{pmatrix}, \begin{pmatrix} \frac{s_+ + s_-}{2} \\ \frac{s_- - s_+}{2(T + 2\Phi_0 \Delta t)} \end{pmatrix} \right\} \right)$$

$$= \mathrm{conv} \left\{ s_-, s_+, \frac{s_+ + s_-}{2} + \frac{t(s_+ - s_-)}{2(T + 2\Phi_0 \Delta t)}, \frac{s_+ + s_-}{2} - \frac{t(s_+ - s_-)}{2(T + 2\Phi_0 \Delta t)} \right\}$$

$$\square$$

Let $G_r(\theta, t)$ be the one-dimensional grid on domain $\mathrm{Rd}_\theta(\mathrm{Mv}_t^d(\tilde{\Lambda}))$, with M equispaced grid cells. Denote by $(G_r(\theta, t))_i = [r_i, r_{i+1}]$ and $(G_u(t))_j$ the i-th and j-th cells of the

respective grids. Then we define the discretised Radon operator Rd_θ for $\mathrm{Rd}_\theta u_t$ as the matrix $M_{\mathrm{Rd}}(t, \theta) \in \mathbb{R}^{M \times M^2}$ with entries

$$(M_{\mathrm{Rd}}(t, \theta))_{i,j} = \mathrm{area}\left(\left\{x \in \mathbb{R}^2 \mid \theta \cdot x \in (G_r(\theta, t))_i\right\} \cap (G_u(t))_j\right).$$

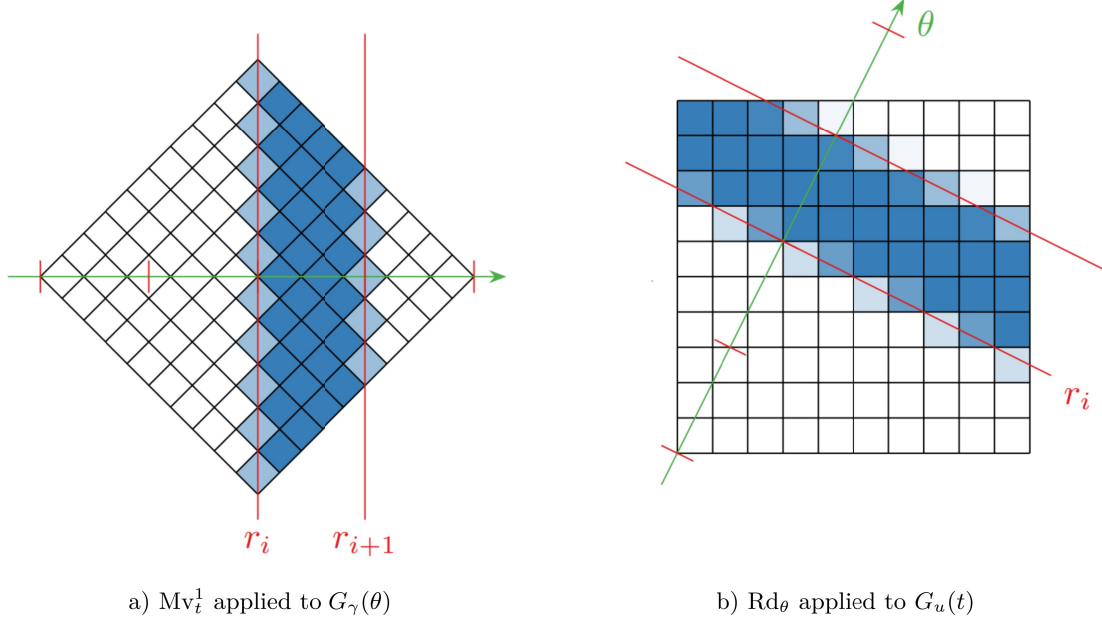a) Mv_t^1 applied to $G_\gamma(\theta)$ b) Rd_θ applied to $G_u(t)$

Figure 6.1.: Illustration of grids and projections with grid cells $(G_r(\theta, t))_i = [r_i, r_{i+1}]$ depicted as red bins dividing the green line in projection direction θ. The area of intersection of a bin with a grid cell $(G_u(\theta, t))_j$ is represented in the cell shade, where the deeper the shade the larger the intersection. (from [3])

Let $\theta(t) = \frac{(1,t)}{\sqrt{1+t^2}} \in S^1$ then the matrix $M_{\mathrm{Mv}}(\theta, t) \in \mathbb{R}^{M \times M^2}$ discretising the move operator Mv_t^1 for $\mathrm{Mv}_t^1 \gamma_\theta$ is defined analogously via

$$(M_{\mathrm{Mv}}(\theta, t))_{i,j} = \mathrm{area}\left(\left\{x \in \mathbb{R}^2 \mid \theta(t) \cdot x \in (G_r(\theta(t), t))_i\right\} \cap (G_\gamma(\theta))_j\right).$$

For an illustration of these intersections, see figure 6.1.

6.1.3. Discretisation of the measurement term

Simulated target data

The ground truths for the simulated experiments are configurations of $4 \leq N \leq 20$ particles each, with initial locations $x_i \in [0, 1]^2$, move vectors $v_i \in \mathbb{R}^2$ and weights $m_i \in \mathbb{R}_{\leq 0}$. We now define measurement target data f_t for such a simulated configuration.

Note. *Since the simulation of a non-zero particle radius would consist in multiplication with the same convolution matrix (see below) in the definitions of both the targets f_t and*

the observation operator Ob, *this would constitute an „inverse crime" and not have any influence on the minimisation of the measurement term. Thus, we do not convolute with* $\mathbb{1}_{B_r}$ *in the following definition of* f_t.

Consider a single ground truth particle (x_n, v_n) and let Φ_0 and Φ_1 be line and column cut-off frequencies. The signal acquired for the q-th line and p-th column of k-space via cartesian sampling at measurement time $t \in \mathcal{T}$ is then

$$\begin{aligned} f_p^q(x_n, \Phi) &= \mathcal{F}(\delta_{x_n + t_q v_n})(-\Phi_0 + q, -\Phi_1 + p) \\ &= e^{-2\pi i \cdot (x_n + t_q v_n) \cdot (\Phi_0 + q, \Phi_1 + p)}, \end{aligned}$$

where $\mathcal{F}$ is the Fourier transform and $t_q = t + q\Delta t$. Then the signal attained for the q-th line in k-space via cartesian sampling with cutoff frequency tuple $\Phi = (\Phi_0, \Phi_1)$ is the truncated Fourier series

$$f^q(x_n, \Phi) = \left(\mathcal{F}(\delta_{x_n + t_q v_n})(-\Phi_0 + q, -\Phi_1 + p) \right)_{0 \leq p \leq 2\Phi_1}.$$

For a measurement time $t \in \mathcal{T}$, we have

$$f_t(x_n, \Phi) = (f^q(x_n, \Phi))_{0 \leq q \leq 2\Phi_0},$$

and thus, the full scan data for all particles in the configuration and all measurement times is the sum

$$f_t(\Phi) = \left(\sum_{n=1}^N f_t(x_n, \Phi) \right)_{t \in \mathcal{T}} \in \mathbb{C}^{|\mathcal{T}| \cdot (2\Phi_0 + 1) \cdot (2\Phi_1 + 1)}. \tag{6.2}$$

Observation operator

Following the definition of Ob in definition 58, we discretise the MRI observation opertor with respect to cutoff frequency tuple $\Phi = (\Phi_0, \Phi_1)$ as the matrix

$$M_{\mathrm{Ob}}(t, \Phi) = \begin{pmatrix} \mathrm{block}(-\Phi_0) & & \\ & \ddots & \\ & & \mathrm{block}(\Phi_0) \end{pmatrix} \tag{6.3}$$

where

$$\mathrm{block}(q) = \begin{pmatrix} e^{-2\pi \cdot (q, -\Phi_1) \cdot gp_0} & \dots & e^{-2\pi \cdot (q, -\Phi_1) \cdot gp_{M^2}} \\ \vdots & \ddots & \vdots \\ e^{-2\pi \cdot (q, \Phi_1) \cdot gp_0} & \dots & e^{-2\pi \cdot (q, \Phi_1) \cdot gp_{M^2}} \end{pmatrix}, \tag{6.4}$$

where $gp_k \in [0, 1]^2$ is the centre point of the k-th grid cell of reconstruction grid $G_u(t)$. As reasoned above, we do not consider a particle radius in the simulated experiments. On the real scan data however, we test for various radii r by multiplying the measurement operator

with

$$M_{conv}(\Phi) = \begin{pmatrix} \mathcal{F}\left(\mathbb{1}_{B_r(0)}\right)(-\Phi_0,-\Phi_1) & & & & \\ & \ddots & & & \\ & & \mathcal{F}\left(\mathbb{1}_{B_r(0)}\right)(-\Phi_0+1,-\Phi_1) & & \\ & & & \ddots & \\ & & & & \mathcal{F}\left(\mathbb{1}_{B_r(0)}\right)(\Phi_0,\Phi_1) \end{pmatrix}$$

$$\in \mathbb{C}^{(2\Phi_0+1)\cdot(2\Phi_1+1)},$$

receiving the observation matrix with convolution

$$\overline{M}_{\mathrm{Ob}}(t,\Phi) := M_{conv}(\Phi) \cdot M_{\mathrm{Ob}}(t,\Phi). \tag{6.5}$$

Discretised optimisation problem

We now state the discretised optimisation problem by replacing the continuous variables and operators from $\mathrm{P}_\alpha(f)$ with their discretised versions. Additionally, instead of the strict contraint $\mathrm{Rd}_\theta u_t = \mathrm{Mv}_t^1 \gamma_\theta$, we use a softened constraint with bound τ in order to avoid discretisation artefacts. For $t \in \mathcal{T}$ and cutoff frequency tuple $\Phi = (\Phi_0, \Phi_1)$, let

$$\vec{U}_t(\Phi) := \left(\vec{u}_{t+q\Delta t}\right)_{q\in\mathbb{N}_0,\, q\leq\Phi_0}.$$

Then we arrive at the discretised formulation of the problem

$$\min_{\substack{\vec{\gamma}_\theta\in\mathbb{R}^{M^2},\theta\in\Theta \\ \vec{u}_t\in\mathbb{R}^{M^2},t\in\Sigma}} \sum_{\theta\in\Theta} \|\vec{\gamma}_\theta\|_1 + \sum_{t\in\Sigma} \|\vec{u}_t\|_1 + \frac{1}{2\alpha} \sum_{t\in\mathcal{T}} \|M_{\mathrm{Ob}}(t,\Phi)\vec{U}_t(\Phi) - f_t(\Phi)\|_2^2$$

$$\text{such that} \quad \left(\sum_{\substack{\theta\in\Theta, \\ t\in\Sigma}} \|M_{\mathrm{Mv}}(\theta,t)\vec{\gamma}_\theta - M_{\mathrm{Rd}}(t,\theta)\vec{u}_t\|_2^2\right)^{\frac{1}{2}} \leq \tau. \tag{$\mathrm{P}_\alpha^\Phi(f)$}$$

We adopt the choice of $\tau = 0.001$ by Holler et al. in [3], who determined this as a good violation bound using a coarse parameter search.

6.2. Experiments on simulated data

We solve the second-order cone program $(\mathrm{P}_\alpha^\Phi(f))$ with MOSEK [30], a commercial solver for large-scale optimisation problems. All experiments are implemented in python, building extensively on the foundational code used for experiments by Holler et al. in [3] and adapting it to the purposes of this thesis. Where comparisons between methods are made, the original dimension-reduced method using the unaltered truncated Fourier series as the observation operator is in the following simply referred to as *dimred*.

6.2.1. Parameters and postprocessing

We run experiments for sets of measurement times

$$\mathcal{T} := \left\{ \frac{k}{K} \mid k \in \{-K, ..., K\} \right\}$$

for $K = 1, 2$. This corresponds to settings with $|\mathcal{T}| = 3, 5$ full scan images taken respectively. All experiments are implemented for $|\Theta| = 5$ and $|\Sigma \setminus \mathcal{T}| = 3$, where the directions

$$\Theta = \left\{ \exp \left(i\pi \left(\frac{j}{|\Theta|} - \frac{1}{2} \right) \right) \mid j = 0, ..., |\Theta| - 1 \right\}$$

are evenly spaced points with maximum distance on the right half of the unit circle, and additional times $\Sigma \setminus \mathcal{T}$ are chosen accordingly such that the image of the times in S^1 under $t \mapsto \frac{(1,t)}{\sqrt{1+t^2}}$ consists of maximally spaced points as well. For the experiments without noise, we set regularisation parameter $\alpha = 0.005$ instead of using the strict contraint in $(\mathrm{P}_\alpha^\Phi(f))$, and reconstructions are performed on a 100×100 grid.

In regard to cutoff frequencies, performance will be tested and compared for two scenarios:

1. Choices of small equal $\Phi_0 = \Phi_1$, then simply denoted by Φ. In application, this equates to sampling only a very small square k-space and we accordingly name this scenario *k-square*.

2. Gathering few but full k-space lines. This is the more practical realistic setting since the vast majority of scan time in cartesian sampling passes between lines and only very little during the readout of a line itself. Thus, the *full-lines* scenario grants significantly more data with only marginally longer scan times than k-square.

Specifically, we will run tests for $\Phi = 2, 3$ in the k-square scenario and for $\Phi_0 = 2$ in full-lines. For the latter, we would ideally want to imitate the properties of the real scan data used, the sampled k-spaces of which have dimension 196×196. Due to limited computational resources however, we set $\Phi_1 = 40$, thus gathering lines of $2\Phi_1 + 1 = 81$ entries each. This compromise allows for computable numbers of parameters for the MOSEK solver while still providing amounts of additional data that give a solid indication of the difference in reconstruction properties between small square k-spaces and full lines.

Ground truth dataset

We test the adapted method on a dataset of 2000 ground truth particle configurations consisting of four to twenty particles each. In order to have better comparability of results between the different choices of $\mathcal{T}$ and frequency cutoffs, all experiments are conducted using this same dataset. Positions x_i with weights m_i and velocities v_i were generated randomly in accordance with the following rules:

1. All particles must stay within the $[0, 1]^2$ domain for the duration of the simulated scan. We assume that the time passing between the end of one scan and the beginning of the following one is equal to the time Δt that passes between two lines within a single scan, as is accurate for the real scan data in section 6.3. For line frequency cutoff Φ_0

and $\mathcal{T}$ as defined above we thus have

$$\Delta t = \frac{1}{K(2\Phi_0 + 1)}.$$

Then the set of times including the line subtimes is

$$\mathcal{T}_{\Phi_0} = \left\{ \frac{k}{K} + q\frac{1}{K(2\Phi_0 + 1)} \mid -K \leq k \leq K, q \leq 2\Phi_0 \right\}$$

and we have

$$\min(\mathcal{T}_{\Phi_0}) = -1 \text{ for all } K, \Phi_0$$

and

$$\max_{K,\Phi_0}\left(\max(\mathcal{T}_{\Phi_0})\right) = 1 + \max_{\substack{1 \leq K \leq 2 \\ 2 \leq \Phi_0 \leq 3}} \frac{2\Phi_0}{K(2\Phi_0 + 1)},$$

which takes its maximum for $K = 1$ and $\Phi_0 = 3$. Thus, all configurations in the dataset are required to remain within the domain for all times in $\left[-1, 1 + \frac{2 \cdot 3}{1 \cdot (2 \cdot 3 + 1)}\right] = \left[-1, \frac{13}{7}\right]$.

2. Weights m_i are drawn from $[0.9, 1.1]$ according to a uniform distribution.

3. Define the dynamic separation of a configuration C with respect to a set of times T as the minimal distance between any two particles at any time in T:

$$\Delta_{dyn}(C, T) := \min_{t \in T} \min_{i \neq j} \|x_i + tv_i - (x_j + tv_j)\|. \tag{6.6}$$

In order to investigate the relation between dynamic separation and the rate of correct reconstructions, we want the ground truth separations to be spread evenly on a scale from 0 to 0.1. Due to the dependency on T, we naturally cannot provide a dataset fulfilling this perfectly for all experiment settings. But we choose ground truths such that, for dynamic separation histograms with ten bins, the numbers of configurations in each bin are reasonably similar for both choices of measurement times $\mathcal{T}$, i.e., $|\mathcal{T}| = 3, 5$. The specific histograms are detailed in appendix A.2.

We generate this dataset by using a rejection-sampling method, adapted from [2]. Configurations drawn from the uniform distribution on $\tilde{\Lambda}$ are accepted or rejected based on a predefined acceptance probability which is selected to ensure that the dynamic separation Δ_{dyn} with respect to a set of times $\mathcal{T}$ is uniformly distributed on $[0, 0.1]$. Two such datasets are generated, one for $|\mathcal{T}| = 3$ and one for $|\mathcal{T}| = 5$, and then combined.

Postprocessing and evaluation of results

We evaluate the reconstructions by their results at time $t = 0$. For a ground truth $u_0^\dagger$, consider the reconstructed discretised snapshot u_0 in terms of the weights $\vec{u}_0 \in \mathbb{R}^{100^2}$ at the cell centres of the grid $G_u(0)$ as defined in section 6.1. Reconstruction success is then measured by two aspects:

1. *Particle matching:* A threshold of 0.1 is applied below which all weights in $\vec{u}_0$ are set to zero. The remaining non-zero weights are sorted into clusters and the centre of

mass and summed weights computed for each cluster are defined as the location and weight of a detected particle. These detected particles are then matched to ground truth particles in within a radius of 0.01 and we consider the

$$recall = \frac{\text{\# matched ground truth particles}}{\text{\# all ground truth particles}}$$

and

$$precision = \frac{\text{\# matched detected particles}}{\text{\# all detected particles}}$$

of a reconstruction.

2. *Wasserstein divergence:* We calculate the squared unbalanced Wasserstein divergence $W_{2,R}^2(u_0^\dagger, u_0)$ for $R = 0.05$.

A reconstruction is deemed successful if all particles are matched, i.e., precision = recall = 1 holds, with a squared Wasserstein divergence of less than 0.01.

6.2.2. Method performance

The results for the reconstruction performance of the MRI-adapted method are summarised in table 6.1. A reconstruction attempt is deemed successful if all ground truth and reconstructed particles are fully paired, i.e., there are no spare unmatched particles in either ground truth or reconstruction, with a Wasserstein distance $<= 0.1$. Additionally to the success rate, we consider the computational effort of each setting as indicated by the maximum resident size[1]. In the setting using the least amount of k-space data, namely k-square

	k-square		full-lines
	$\Phi = 2$	$\Phi = 3$	$\Phi_0 = 2$
$|\mathcal{T}| = 3$	747	1230	786
$|\mathcal{T}| = 5$	822	1291	-

(a) Successful reconstructions

	k-square		full-lines
	$\Phi = 2$	$\Phi = 3$	$\Phi_0 = 2$
$|\mathcal{T}| = 3$	13884.74	18601.72	59126.14
$|\mathcal{T}| = 5$	17706.83	27251.03	-

(b) Computational effort

Table 6.1.: Performance of the MRI-adapted method per reconstruction setting. *Table (a)*: Number of successful reconstructions out of 2000. *Table (b)*: Maximum resident set size in MB, taken over all ground truth reconstructions.

with three measurement times and cutoff frequency $\Phi = 2$, already 747 out of 2000 configurations are reconstructed correctly. We consider the expected improvements from the inclusion of more frequencies. While the full-lines setting does obtain 39 additional successful configurations as compared to k-square, this is only a relatively small improvement, especially when taking into consideration that the computational effort is more than quadrupled. More precisely, taking the number of successful reconstructions and computational

---

[1] The resident set size (RSS) of a process is the memory it occupies in the RAM. In our application, every reconstruction attempt of any ground truth is considered a process and the maximum resident set size of a setting is then the maximum taken over the RSS's of all reconstructions in that setting.

effort of k-square with $|\mathcal{T}| = 3$ and $\Phi = 2$ as the base results to compare against, performance is improved with full-lines by $5.22\,\%$ while the effort increases by $425.84\,\%$. The ratios for improvement within k-square are significantly better. From $|\mathcal{T}| = 3$ to $|\mathcal{T}| = 5$, we have $10.04\,\%$ more correctly reconstructed ground truths at a $27.53\,\%$ higher effort. The greatest change however comes with additional k-space lines, as the reconstruction is improved by $64.66\,\%$ at an additional effort of $33.97\,\%$ for $|\mathcal{T}| = 3, \Phi = 3$ and by $72.28\,\%$ at an additional effort of $96.27\,\%$ for $|\mathcal{T}| = 5, \Phi = 3$. In terms of performance-to-effort ratio, the k-square scenario with cutoff $\Phi = 3$ offers the most balanced trade-off.

We additionally run the dimred method in the k-square scenario with $|\mathcal{T}| = 3$ and $\Phi = 2$. As expected, the unaltered method is not successful on the simulated MRI data, no ground truths were reconstructed correctly.

6.2.3. Dynamic separation

We examine to what extent the dynamic separation of configurations may constitute or contribute to a source condition for the reconstruction success of the MRI-adapted method, similar to the source condition stated in remark 47. Figure 6.2 shows the rate of correct reconstructions mapped against the dynamic separations of the ground truths for four settings that differ as follows: On the left-hand side, we consider the dynamic separation $\Delta_{dyn}(C, \mathcal{T})$ of a configuration C for sets $\mathcal{T}$ of measurement times. Since the MRI-adapted method uses k-space data from additional times in $\mathcal{T}_\Phi \setminus \mathcal{T}$, we consider on the right-hand side dynamic separations $\Delta_{dyn}(C, \mathcal{T}_\Phi)$ calculated over the sets $\mathcal{T}_\Phi$ of subtimes and compare results.

In all settings, reconstructions are on average more successful the higher the separation, indicating that dynamic separation may potentially be relevant for the formulation of a source condition. It is intuitive that the correct reconstruction rates are overall higher for $|\mathcal{T}| = 5$ than for $|\mathcal{T}| = 3$, since on the one hand the method is more successful for a higher number of measurement times as we have seen in section 6.2.2, and on the other hand there is the additional effect of the dynamic separation being calculated as the minimum over a larger set of times, thus shifting the curve left. Differences between the left- and right-hand side are attributed exclusively to this second effect due to the larger sets of times $\mathcal{T}_\Phi$ while the reconstruction settings used stay the same. Note here that more times are considered for $\Phi = 3$ than for $\Phi = 2$.

The seemingly counterintuitive dips in the reconstruction rates in 6.2b for k-square with $\Phi = 2$ at dynamic separation 0.07 and in 6.2d for k-square with $\Phi = 3$ at dynamic separation 0.06 can be explained by the fact that the same dataset of ground truth configurations was used for all experiments, leaving significantly fewer configurations in the high-separation bins and thus increasing the impact of single reconstruction successes and failures on the average rate. Precise separation histograms for all four choices of sets of times are given in appendix A.2.

a) $\mathcal{T}$ with $|\mathcal{T}| = 3$.

b) $\mathcal{T}_\Phi$ with $|\mathcal{T}| = 3$.

c) $\mathcal{T}$ with $|\mathcal{T}| = 5$.

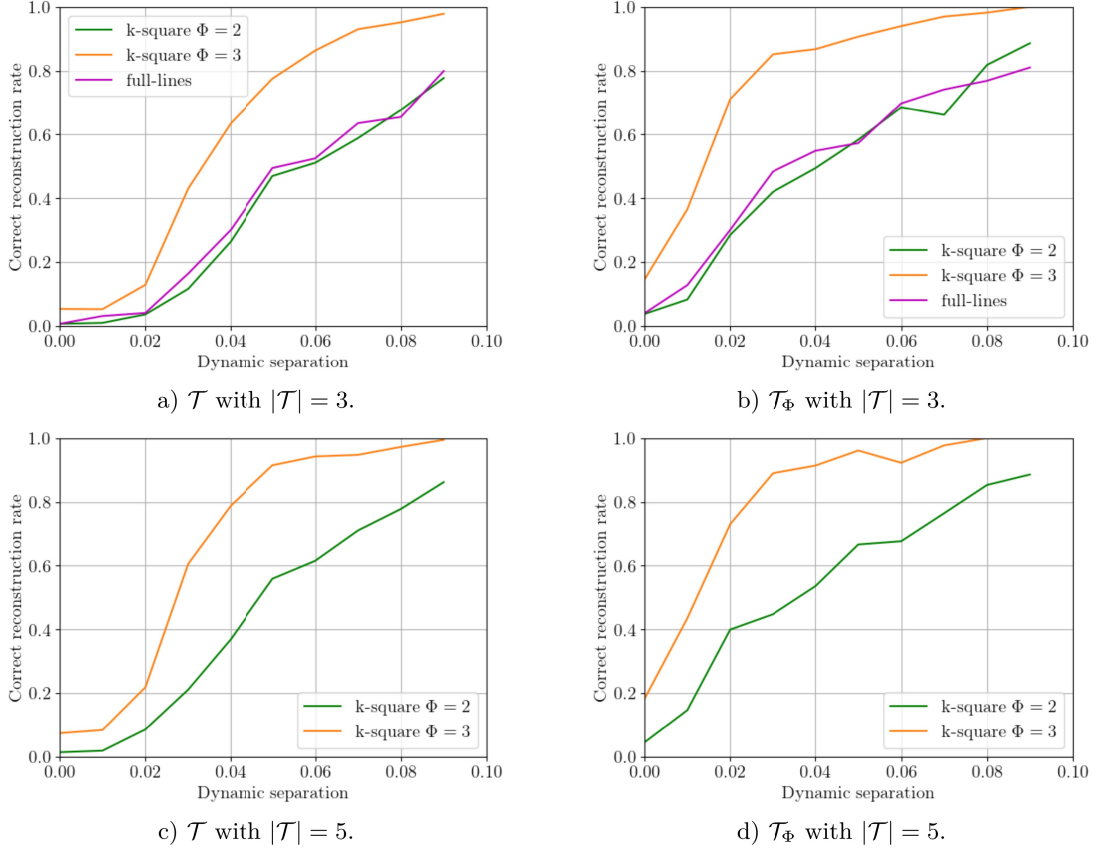d) $\mathcal{T}_\Phi$ with $|\mathcal{T}| = 5$.

Figure 6.2.: Reconstruction rates for varying levels of dynamic separation. We have $|\mathcal{T}| = 3$ in the top row and $|\mathcal{T}| = 5$ in the bottom row. Dynamic separations are calculated over the set of measurement times $\mathcal{T}$ on the left, and over the set of all subtimes $\mathcal{T}_\Phi$ for the respective cutoff frequency Φ on the right.

6.2.4. Experiments with noise

Fix the k-square setting with $|\mathcal{T}| = 3$ and $\Phi = 2$. We now examine the reconstruction properties of the MRI-adapted method for noisy measurements by adding noise to ground truths that were reconstructed correctly in the noise-free case. For noise levels

$$\delta \in \left\{ 10^k \mid k \in \{-3, -2, ..., 3\} \right\},$$

we add Gaussian noise with standard deviation $\sqrt{\frac{2\delta}{150}}$ to the measurements f. Note that

$$\delta = \frac{1}{2} \sum_{t \in \mathcal{T}} \|f_t^\delta - f_t^\dagger\|_H^2$$

then holds by design, since the vectors f as implemented have 150 entries[2]. For each noise level the same set of ground truths is used. From the 747 that were correctly reconstructed

---

[2]The measurement vectors f as defined in (6.2) have 75 complex entries which are split into real and imaginary parts in the implementation.

in the noise-free experiment, a fixed subset of 200 configurations is chosen in order to save computational capacities. For comparability, we set regularisation parameter $\alpha = 0.2\sqrt{\delta}$ as done in the experiments by Holler et al [3].
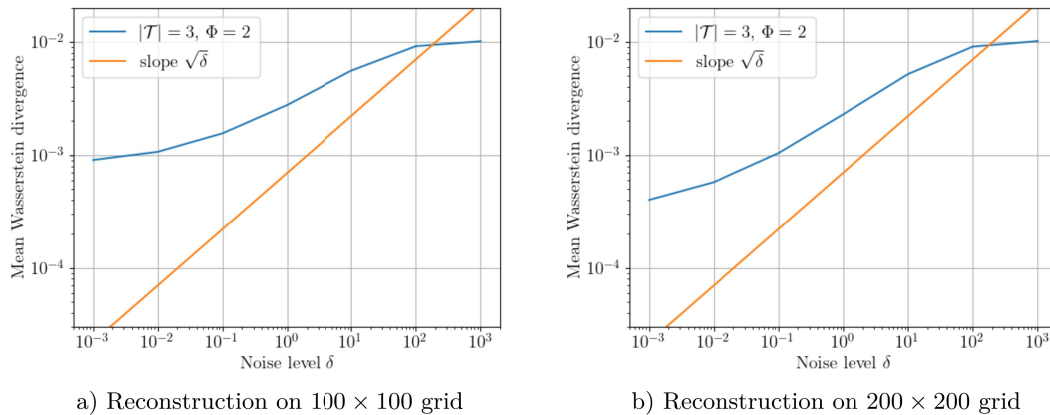

a) Reconstruction on 100×100 grid   b) Reconstruction on 200×200 grid

Figure 6.3.: Reconstruction error for varying levels of noise.

Figure 6.3 depicts the change in mean Wasserstein divergences for varying noise levels δ in comparison with the slope $\sqrt{\delta}$ that was obtained in section 3.2 for the general dimension-reduced method. Notably, the mean divergence for $\delta = 10^{-3}$ is about $0.90 \cdot 10^{-3}$ for reconstructions on a 100×100 grid (see figure 6.3a), whereas reconstructions on a grid of double the resolution yield a mean divergence of about $0.40 \cdot 10^{-3}$ (see figure 6.3b), less than half. With similar mean divergences at noise level $\delta = 10^3$ of about $1.05 \cdot 10^{-2}$ and $1.02 \cdot 10^{-2}$ for the resolutions respectively, this suggests that the reconstruction properties of the method may possibly approach the slope $\sqrt{\delta}$ further when performed on higher resolutions. Further experimentation is needed to examine this.

6.3. Experiments on real MRI data

In this section, we apply the reconstruction methods to real MRI data. After describing the experiment setup and data acquisition process, we discuss issues in the data and post-processing measures to mitigate them, and finally present a comparison of reconstruction performance between the original dimred method and our MRI-adapted version.

6.3.1. Acquisition of real data

The data for the numerical experiments was gathered using a $9.4T$ MRI scanner of the model Bruker Biospec 94/20. In order to mimic particle movement in an environment that is ideally as homogeneous as possible, a rotating phantom system, initially designed for [31], was used. The phantoms themselves are 2 mL Eppendorf tubes, filled with 1% agarose gel, into which microparticles of iron oxide (MPIO) are injected. With 9.2 pg of iron and a mean diameter of about $(8.2 \pm 0.6)\mu g$ per particle, they produce signal voids in the scan which result in hypointense spots in the images which are akin to the voids iron-labelled cells would produce in in vivo experiments. The rotation system is made up

of two modules that are connected via a carbon drive shaft: an aluminium drive frame mounted on the AutoPac table of the scanner and an acrylic glass MRI insert that holds the phantom. Attached to the drive frame is a stepper motor which produces rotation using toothed belts and gearwheels. The MRI insert is comprised of a glass fiber stick set in glass ball bearings with the Eppendorf tube mounted on top, as illustrated in figure 6.4. The glass ball bearings enable smooth rotation of the phantom and ensure a position inside the scanner that is mostly centred. However, in practice, the rotational axis is slightly off-centre and additionally, the tube position is subtly slanted. The effects this has on the data are discussed in more detail in section 6.3.2.
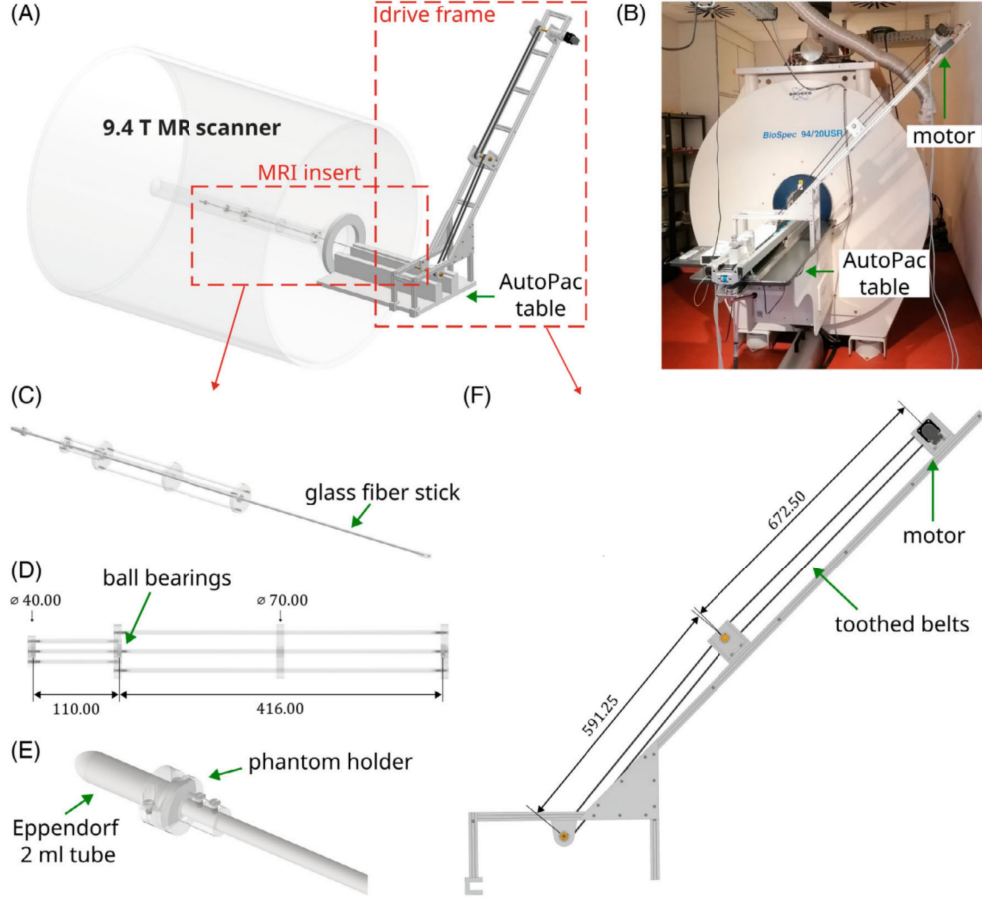

Figure 6.4.: Rotating phantom system used to obtain experiment data (from [31]). The phantom is secured in a phantom holder (E) and mounted on a glass fiber stick that is inserted into the ball bearing construction (D) as depicted in (C) for rotation. The motor and toothed belts driving the rotation are installed on a drive frame (F) that is then fixed to the AutoPac table and operates the movement of the phantom as depicted in design sketch (A) and photo (B).

We used a cartesian sampling scheme with a repetition time (TR) between any two line read-outs of 640 ms and an echo time (TE), i.e., the time passing during the read-out of one k-space line, of 8 ms. The overall span of time per time frame is then $TR \cdot (number\ of\ k\text{-}space\ lines)$. With a field of view (FOV) of 12×12 mm^2, the scans have a resolution of 196×196 pixels

of respective size $61 \times 61 \ \mu m^2$.

6.3.2. Data preprocessing

Let p be a slice of the phantom containing a set of particles that we want to reconstruct and let $\mathcal{I}_p^t \in \mathbb{R}_{\geq 0}^{196 \times 196}$ be the 2D scan image of slice p at measurement time t obtained as described above. For our reconstruction method using non-negative Radon measures to be applicable, we ideally want an image I_p^t in which the only pixel values greater than zero are caused by the iron particles in otherwise neutral surroundings. But the agarose gel used in our phantom is not perfectly homogeneous as it contains small air pockets as well as slight variations in density, and in practical application, particles will usually not be tracked in a neutral medium but in a much more complex 'background' such as, for instance, a human body. Thus, we have $\mathcal{I}_p^t = I_p^t + \eta$, where η is the background noise. Furthermore, note that the iron particles cause signal voids that cause hypointense spots of lower pixel values in the acquired images. In order to retrieve I_p^t, we thus choose a base slice b containing no particles for which $\mathcal{I}_b^t$ is as similar to η as available and obtain via subtraction the approximation

$$\tilde{I}_p^t = \mathcal{I}_b^t - \mathcal{I}_p^t \tag{6.7}$$

of I_p^t. While the aim of the image subtraction is to obtain a neutral background, due to natural inhomogeneities between the different slices and phantom tubes, a certain level of noise persists. We create the option to remove this noise by setting all pixel values under a certain noise threshold to zero. This threshold is chosen indvidually per image such that all inhomogeneities outside of the particle voids are removed while not unintentionally trimming the areas of influence of the particle voids themselves.
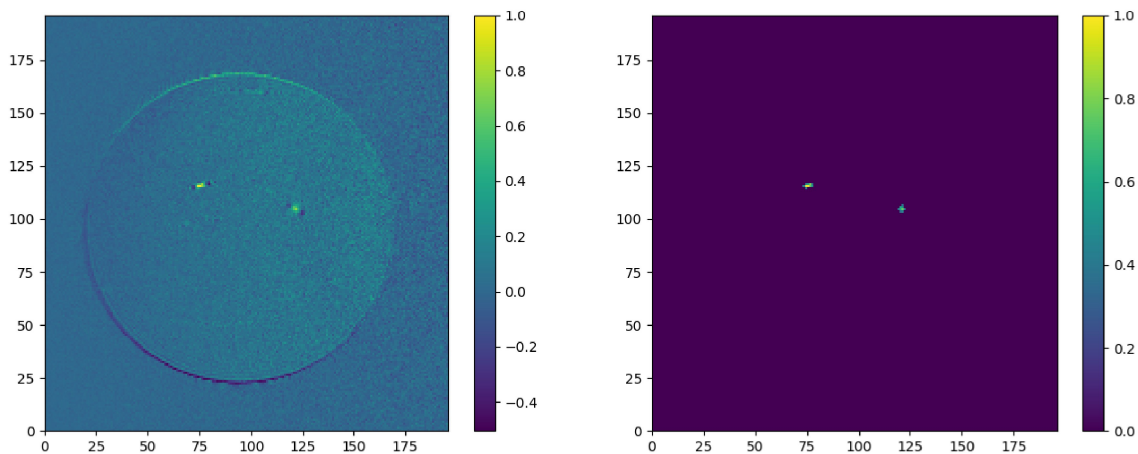

Figure 6.5.: Example of a preprocessed image. Left: Image obtained via subtraction of a particle image from a base image. Right: The same image after filtering for annular inconsistency and noise.

As an additional difficulty, the aforementioned off-centre rotation axis and the subtle slant of the phantom position inside the scanner cause variations in the exact locations of the tube slices in the retrieved images. This means that upon subtracting two images an annular inconsistency is created, a circular pattern of noise that can distort particle detection (see

figure 6.5). In order to remove this inconsistency from an image, we set all pixel values outside of a chosen radius around a chosen centre point to zero. As with the noise threshold before, we choose centre and radius for each image individually, in a way which ensures that anything from the inconsistency outward is zero, but as little as possible is lost inward from it. The imperfect rotation also causes the simulated trajectories of the particles to not be perfectly circular, but since we only cover short distances travelled in order to approximate linear and not circular movement, we disregard this issue.

We expect the mass of any particle to remain constant throughout its movement, this is reflected in the reconstruction method. However, the receiver coils of the scanner are not arranged evenly around its circumference. Because of their local placement, the strength of the signal recovered by them has a negative gradient away from the coils, resulting in an uneven intensity in the acquired images, as can be seen in figure 6.6[3].
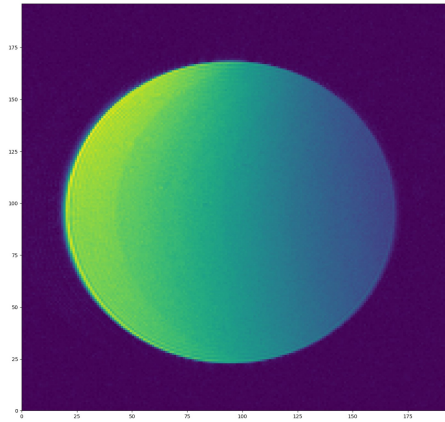

Figure 6.6.: Uneven shading due to placement of receiver coils.

After substraction of particle and base images, this then causes an equally uneven intensity in particles as they move closer to or further away from the coil locations. We mitigate this issue by element-wise multiplication with appropriate 196×196 matrices counteracting the uneven shading in the images (see figure 6.7).

It should also be noted that, by nature of the rotating set-up, the simulated particle movement is circular instead of linear. After preprocessing, measurement data f is then generated from the preprocessed images via the two-dimensional fast fourier transform.

---

[3]Colourbars are left out from here on for the benefit of avoiding crowded figures. The scale of pixel values after postprocessing remains as in the right-hand side image in figure 6.5, ranging from 0 (dark violet) to 1 (yellow).
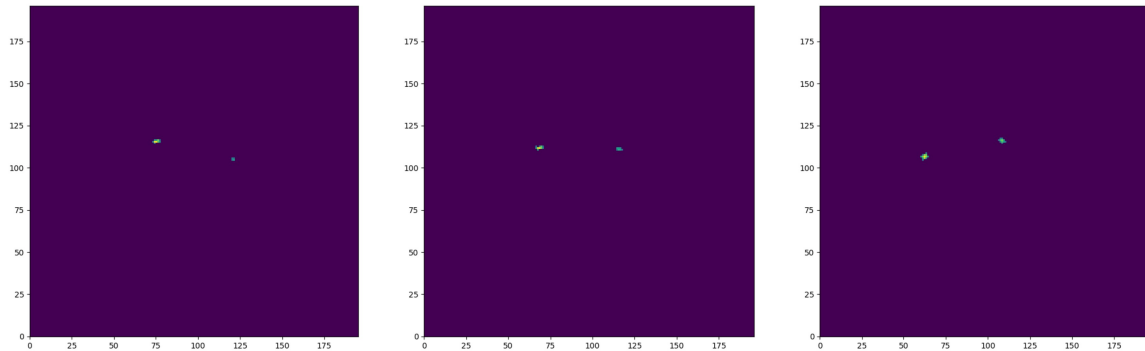
a) Particles with inconsistencies in weights and radii, obtained from the subtraction of base and particle images that are unevenly shaded due to receiver coil placement.
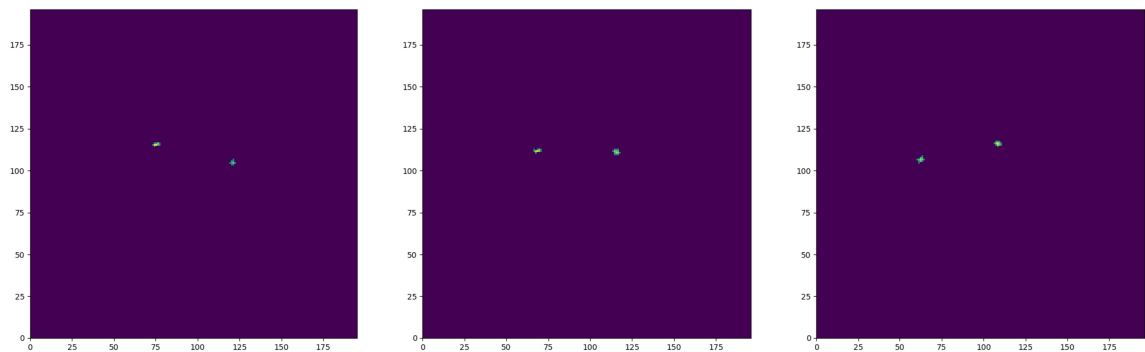
b) The same particles with more consistent weights and radii across measurement times, obtained from the subtraction of actively reshaded base and particle images.

Figure 6.7.: Comparison of particles without and with active reshading.

6.3.3. Results

We consider a slice with two particles, scanned at three measurement times with a rotational speed of $4.39 \cdot 10^{-3}$ rotations per minute, slow enough that there is barely any motion blur present in the resulting images, which are shown in figure A.2a. For each measurement time, a full scan of 196 full k-space lines was made. Thus, we set $\Delta t = \frac{1}{196}$ in the real experiments, following the reasoning in section 6.2.1.

Since this setup does not offer a ground truth with discrete initial locations and defined move vectors, the postprocessing and evaluation procedures require adaptation in two regards. Analogously to the clustering process performed on the reconstructions in the simulated experiments, we now generate an artificial baseline to compare the reconstruction against by identifying clusters of non-zero pixel intensities in the scan at time $t = 0$ and defining a 'ground truth' location at the centre of mass of each cluster and assign it the summed cluster weight. As can be seen in figure A.2a, the motion blur is small enough to allow sufficiently accurate particle localisation using this approach. Furthermore, we calculate the squared unbalanced Wasserstein divergence in two distinct variants. The first is completely analogous to the simulated setting, using the artificial baseline in place of $u_0^\dagger$. We refer to this variant as wdc. The second variant, which we call wdp, instead regards as ground truth locations the pixel centres of the scan image at time $t = 0$, with the pixel intensities set as

weights. In both variants we set all pixel intensities below a threshold of 0.3 to zero.

The results are summarised in table 6.2, and selected reconstructions are shown in figure 6.8. Overall, increased amounts of input data yield higher precision and lower Wasserstein divergence for both methods. A line frequency cutoff $\Phi_0 = 3$ in the k-square setting significantly reduces the Wasserstein divergence, especially for the MRI-adapted method where it is lowered to less than half the divergence for $\Phi_0 = 2$. The strongest results for both methods are achieved for full-lines without convolution. It is notable that the reconstruction with the full-lines MRI-adapted method with a line-cutoff of $\Phi_0 = 2$ is still slightly better than that achieved using the dimred method with $\Phi_0 = 3$, evaluated by divergence. MRI-adapted full-lines reconstructions with $\Phi_0 = 3$ were not performed due to limitations in computational resources.

Φ_0	Φ_1	conv	precision	recall	wdc	wdp
2	2	0	0.50	1.00	0.01110	0.00935
		2	0.50	1.00	0.01112	0.00950
		4	0.50	1.00	0.01128	0.00970
	40	0	1.00	1.00	0.00599	0.00469
		2	1.00	1.00	0.01536	0.01469
		4	0.00	0.00	0.02561	0.02551
3	3	0	0.67	1.00	0.00508	0.00372
		2	0.67	1.00	0.00507	0.00376
		4	0.67	1.00	0.00518	0.00397

(a) Results for the MRI-adapted method.

Φ_0	Φ_1	conv	precision	recall	wdc	wdp
2	2	0	0.50	1.00	0.01271	0.01120
		2	0.50	1.00	0.01281	0.01119
		4	0.50	1.00	0.01298	0.01138
	40	0	0.67	1.00	0.00949	0.00811
		2	1.00	1.00	0.01552	0.01476
		4	0.00	0.00	0.02715	0.02701
3	3	0	0.67	1.00	0.00976	0.00823
		2	0.67	1.00	0.00983	0.00828
		4	0.67	1.00	0.00999	0.00845
	40	0	1.00	1.00	0.00668	0.00549
		2	1.00	1.00	0.01432	0.01355
		4	0.00	0.00	0.02705	0.02685

(b) Results for the dimred method.

Table 6.2.: Comparison of precision, recall, wdc and wdp values for the MRI-adapted and dimred methods across various choices of Φ_0, Φ_1 and convolution radius (conv), colour-coded from best (green) to worst (red) performance in the respective indicator. Convolution radii are given in $\frac{x}{196}$ distance units in the field-of-view.

With respect to convolution, the reconstructions consistently decrease in quality for higher

radii, indicating that the convolution as designed for the adapted method in chapter 5 may not be a suitable approach to capturing the non-zero radii of the imaged particles. While the detrimental effects of higher choices of radii on the reconstruction, namely resulting in higher Wasserstein divergence values, are subtle for the k-square setting, they are exacerbated for $\Phi_1 = 40$. We suspect that the convolution has too strong a blurring effect, possibly over-smoothing the reconstruction especially for higher frequencies, which would explain weaker results for high radii in the full-lines setting in particular. The breakdown of the reconstruction for a radius of $\frac{4}{196}$ may be due to the fact that this choice of radius implies a particle diameter of about 0.04 distance units in the field-of-view, while the actual particles in the scans appear to be closer to about 0.02 in diameter, even with the slight motion blur.

We note that the MRI-adapted method overall performs equally as well as or better than the dimred method on all three metrics in all settings compared here, even for the low speed of rotation at which the considered scan was made, emulating only slow particle movement.
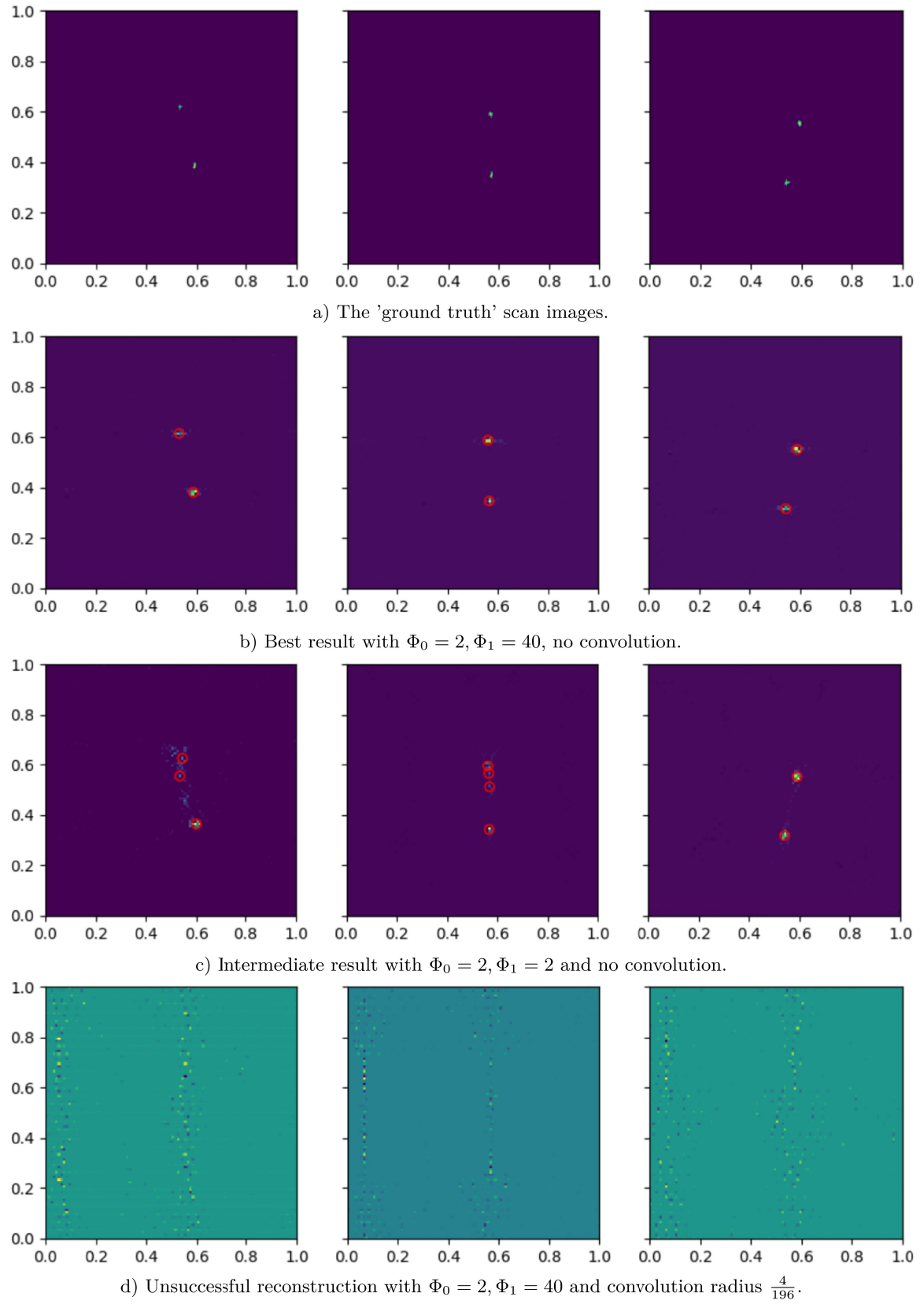
a) The 'ground truth' scan images.

b) Best result with $\Phi_0 = 2, \Phi_1 = 40$, no convolution.

c) Intermediate result with $\Phi_0 = 2, \Phi_1 = 2$ and no convolution.

d) Unsuccessful reconstruction with $\Phi_0 = 2, \Phi_1 = 40$ and convolution radius $\frac{4}{196}$.

Figure 6.8.: Exemplary results of reconstructions using the MRI-adapted method on real scan data.

CHAPTER 7

Conclusions and outlook

This thesis aimed to adapt a dimension-reduced reconstruction method for reconstructing configurations of linearly moving particles from MRI data, building upon the approach introduced by Holler et al. in [3]. We covered the original method by Holler et al. and examined its reconstruction properties for noise-free as well as noisy data.

Following an introductory explanation of the physical and technical foundations of MRI, we identified specific requirements for an observation operator tailored to MRI with cartesian sampling. These included

1. a foundation on the truncated Fourier transform to accurately represent the nature of k-space in MRI,

2. the consideration of temporal progression during measurement, specifically time passing between the acquisition of lines in k-space, and

3. capturing the non-zero radii of iron-particles' areas of influence on the scan image by convolution with the characteristic function of a ball of the particle radius.

The main contribution of this thesis is the successful construction of an MRI observation operator that meets these outlined requirements.

We discretised the MRI-adapted dimension-reduced method and tested it on both simulated and real MRI data. Experiments on simulated particle configurations demonstrated that the MRI-adapted method effectively managed the challenges posed by the passage of time during MRI data acquisition, which the unaltered method was not adapted to and failed at. Furthermore, our results for various levels of dynamic separation in the configurations, namely higher reconstruction rates for larger dynamic separations, indicate that dynamic separation may potentially serve as a basis for defining a source condition for this method. Lastly, our findings for the development of the reconstruction error with increasingly noisy data suggest similar behaviour to that of the original method scaling with $\sqrt{\delta}$, but further experimentation and theoretical inquiry are required.

We also showed superior performance of our MRI-adapted method with regard to recall, precision and Wasserstein divergence on a real MRI scan of a phantom simulating particle movement via slow controlled rotation. The convolutional adjustments did not yield improvements but rahter produced weaker results. This possibly indicates that the particles' areas of influence on the images are small enough that further adaption to capture this effect may not turn out to be necessary. But a different methodological adaptation could capture the particle influence more successfully.

Building on the work presented in this thesis, the reconstruction method could be adapted for alternative MRI sampling schemes. Adaptation to planar echo (or 'zigzag') patterns may

be particularly feasible, since their line-by-line design closely resembles that of cartesian trajectories. Further experimentation on real MRI scan data is needed to validate the method, optimally with a phantom setup that is more explicitly tailored for generating linear particle trajectories.

Beyond experiments, theoretical inquiry into the reconstruction properties of the MRI-adapted method is required. The formulation of a specific source condition for exact reconstruction on noise-free data, as well as the examination of the reconstruction error on noisy data are of interest.

Eventually, an extended application to particle configurations in more heterogeneous media is desired, approaching more realistic (clinical) MRI scenarios. A practical next step would be to implement the reconstruction in the presence of a static background image, for instance a brain scan, with the ultimate goal of applying the method to MRI scans of iron-marked cells in living subjects to assess the method's applicability to biologically relevant contexts.

Bibliography

[1] Jacques Hadamard. Sur les problèmes aux dérivées partielles et leur signification physique. *Princeton University Bulletin*, pages 49–52, 1902.

[2] Giovanni S. Alberti, Habib Ammari, Francisco Romero, and Timothée Wintz. Dynamic spike super-resolution and applications to ultrafast ultrasound imaging. *SIAM Journal on Imaging Sciences*, 12(3):1501–1527, January 2019.

[3] M. Holler, A. Schlüter, and B. Wirth. Dimension reduction, exact recovery, and error estimates for sparse reconstruction in phase space. *Applied and Computational Harmonic Analysis*, 70:101631, May 2024.

[4] Benedikt Wirth. Inverse problems - lecture notes, 2021.

[5] Walter Rudin. *Real and complex analysis*. McGraw-Hill international editions. McGraw-Hill, New York, NY, 1987.

[6] A. Rényi. On projections of probability distributions. *Acta Mathematica Academiae Scientiarum Hungaricae*, 3(3):131–142, September 1952.

[7] G. Bianchi and M. Longinetti. Reconstructing plane sets from projections. *Discrete amp; Computational Geometry*, 5(3):223–242, June 1990.

[8] Carlos Fernandez-Granda Emmanuel J. Candès. Super-resolution from noisy data. *Journal of Fourier Analysis and Applications*, 19(6):1229–1254, December 2013.

[9] Richard Ansorge and Martin Graves. *The Physics and Mathematics of MRI*. 2053-2571. Morgan and Claypool Publishers, 2016.

[10] Allen D. Elster. https://mriquestions.com. Accessed September 19, 2024.

[11] F. Bloch. Nuclear induction. *Physical Review*, 70(7–8):460–474, October 1946.

[12] Thomas A. Gallagher, Alexander J. Nemeth, and Lotfi Hacein-Bey. An introduction to the fourier transform: Relationship to mri. *American Journal of Roentgenology*, 190(5):1396–1405, May 2008.

[13] Johan Overweg. Mri main field magnets. In *14th ISMRM scientific meeting and exhibition*. International Society for Magnetic Resonance in Medicine (ISMRM), 2006.

[14] Dmitry Kurzhunov. *Novel Reconstruction and Quantification Methods for Oxygen-17 Magnetic Resonance Imaging at Clinical Field Strengths*. PhD thesis, 2017.

[15] Vijay P.B. Grover, Joshua M. Tognarelli, Mary M.E. Crossey, I. Jane Cox, Simon D. Taylor-Robinson, and Mark J.W. McPhail. Magnetic resonance imaging: Principles and techniques: Lessons for clinicians. *Journal of Clinical and Experimental Hepatology*, 5(3):246–255, September 2015.

[16] I. I. Rabi, J. R. Zacharias, S. Millman, and P. Kusch. A new method of measuring nuclear magnetic moment. *Physical Review*, 53(4):318–318, February 1938.

[17] E. M. Purcell, H. C. Torrey, and R. V. Pound. Resonance absorption by nuclear magnetic moments in a solid. *Physical Review*, 69(1–2):37–38, January 1946.

[18] Nobel Prize Outreach AB 2024. All nobel prizes in physics. NobelPrize.org. Accessed September 24, 2024.

[19] W. F. Eberlein. The spin model of euclidean 3-space. *The American Mathematical Monthly*, 69(7):587–598, August 1962.

[20] Richard Phillips Feynman, Robert Benjamin Leighton, and Matthew Sands. *The Feynman lectures on physics*, volume II, chapter Chapter 34 - The Magnetism of Matter. Basic Books, New York, 2010. Originally published 1963-1965.

[21] W. Gerlach and O. Stern. Der experimentelle nachweis des magnetischen moments des silberatoms. *Zeitschrift für Physik*, 8(1):110–111, December 1922.

[22] Malcolm H. Levitt. *Spin Dynamics: Basics of Nuclear Magnetic Resonance*. Wiley, Chichester, 2. ed., repr. edition, 2011.

[23] Peter Zacharias. *Magnetic Properties of Materials*, pages 81–124. Springer Fachmedien Wiesbaden, 2022.

[24] Mehmet Akçakaya, Maxine Tang, and Reza Nezafat. *Cardiac Magnetic Resonance Imaging Physics*, pages 1–16. Springer New York, 2019.

[25] Rolf Gebker, Jürg Schwitter, Eckart Fleck, and Eike Nagel. How we perform myocardial perfusion with cardiovascular magnetic resonance. *Journal of Cardiovascular Magnetic Resonance*, 9(3):539–547, May 2007.

[26] Bernd André Jung and Matthias Weigel. Spin echo magnetic resonance imaging. *Journal of Magnetic Resonance Imaging*, 37(4):805–817, March 2013.

[27] Kai Tobias Block, Martin Uecker, and Jens Frahm. Undersampled radial mri with multiple coils. iterative image reconstruction using a total variation constraint. *Magnetic Resonance in Medicine*, 57(6):1086–1098, May 2007.

[28] Bénédicte M.A. Delattre, Robin M. Heidemann, Lindsey A. Crowe, Jean-Paul Vallée, and Jean-Noël Hyacinthe. Spiral demystified. *Magnetic Resonance Imaging*, 28(6):862–881, July 2010.

[29] George B. Arfken, Hans J. Weber, and Frank E. Harris. *Integral Transforms*, pages 963–1046. Elsevier, 2013.

[30] Mosek ApS. *MOSEK Optimizer API for Python 10.2.3*, 2024.

[31] Enrica Wilken, Asli Havlas, Max Masthoff, Amir Moussavi, Susann Boretius, and Cornelius Faber. Radial compressed sensing imaging improves the velocity detection limit of single cell tracking time-lapse mri. *Magnetic Resonance in Medicine*, 91(4):1449–1463, December 2023.

APPENDIX A

Experiment notes

A.1. Experiments with spliced data

Beyond the experiments in section 6.3.3, we attempted employing spliced scan data as a way of circumventing the issue of unknown ground truths for higher rotational speeds. More specifically, the splicing works as follows:

- Make a minimum of fifty scan images such that the phantom is static during scans but rotated by an equal amount between any two consecutive scans.

- Construct an artificially 'dynamic' measurement f by combining k-space lines from the fast Fourier transforms of multiple static scans. The simplest example would be to take the first line from the k-space of the first scan, the second from the k-space of the second scan and so forth. For a higher artificial speed, one can then skip scans and use k-space lines only from every second, third etc.

The problem with this plan lay in the data issues as described in section 6.3.2 as not enough static images could be preprocessed in a way that secures both sufficient faithfulness to the scans and sufficient consistency between them for the reconstruction to function. After
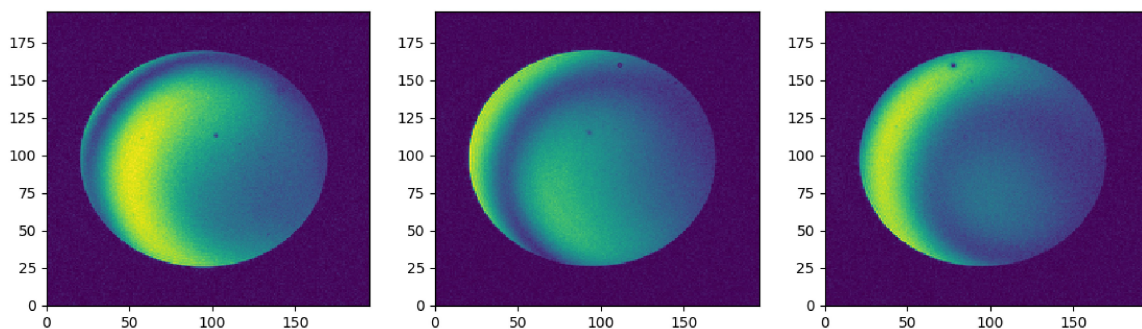

Figure A.1.: Three static images, each four rotation phases apart, with significant discrepancies in particle intensity.

subtraction of particle from base images and preprocessing, despite individual mitigation efforts for every scan, discrepancies were still too great for our reconstruction method to succeed.

A.2. Dynamic separation histograms

The simulated ground truths used in the numerical experiments in chapter 6 have an average number of 8.9745 particles with dynamic separations as illustrated in the histograms in figure A.2.

a) $\mathcal{T}$ with $|\mathcal{T}| = 3$

b) $\mathcal{T}$ with $|\mathcal{T}| = 5$

c) $\mathcal{T}_2$ with $|\mathcal{T}| = 3$

d) $\mathcal{T}_3$ with $|\mathcal{T}| = 3$

e) $\mathcal{T}_2$ with $|\mathcal{T}| = 5$
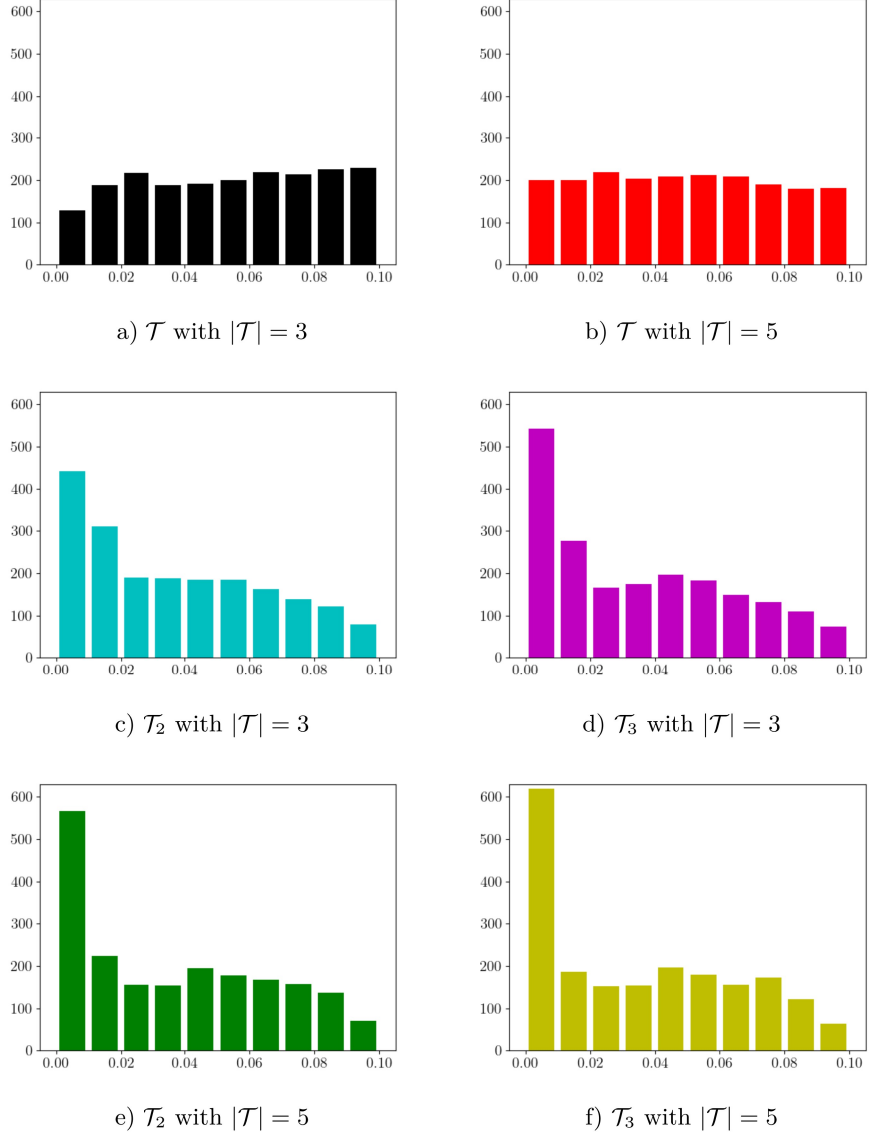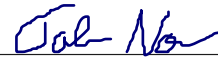
f) $\mathcal{T}_3$ with $|\mathcal{T}| = 5$

Figure A.2.: Histograms of dynamic separation $\Delta_{dyn}(C, T)$ of configurations C in the ground truth dataset for varying choices of set of times T, where $\mathcal{T}$ and $\mathcal{T}_\Phi$ are defined as in section 6.2.1.

Declaration of Academic Integrity

I hereby confirm that this thesis on *Dimension-reduction for reconstruction of dynamic particle configurations from MRI data* is solely my own work and that I have used no sources or aids other than the ones stated. All passages in my thesis for which other sources, including electronic media, have been used, be it direct quotes or content references, have been acknowledged as such and the sources cited.

Münster, November 7, 2024

(Tabea Naeven)